

DESIGN AND FABRICATION OF OPTICALLY-PUMPED GUIDED-MODE
RESONANCE SURFACE-EMITTING LASERS

by

PRESTON P. YOUNG

Presented to the Faculty of the Graduate School of
The University of Texas at Arlington in Partial Fulfillment
of the Requirements
for the Degree of

DOCTOR OF PHILOSOPHY

THE UNIVERSITY OF TEXAS AT ARLINGTON

May 2006

Copyright © by Preston P. Young 2006

All Rights Reserved

Dedicated to my grandfather Mead P. Young, my father Phillip M. Young,
and my advisor Dr. Robert Magnusson.

ACKNOWLEDGEMENTS

I wish to thank the following persons for their contributions without which this work would not have been possible. First and foremost thanks are to Dr. Robert Magnusson and Dr. Theresa A. Maldonado. Their support and guidance began with my sponsorship in the National Science Foundation Research Experiences for Undergraduates (NSF-REU) program in the University of Texas at Arlington Electro-Optics Research Center (EORC). Through participation in the NSF-REU program, my educational journey ultimately led to attaining the Doctor of Philosophy degree in Electrical Engineering. I would never have dreamed this possible without the original seeds being planted and the additional encouragement provided by Dr. Magnusson and Dr. Maldonado. They gathered together an exceptionally bright and talented group of students at the UTA EORC who I thank for their help, advice, and friendship. These include Sorin Tibuleac, Debra Wawro, Purnomo Priambodo, Zhongshan Liu, Dongho Shin, Georgeanne Radloff, and Kevin Le.

Over the course of my education, I have been privileged to learn from many truly excellent professors and colleagues. These include my Committee members Dr. Alan Davis, Dr. Meng Tao, Dr. Timothy Holzheimer, and especially Dr. Truman Black for his friendship, encouragement, and moral support. Additionally, I thank Dr. Kambiz Alavi for many insightful discussions and opinions. Again, without their support and encouragement, I would not have achieved this goal.

For direct contributions to this work, I express gratitude to Dr. Geoff Taylor at the University of Connecticut for advice and suggestions regarding practical design of strained quantum-well laser structures. The author is further indebted to him for providing the high-quality MBE growth of the GMR-SEL laser wafer structure. I again thank Dr. Kambiz Alavi at UTA for providing the photoluminescence system and insight for characterization of the GMR-SEL wafer. I also again wish to thank Dr. Truman Black of the UTA Department of Physics for the use of his Laser and Spectroscopy Laboratory facilities. Additionally, the author offers sincere gratitude to the members and staff of the Cornell Nanofabrication Facility (CNF) for immeasurable advice and support in the fabrication and processing work presented in Chapters 5 and 6. This thanks is especially extended to Michael Skvarla, Alan Bleier, John Treichler, Jerry Drumheller, Rob Illic, and Daron Westly for their suggestions and patience.

Finally, I thank my friends and family for their support and encouragement.

April 18, 2006

ABSTRACT

DESIGN AND FABRICATION OF OPTICALLY-PUMPED GUIDED-MODE RESONANCE SURFACE-EMITTING LASERS

Publication No. _____

Preston P. Young, Ph.D.

The University of Texas at Arlington, 2006

Supervising Professor: Robert Magnusson

This dissertation describes the design and fabrication of guided-mode resonance (GMR) structures and their applications to laser devices. These include tunable Ti:Sapphire lasers as well as semiconductor lasers with integrated light emitting layers. The resonance characteristics of GMR structures are determined by the designed and fabricated waveguide-grating parameters. The primary tool for the design and simulation analysis of GMR devices is rigorous coupled-wave analysis (RCWA). This numerical method is used to provide diffraction efficiency calculations as well as simulations of the electric fields within GMR structures. RCWA-based field analysis is used to design an optically pumped GMR surface-emitting laser (GMR-SEL) in the

GaAs/Al_xGa_{1-x}As material system with an In_{0.2}Ga_{0.8}As quantum well for output wavelength near 980 nm.

All optical GMR devices require patterning of sub-micron diffraction grating structures. Preliminary GMR grating fabrication is performed by holographic interference lithography and is optimized by utilizing a charge-coupled device (CCD) camera-based fringe stabilization system. Prototype GMR-SEL devices are fabricated in the GaAs/Al_xGa_{1-x}As material system by electron-beam lithography and reactive-ion etching (RIE). Electron-beam lithography is performed using hydrogen silsesquioxane (HSQ) as high-resolution resist material. The results of exposure proximity correction for electron-beam lithography are presented. An RIE process suitable for reliable etching of the HSQ grating patterns into a semiconductor GMR-SEL wafer is developed and characterized.

The fabricated prototype GMR-SEL devices are optically pumped at an oblique GMR resonance angle near 45° corresponding to the 810 nm output of a Ti:Sapphire laser. Whereas these elements have insufficient gain for lasing, the measured photoluminescence spectra for several devices exhibit spectral peaks that occur precisely at the theoretical GMR-SEL resonance locations. Therefore, this dissertation provides results and methods useful to experimentally realize prototype GMR-SEL devices fabricated in semiconductor materials.

TABLE OF CONTENTS

ACKNOWLEDGEMENTS.....	iv
ABSTRACT	vi
LIST OF ILLUSTRATIONS.....	xii
LIST OF TABLES.....	xvii
Chapter	
1. INTRODUCTION	1
2. GUIDED-MODE RESONANCE DEVICES, RIGOROUS COUPLED- WAVE FIELD ANALYSIS, AND APPLICATION TO TITANIUM- SAPPHIRE LASERS	7
2.1 Guided-Mode Resonance Device Characteristics.....	7
2.2 Rigorous Coupled-Wave Analysis Formulation for Internal Fields Calculations	11
2.3 Ti:Sapphire Lasers with GMR Output Couplers	16
3. GUIDED-MODE RESONANCE SURFACE-EMITTING LASER DESIGN, WAFER CHARACTERIZATION, AND DESIGN OPTIMIZATION	21
3.1 Preliminary GMR-SEL Design Analysis.....	21
3.2 Initial GMR-SEL design.....	25
3.3 RCWA Analysis of Initial GMR-SEL Design.....	28
3.4 RCWA Fields Analysis of Initial GMR-SEL Design.....	31
3.5 Summary of GMR-SEL design.....	36

3.6 Laser Wafer Characterization	39
3.7 Design Changes for GMR-SEL Wafer #2	45
3.8 Summary of GMR-SEL Design and Design Optimization	48
4. HOLOGRAPHIC SUB-WAVELENGTH GRATING FABRICATION, ACTIVE FRINGE STABILIZATION, AND PHOTORESIST STACK DESIGN	49
4.1 Holographic Interferometer Performance Characteristics	50
4.2 Interference Fringe Stabilization.....	55
4.3 Fringe Stabilization Methods.....	56
4.4 CCD Camera-Based Fringe Stabilization Method.....	58
4.5 Fringe Stabilizer Performance Results.....	64
4.6 CCD-based Fringe Stabilization Summary.....	67
4.7 Design of photoresist stacks for optimum exposure characteristics	67
4.8 Photoresist Grating Requirements and Exposure Characteristics.....	68
4.9 Photoresist stack design using a bottom anti-reflection (BARC) coating	75
4.10 Photoresist stack design for basic two-layer dielectric GMR structure Photoresist Grating Requirements and Exposure Characteristics.....	81
4.11 Photoresist stack design for patterning of GMR-SEL structure on GaAs.....	85
4.12 Summary of sub-micron photoresist grating fabrication	87
5. ELECTRON-BEAM LITHOGRAPHY AND REACTIVE- ION ETCHING FOR FABRICATION OF SUB-MICRON GRATINGS	89

5.1 Sub-Micron Grating Fabrication for GMR-SEL devices.....	90
5.2 Electron-Beam Patterning of Sub-Micron Diffraction Gratings	91
5.3 Electron-Beam Resist Materials	92
5.4 Hydrogen Silsesquioxane (HSQ) as a Negative Electron-Beam Resist	92
5.5 Electron-Beam Exposure Dose Testing Using HSQ Resist on GaAs Substrates	94
5.6 HSQ Exposure Dose Pattern Results	99
5.7 Wet Etching of GaAs Gratings Using HSQ Resist.....	101
5.8 Electron-Beam Proximity Exposure Effects.....	103
5.9 Proximity-Effect Correction	104
5.10 Exposure Dose Testing for Proximity Effect Corrected Pattern	108
5.11 Reactive-Ion Etching (RIE) of HSQ Gratings on GaAs	112
5.12 Summary of Electron-Beam Patterning and RIE Etching of Sub-Micron Grating Structures on GaAs	118
6. FABRICATION OF GUIDED-MODE RESONANCE SURFACE-EMITTING LASERS BY ELECTRON- BEAM LITHOGRAPHY, REACTIVE ION ETCHING, AND TESTING	119
6.1 Electron-Beam Patterning of GMR-SEL Grating Structures.....	120
6.2 RIE Etching of GMR-SEL Grating Structures	122
6.3 GMR-SEL Laser Test Setup	124
6.4 GMR-SEL Laser Test Results	125
6.5 GMR-SEL Laser Fabrication Results Summary.....	129

7. CONCLUSIONS	132
APPENDIX	
A. MATHCAD IMPLEMENTATION OF 3-LAYER ASYMMETRICAL WAVEGUIDE ANALYSIS ROUTINE.....	140
REFERENCES	143
BIOGRAPHICAL INFORMATION.....	152

LIST OF ILLUSTRATIONS

Figure	Page
2.1 Basic 2-layer waveguide-grating GMR mirror	8
2.2 Simulated results of GMR TE reflectivity versus wavelength at normal and 5° angles of incidence for the structure illustrated in Fig. 2.1	8
2.3 Simulated GMR reflectivity versus wavelength as a function of grating period for the waveguide-grating structure of Fig. 2.1	9
2.4 Simulated GMR TE reflectivity versus wavelength at variable angles of incidence for the waveguide structure of Fig. 2.1	10
2.5 Simulated field profiles for the GMR structure of Fig. 2.1 at resonance.....	14
2.6 RCWA simulated total electric field profile at time $t=0$ for structure of Fig. 2.1 with simulation parameters of Fig. 2.5	16
2.7 Schematic and measured output spectrum for a dye laser cavity using a GMR mirror as the output coupler using optimized components	17
2.8 Schematic of a practical Ti:Sapphire unidirectional ring laser cavity using optimized components.....	18
3.1 Schematic of GRM-SEL structure with 980 nm laser output using 810 nm GMR resonant optical pumping	23
3.2 Simulated GMR-SEL response versus wavelength as function of grating period L for the structure of Table 3.1	29

3.3	Simulated GMR-SEL response versus wavelength as function of grating depth d_1 for the structure of Table 3.1	30
3.4	Simulated GMR-SEL response versus wavelength as function of grating fill factor for the structure of Table 3.1.....	30
3.5	Plot of electric fields as a function of position in the GMR-SEL layer structure.....	32
3.6	Plot of electric fields as a function of position in the GMR-SEL layer structure for adjusted spacer layer thickness	33
3.7	Plot of total electric fields as a function of position in the GMR-SEL layer structure showing the effect of variation in grating fill factor.....	34
3.8	Diffraction efficiency response of the basic GMR-SEL structure of Table 3.2 for 810nm TE polarized illumination.....	35
3.9	DCC X-Ray diffractometry results for commercial MBE-grown GMR-SEL laser wafer (Wafer #1)	40
3.10	Schematic of basic photoluminescence (PL) setup for characterization of quantum-well structure under short and long wavelength illumination conditions.....	44
3.11	Simulated plot of electric fields as a function of position in the GMR-SEL layer structure for Wafer #2 described in Table 3.5.....	46
3.12	Plot of measured photoluminescence for GMR-SEL Wafer #2	48
4.1	Schematic of Lloyd's mirror interferometer for exposure of sub-micron photoresist gratings	50
4.2	Schematic of intensity distributions for respective portions of expanded Gaussian beam incident on substrate and Lloyd's mirror.....	52
4.3	Stylized irradiance profile in substrate exposure plane with 20% and 10% variations in intensity of the respective incident and reference beams	54

4.4	Schematic layout of interferometer and fringe control system.....	58
4.5	Video frame and spatial intensity data.....	60
4.6	Snapshot of fringe stabilization software user interface.....	63
4.7	Measured uncorrected (a) and corrected (b) fringe shift in degrees versus time for a 150 second exposure.....	65
4.8	SEM photographs of 250 nm photoresist grating structures with variable exposure energy.....	66
4.9	Stylized plot of normalized photoresist thickness remaining after development versus logarithmic exposure energy for a positive photoresist.....	70
4.10	250 nm photoresist grating structures with variable exposure energy	71
4.11	250 nm photoresist grating structures with variable exposure energy and increased development time.....	72
4.12	Example of a photoresist grating profile showing a minimum practical fill factor of approximately 0.3	73
4.13	SEM photos of 310 nm photoresist gratings on a silicon wafer	77
4.14	Calculated profile of normalized electric field intensity in the direction normal to the silicon substrate	78
4.15	SEM photo of a photoresist grating on a silicon wafer exposed to threshold of clearing in the grating groove during development	79
4.16	Calculated profile of normalized electric field intensity in the direction normal to the substrate.....	80
4.17	Low-frequency noise pattern on a photoresist grating	82
4.18	Calculated profile of normalized electric field intensity in the direction normal to the substrate during photoresist exposure for two-layer GMR structure of Fig. 2.1	83

4.19	Calculated profile of normalized electric field intensity in the direction normal to the substrate for two-layer GMR waveguide structure with inclusion of BARC layer	84
4.20	Calculated profile of total electric field intensity in the direction normal to the GaAs substrate	86
5.1	Exposure dose-test pattern for electron-beam exposure characterization of HSQ gratings on GaAs	95
5.2	SEM micrographs of the initial exposure dose pattern shown in Fig. 5.1	98
5.3	SEM micrographs of the initial exposure-dose pattern shown in Fig. 5.1	100
5.4	SEM micrographs of wet-etched initial exposure-dose patterns using an HSQ resist mask on a GaAs substrate.....	102
5.5	Monte Carlo simulation profiles for electron scattering events in a PMMA resist layer on a silicon substrate	103
5.6	Schematic showing how the GHOST technique can be used to correct for the proximity effect.....	106
5.7	Screenshots of fractured grating pattern of Fig. 5.1 obtained from PROCECCO software.....	107
5.8	SEM micrographs of HSQ grating structures as functions of exposure dose	109
5.9	SEM micrographs of HSQ grating structures as functions of exposure dose	111
5.10	SEM micrographs of RIE-etched GaAs grating depth as functions of etch time	115
5.11	SEM micrographs of RIE-etched GaAs grating depth as functions of etch time	117
6.1	Schematic of layout for electron-beam patterning of GMR-SEL devices.....	122
6.2	SEM micrographs of RIE etched GMR-SEL gratings structures.....	123

6.3	Schematic of GMR-SEL laser test setup	124
6.4	Graph of typical normalized photoluminescence (PL) obtained from GMR-SEL wafer devices	126
6.5	Schematic of layout for electron-beam patterning of GMR-SEL devices	124
6.2	SEM micrographs of RIE etched GMR-SEL gratings structures	123
6.3	Schematic of GMR-SEL laser test setup	125
6.4	Graph of typical normalized photoluminescence (PL) obtained from GMR-SEL wafer devices	127
6.5	Graph of measured normalized photoluminescence (PL) versus wavelength obtained from GMR-SEL wafer devices F-5 and G-1 with gold substrate mirrors.....	128

LIST OF TABLES

Table		Page
3.1	Initial GMR-SEL Design Parameters and Nominal Refractive Indices	28
3.2	Basic GMR-SEL Structure.....	36
3.3	Full GMR-SEL Structure with Integrated Bragg Mirror	36
3.4	Ellipsometer Analysis Summary for GMR-SEL laser Wafer #1	42
3.5	GMR-SEL Wafer #2 Design and Measured Layer Parameters	47
5.1	Process Parameters for RIE Etching of GaAs in ECR Etch System.....	114
6.1	Device Pattern Types for Patterning of Prototype GMR-SEL Devices	121

CHAPTER 1

INTRODUCTION

Guided-mode resonance (GMR) devices are a class of waveguide-grating structures that exhibit sharp resonant coupling between an incident wave and the waveguide modes supported by the dielectric structure. Passive GMR devices have been developed as reflection and transmission filters at both optical and microwave frequencies [1-7]. The unique properties of GMR devices can also be applied to control laser polarization, output wavelength, and spatial mode structure [7-17]. Initial applications utilized GMR devices implemented with dielectric materials, while only relatively few applications have utilized GMR structures implemented in semiconductor materials [12, 16-19]. This dissertation further addresses applications of GMR elements in laser systems and in particular, the development of active GMR lasers made with semiconductor materials [1, 12].

GMR mirrors have been demonstrated as output couplers in dye laser [7-11, 13] and Ti:Sapphire laser cavities. In each of these cases, the GMR mirror was mounted at normal incidence to the laser cavity yielding monochromatic laser output. For a given GMR waveguide-grating structure, the resonant wavelength is a strong function of the grating period and the angle of incidence. In this dissertation, a design for a tunable Ti:Sapphire laser using a GMR mirror as the tuning element is proposed. The angular

dispersion characteristic of a GMR mirror is used to select the laser output wavelength. This design presents a compact layout with tunability over approximately 150 nm.

Active GMR devices can be implemented with semiconductor materials as modulators [18, 19], amplifiers, and lasers [1, 7, 12]. GMR devices have also been investigated as external cavity devices for polarization and mode control in edge-emitting lasers and vertical-cavity surface-emitting lasers (VCSELs) [13-17]. Optically pumped surface-emitting solid polymer dye lasers using GMR structures have also been demonstrated [20, 21]. Preliminary designs for semiconductor-based electrically injected surface-emitting lasers (SELs) employing integrated GMR structures as both a high-reflectivity mirror and the gain element have been presented, but these devices have not been experimentally realized [1, 7, 12].

In this research, basic requirements and characteristics of integrating a GMR structure with a semiconductor active gain region are considered. From this analysis, implementations of guided-mode resonance surface-emitting lasers (GMR-SELs) are described. Preliminary analysis of GMR-SEL mirror reflectivity and quantum-well gain characteristics are described in [7]. These results are extended and applied in this dissertation for the design of prototype optically pumped GMR-SEL devices. A specific design for an optically pumped GMR-SEL using the GaAs/AlGaAs material system with a strained $\text{In}_{0.2}\text{Ga}_{0.8}\text{As}$ quantum well operating near 980 nm is presented. The GMR-SEL structure is designed and fabricated to employ resonant pumping at an oblique angle to the GMR device corresponding to an 810 nm pump wavelength. GMR-SEL characterization experiments performed in September 2004 demonstrated weak emission

peaks at wavelengths corresponding to excited guided-mode resonances as verified by numerical computation.

The primary software analysis tool employed for design and optimization of GMR devices in this work is the rigorous coupled-wave analysis (RCWA) method using the enhanced transmittance matrix method (ETMM) [27-29]. RCWA provides numerical solutions of the eigenvalue equations representing the electromagnetic fields and boundary conditions in the waveguide-grating structure. Additionally, the ETMM RCWA method was applied in this research for calculation and analysis of the internal fields in resonant waveguide-grating structures. The software to implement the ETMM RCWA method for internal fields calculations was developed as a key part of this research and written in the Electro-Optics Research Center at the University of Texas at Arlington (UTA). Typical results and insight gained from the RCWA field analysis are detailed in Chapter 2.

The GMR-SEL design is initially carried out using a homogenous waveguide analysis followed by initial estimation of the key waveguide-grating parameters [22]. The RCWA software is used to define and optimize the waveguide-grating parameters of the GMR-SEL. The UTA RCWA software code is then used to determine optimum spacing and thickness of the various layers for the GMR-SEL structure. Based on this design and analysis, GMR-SEL wafers are grown by molecular-beam epitaxy (MBE). Primary wafer characterization is performed by spectroscopic ellipsometry to verify the wafer layer thicknesses and material composition. Additionally, the active layer photoluminescence is measured to determine the peak wavelength of the quantum-well

gain. These results are then used to refine the design parameters for the GMR waveguide-grating. These parameters include the grating period, etch depth, and fill factor. Again, this analysis and optimization are performed with the RCWA fields software.

Based on the design analysis and wafer characterization, the next steps include lithographic definition of GMR-SEL gratings followed by etch transferal of the grating patterns into the wafer substrate layers. Reactive-ion-etching (RIE) is the preferred method for etch-transferal of the grating patterns into the GMR-SEL wafer in this work. These processes are developed and characterized before fabrication of the prototype GMR-SEL devices.

An essential step in the fabrication of all GMR structures is lithographic patterning of high quality diffraction gratings. Grating structures are fabricated in this research using both ultra-violet (UV) holographic and electron-beam lithography. Optimized fabrication of sub-micron grating structures using holographic lithography for photoresist gratings is described. A two-beam UV interferometer is designed and implemented that allows patterning of large-area photoresist gratings. The interferometer design allows convenient reconfiguration to produce uniform grating exposure over a wide range of grating periods. This interferometer configuration provides better uniformity and intensity balance between the incident and reference beams than that obtained from conventional single-beam interferometers. The two-beam interferometer setup also provides a means for stabilization of the fringe pattern during exposure.

A fringe stabilization system is developed as part of the UV interferometer to allow consistent fabrication of sub-micron photoresist gratings [34, 35]. The fringe stabilization method utilizes a CCD-camera element and software to provide real-time feedback control to the UV lithographic interferometer. The active fringe stabilizer described in this work is implemented as a simple PC-based system. The CCD camera allows for simplified setup of the fringe stabilization system when the projected fringe pattern cannot be visibly observed. The fringe stabilizer is a key element used in the patterning of grating structures used in fabrication of GMR devices in this and related work [4, 36, 64]. Results for gratings patterned on dielectric and semiconductor substrates are presented.

Electron-beam lithography is an alternative to interference lithography for patterning sub-micron diffraction gratings. With this method, it is possible to pattern both the grating pattern as well as the overall device structure in a single step. With interference lithography, a second mask and exposure must be used to define the device structure. In this research, electron-beam lithography is used to fabricate 320 nm and 160 nm grating periods on GaAs as part of the process development for GMR-SEL structures. The gratings are fabricated using hydrogen silsesquioxane (HSQ) as the resist material.

HSQ was originally developed as a low-k spin-on dielectric material for use in the microelectronics industry [72]. When exposed to an electron-beam, the HSQ cross-links into a SiO₂-like material [73]. Conventional organic photoresist developer is used to dissolve the unexposed HSQ resulting in a patterned hard mask for use in subsequent RIE etch processing. The process development and characterization results for electron-beam

patterning of sub-micron gratings on GaAs substrates are described in detail. The need for electron-beam proximity-effect pattern correction is demonstrated

These design, analysis, and processing results are then applied to the fabrication of prototype GMR-SEL devices. The GMR-SEL devices are fabricated by e-beam lithography with HSQ resist followed by RIE processing. Finally, the results of device testing and characterization are presented. In summary, this dissertation reports the design, fabrication, optimization, and characterization steps necessary for fabrication of optically pumped GMR-SEL devices.

CHAPTER 2

GUIDED-MODE RESONANCE DEVICES, RIGOROUS COUPLED-WAVE FIELD ANALYSIS, AND APPLICATION TO TITANIUM-SAPPHIRE LASERS

2.1 Guided-Mode Resonance Device Characteristics

The GMR effect is extensively described in other works [7, 23-26] and only the characteristics relevant to the work in this dissertation are presented. GMR resonant waveguide devices fabricated in conventional dielectric as well as semiconductor materials employ sub-wavelength gratings. The performance of GMR devices is typically very sensitive to the material and structural parameters used. These characteristics include the operating wavelength, range of input acceptance angles, linewidth, and sideband response away from resonance [2, 7, 23-26]. The operating wavelength for a given input angle is determined primarily by the grating period. This is easily controlled during the fabrication process. The linewidth is largely determined by the material parameters, especially the relative difference in the high and low refractive indexes used to form the grating (Δn). For large Δn values, the linewidth can be relatively broad – 5 nm or more as shown in AlGaAs structures presented in the laser design Chapter 3. GMR structures fabricated with a small Δn or shallow gratings can have full-width half maximum (FWHM) linewidths less than 0.5 nm [2, 25].

A basic 2-layer GMR mirror is shown in Fig. 2.1. This structure consists of a SiO₂ grating layer above an HfO₂ waveguide layer on a fused-silica substrate. The input

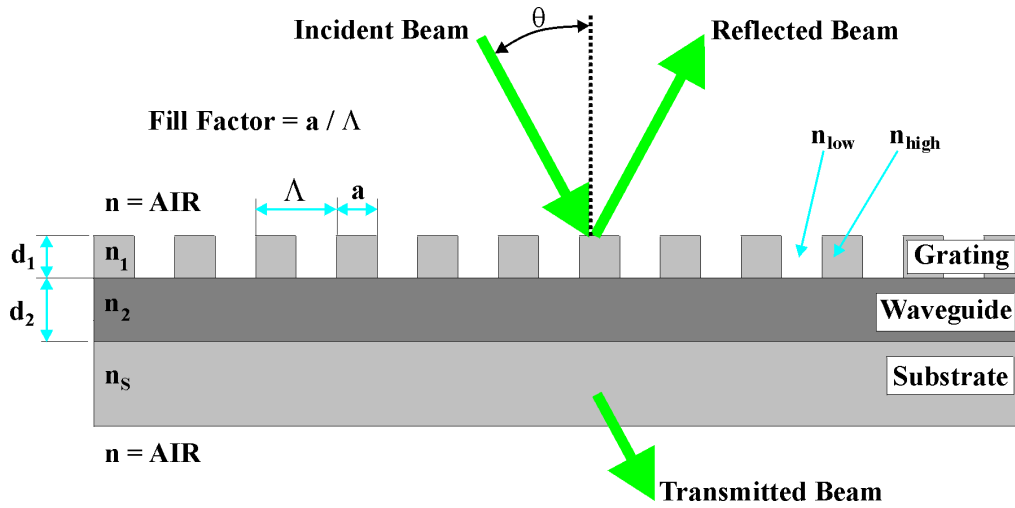


Figure 2.1. Basic 2-layer waveguide-grating GMR mirror. Physical parameters: $d_1 = 110$ nm, $d_2 = 190$ nm, $n_s = n_s = 1.46$ (SiO_2), $n_2 = 1.98$ (HfO_2), $n_{\text{high}} = 1.46$, $n_{\text{low}} = 1.0$, $\text{FF} = 0.5$, input and exit medium is air.

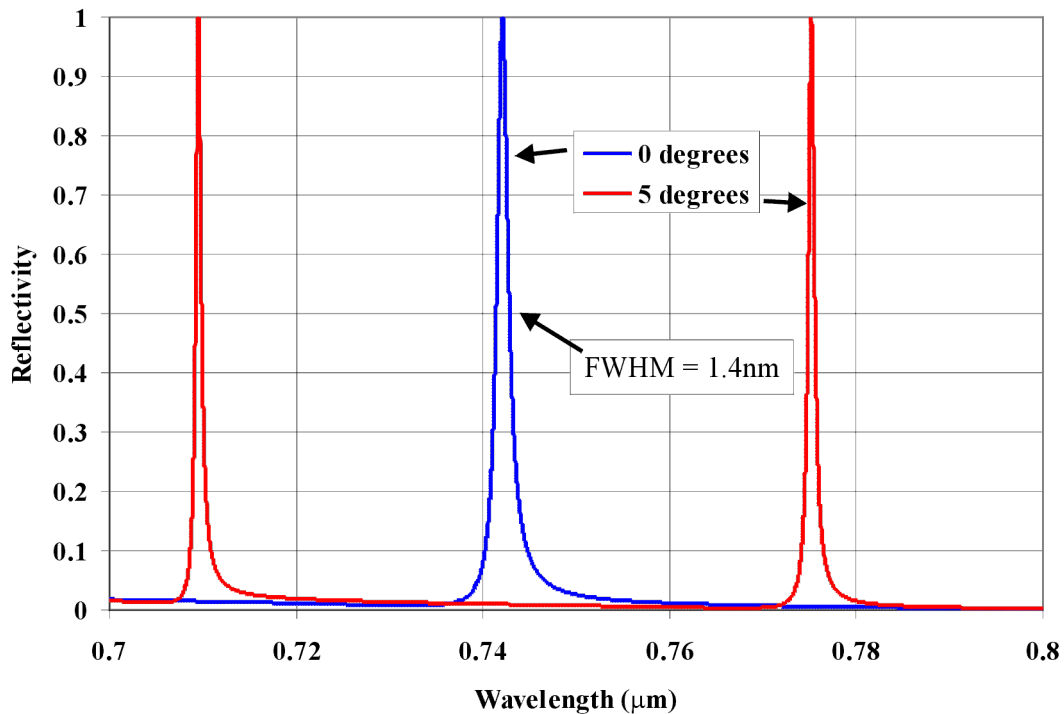


Figure 2.2. Simulated results of GMR TE reflectivity versus wavelength at normal and 5° angles of incidence for the structure illustrated in Fig. 2.1. The resonance peak occurs at 742.1 nm for normal incidence. Resonance peaks occur at 709.5 nm and 775.2 nm for 5° incidence. The grating period $\Lambda = 435$ nm.

and exit media are air. The reflectivity response for transverse electric (TE) polarized illumination at normal and 5° angles of incidence as functions of wavelength are given in Fig. 2.2. This response shows that there are two possible GMR resonant wavelengths for a given oblique angle of incidence. The response of Fig. 2.3 shows the sensitivity of the resonance wavelength to the grating period. The wavelength sensitivity for this example is approximately 2 nm of wavelength shift per nm grating period. Fig. 2.4 shows the sensitivity of the resonant wavelength to angle of incidence over a wide range of angles. The angular sensitivity near the 45° median angle becomes approximately 4 nm of wavelength shift per degree.

Sideband response (off resonance reflectivity) is determined by the overall layer structure and device material parameters. Multilayer GMR devices with low sideband

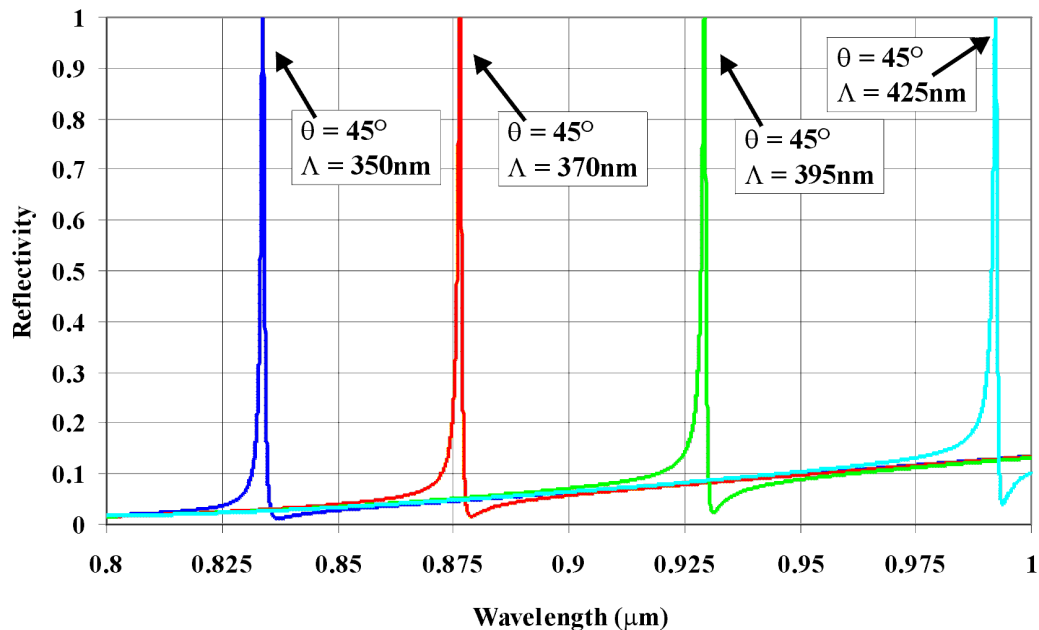


Figure 2.3. Simulated GMR reflectivity versus wavelength as a function of grating period for the waveguide-grating structure of Fig. 2.1. The input light is TE polarized and incident on the GMR mirror at a 45° angle.

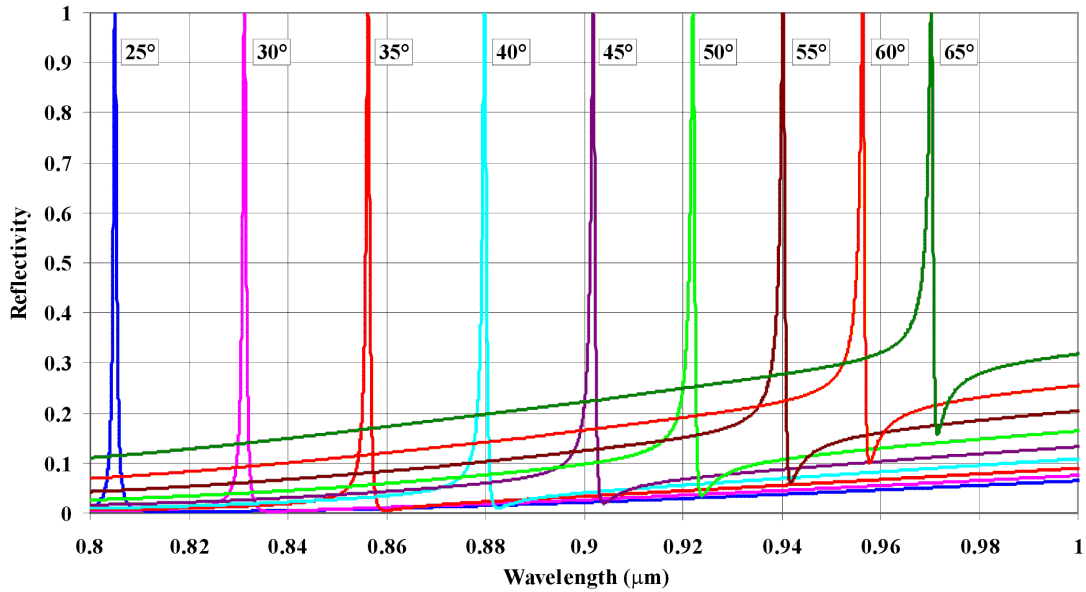


Figure 2.4. Simulated GMR TE reflectivity versus wavelength at variable angles of incidence for the waveguide structure of Fig. 2.1. Grating period $\Lambda = 382$ nm.

response are designed by performing a conventional thin film anti-reflection (for reflection filters) or high reflectivity design (for transmission filters) with the grating layer replaced by an equivalent thickness layer having the average refractive index (permittivity) of the grating layer [7]. This average refractive index is related to the refractive index of the materials used, the grating shape, and fill factor.

The structure of Fig. 2.1 is designed for a low sideband characteristic at normal incidence. It can be seen in Figures 2.3 and 2.4 that the sideband reflectivity increases as the wavelength or angle of incidence is increased from the normal incidence characteristic shown in Fig. 2.2. These calculations indicate the general need to optimize the waveguide-grating design parameters for each specific application. In the case of Fig. 2.4, additional layers could be introduced into the two-layer structure as in conventional

thin-film design to decrease the sideband response over the full range of incident angles [7, 26].

2.2 Rigorous Coupled-wave Analysis Formulation for Internal Fields Calculations

The original implementation of the rigorous coupled-wave analysis (RCWA) software was designed for diffraction efficiency calculations yielding relative amplitudes of the reflected and transmitted waves from a given structure [27-29]. The RCWA algorithm was reformulated [29] to provide improved numerical efficiency, stability, and convergence of the RCWA numerical solutions. This reformulation for improved RCWA performance is termed the enhanced transmittance matrix method (ETMM). The RCWA algorithm used by the UTA research group is based on the ETMM developed by Moharam et al. [29]. As an extension to the previous RCWA implementations, the ETMM was modified for work in this dissertation to allow calculation of the device internal fields.

The modification of the ETMM was developed out of necessity for this research and had not been specifically described in previous literature. Internal field calculations had been previously implemented with a characteristic matrix RCWA algorithm [30] based on original methods by Moharam et al. [29]. During development of the modified ETMM algorithm, correspondence with another research group [31] indicates that this modified algorithm was first developed by that group, although only calculated field results have been published without specific detail of the analysis method [1]. The validity of the internal field calculations algorithm has been verified through

correspondence with this research group. Commercial software providing similar internal fields calculations has also recently become available [32].

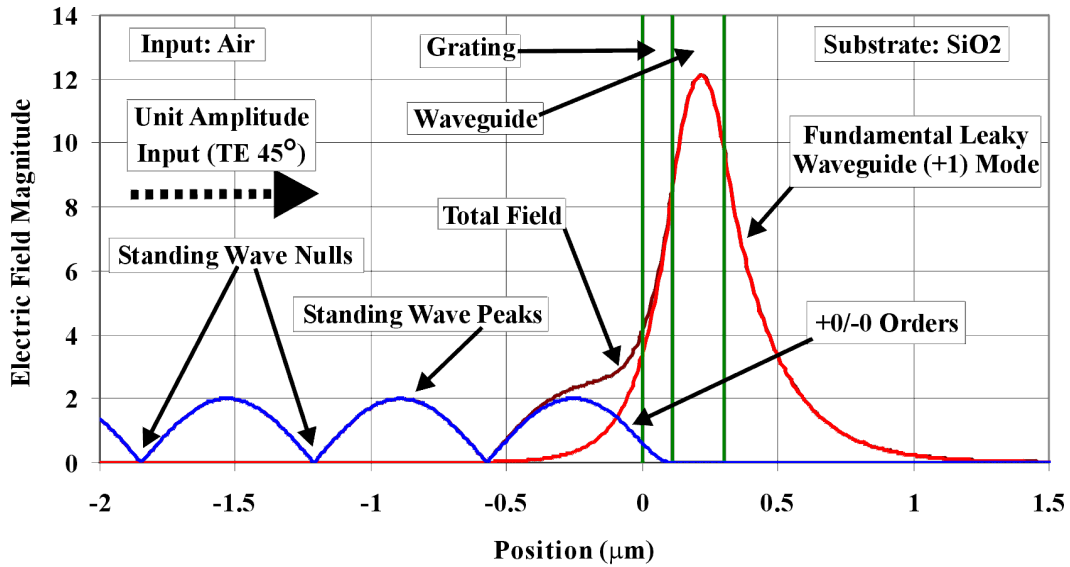
The basic ETMM algorithm provides amplitudes of reflected and transmitted waves corresponding to diffracted orders of the waveguide-grating structure. These reflected and transmitted amplitudes are then used to obtain the diffraction efficiency at the outer surfaces of the multilayer structure by simple ratio analysis of the real power carried by the incident, reflected, transmitted, and diffracted waves. A transmission (characteristic) matrix is constructed that represents the total electromagnetic coupling between various diffracted (propagating and evanescent) orders of the waveguide-grating structure by providing phase matching between the diffracted orders at each interface of the multilayer structure. By applying boundary conditions at each interface and solving for the reflected and transmitted amplitudes of each diffracted order, the field amplitude response of the structure at the outer surfaces is obtained. In general, for this total solution, the actual field amplitudes within the multilayer structure are not calculated.

The modification performed for the work in this dissertation is implemented by retaining the intermediate partial solutions at each boundary layer obtained during construction of the original transmission matrix. Once the field response for the total structure has been obtained, the constant coupling coefficients between the various diffracted orders in each layer are easily determined. By using the constant coupling coefficients along with the intermediate boundary layer solutions, the electric field at any point in any layer can be efficiently calculated. This includes any point both normal to and along the grating structure, thus allowing determination of the electric fields within

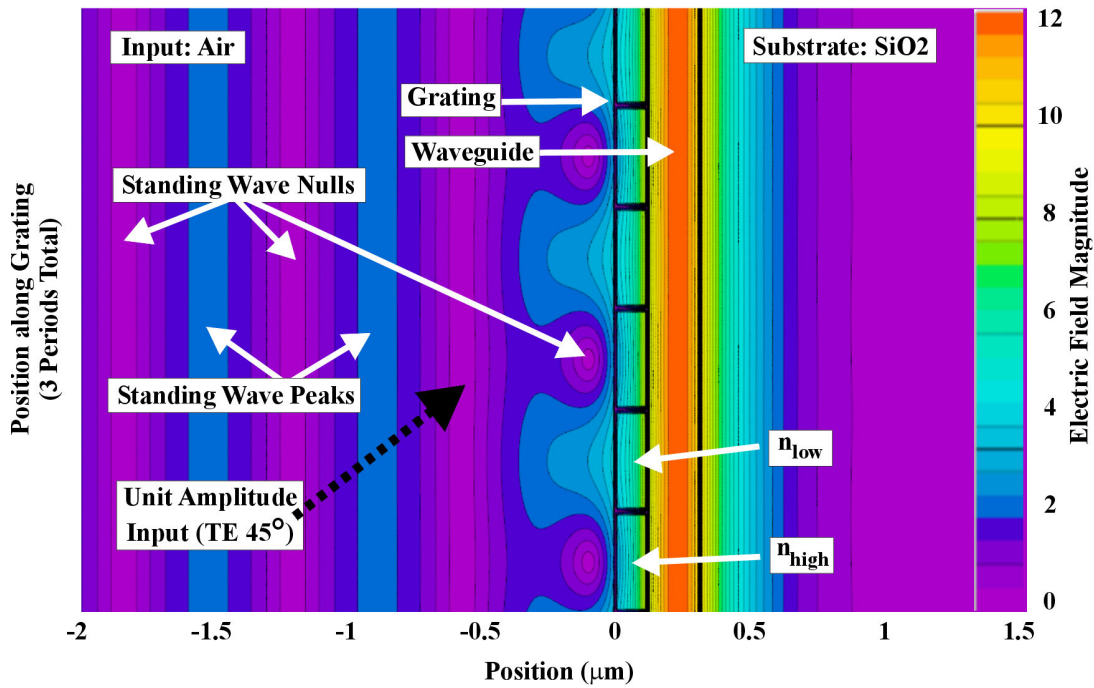
the periodic grating profile. Additionally, the temporal dependence of the monochromatic input is typically neglected during solution of the coupled wave equations. This temporal dependence can be reintroduced during calculation of the field solutions allowing visualization of the propagating electromagnetic fields.

Figure 2.5 provides a sample output from the modified ETMM RCWA code. This figure was obtained for the structure of Fig. 2.1 with grating period $\Lambda = 382$ nm and resonant input wavelength $\lambda_{\text{res}} = 901.85$ nm for a 45° angle of incidence. The curves of Fig. 2.5 (a) show the electric field magnitude (averaged over one grating period) of the input and reflected waves (+0/-0 orders), the total field in the simulation space, and the fundamental leaky waveguide (+1) mode. The standing wave normal to the substrate is a result of constructive and destructive interference between the incident and reflected waves (+0/-0 orders). The analysis can also be performed on individual field orders to show their relative magnitudes at any position within the structure. The field plots clearly show the waveguide energy confinement of the GMR device as well as the exponential decay of the waveguide (+1) mode fields into the surrounding media. The waveguide confinement factor, grating coupling coefficient, and resonator quality factor Q can be determined from this numerical analysis.

The lower plot of Fig. 2.5(b) shows a 2-dimensional (2D) representation of the total electric field magnitude (the temporal phase dependence is not shown) across a section of three grating periods. This plot shows that null regions also occur immediately in front of the n_{high} portions of the grating layer. Note that Figures 2.5(a) and (b) are vertically aligned on the page to show correspondence of the field patterns in each figure.



(a)



(b)

Figure 2.5. Simulated field profiles for the GMR structure of Fig. 2.1 at resonance. The electric field magnitudes are based on the TE polarized unit-amplitude plane wave incident at 45° from the left. (a) Shows the average field magnitude over one grating period relative to the GMR structure. (b) Shows a top-down 2-D contour plot over three grating periods for the same structure. This figure shows the standing wave nulls both along and normal to the substrate. $\lambda_{\text{res}} = 901.85 \text{ nm}$. $\Lambda = 382 \text{ nm}$.

The modified ETMM RCWA allows generation of electric field plots similar to those obtained from finite difference time domain (FDTD) analysis for infinitely periodic structures under steady-state excitation [38]. The RCWA method reduces the calculation time to a small fraction of that required by FDTD analysis. In conventional FDTD analysis, a temporal excitation function is applied to a structure and the temporal response is calculated for a length of time sufficient for the electromagnetic waves to propagate through the simulation space. In the case of resonant structures under steady state excitation, the FDTD simulation must be conducted for many cycles of the fundamental input frequency (wavelength) to achieve the steady-state resonance condition. With the RCWA analysis method, steady-state resonance solutions for the entire structure are calculated directly. The specific steady-state temporal field distribution within the structure at resonance can then be calculated with a single cycle of the input frequency.

Figure 2.6 shows a simulation of the electric field in the same structure of Figures 2.1 and 2.5 for a single snapshot in time ($t=0$). This figure shows both the amplitude and phase of the total field within the simulation space. The distance between the field peaks in each region is a function of the refractive index in each region. The small amplitude (0.005) transmitted plane wave in the substrate region is due to very slight deviation of the simulation wavelength from the ideal resonance wavelength. When the simulation of Fig. 2.6 is repeated for several time steps, the fields can be seen to propagate showing the interaction between the various propagating waves.

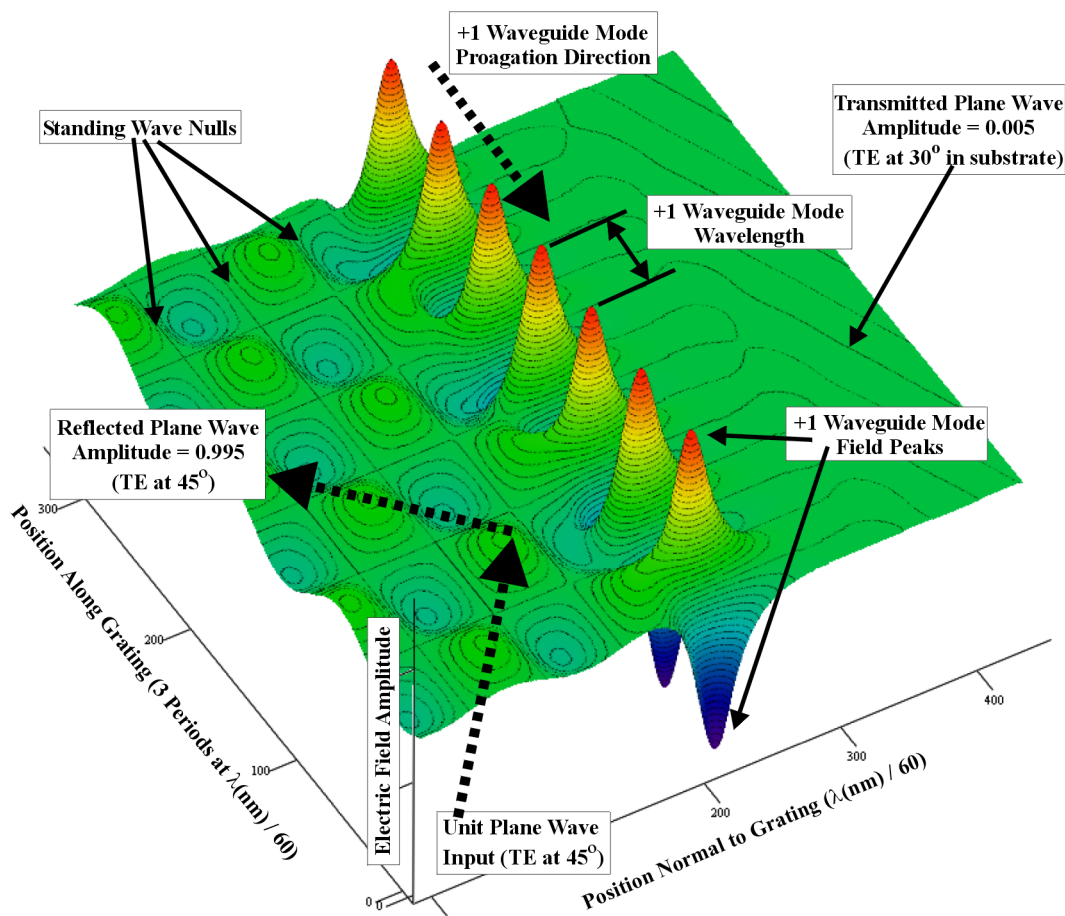
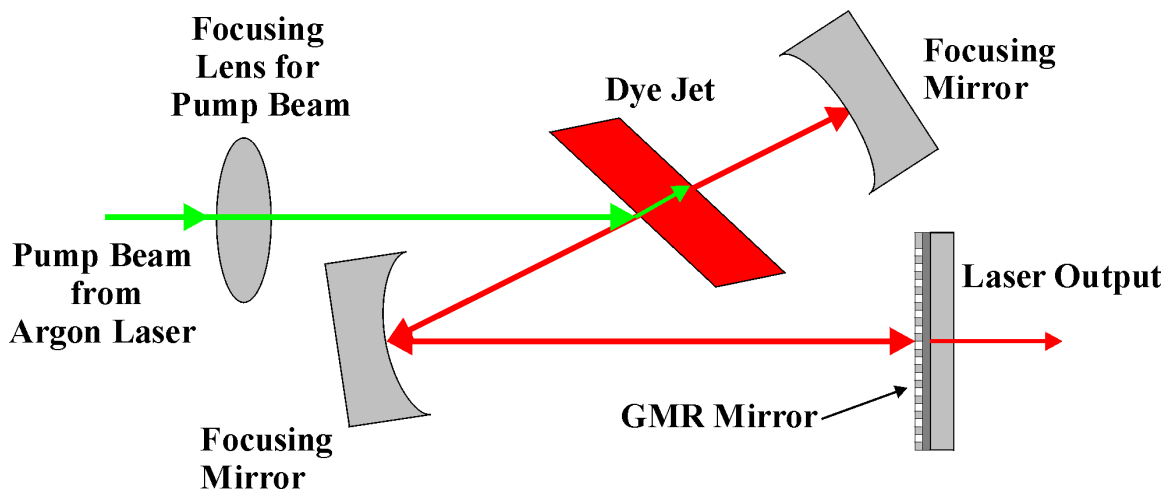


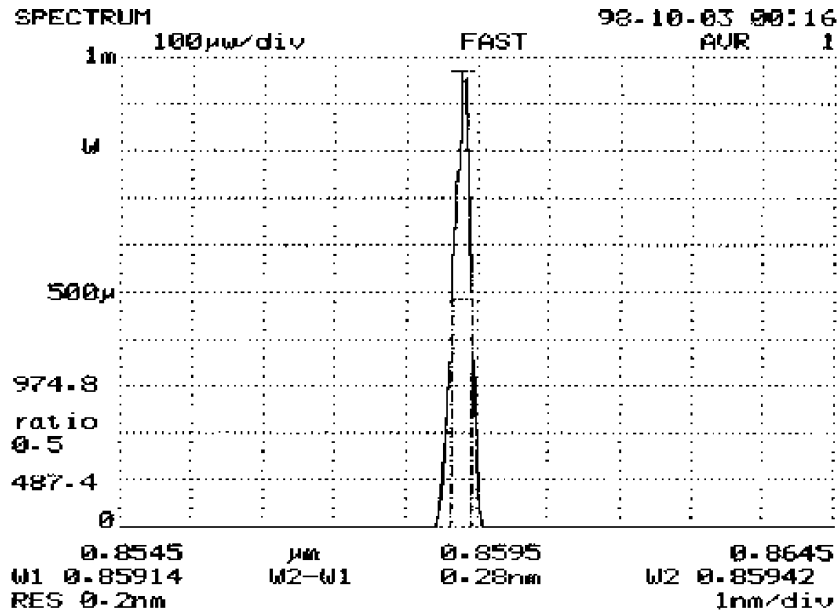
Figure 2.6. RCWA simulated total electric field profile at time $t=0$ for structure of Fig. 2.1 with simulation parameters of Fig. 2.5. This figure shows both the amplitude and phase of the total field along three grating periods. ($\lambda_{\text{res}} = 901.5$, $\Lambda = 382\text{nm}$, incident angle = 45°).

2.3 Ti:Sapphire Lasers with GMR Output Couplers

GMR mirrors have been demonstrated previously as output couplers in dye [8-11] and Ti:Sapphire lasers. This is shown schematically in Fig. 2.7(a). The output coupler is fixed at normal incidence to the laser cavity, thus providing monochromatic laser output at the GMR resonance wavelength. The measured output spectrum from an optical spectrum analyzer is shown in Fig. 2.7(b). From previous analysis, it is estimated that the GMR filter has a reflectivity of approximately 95% [7-11].



(a)



(b)

Figure 2.7. Schematic and measured output spectrum for a dye laser cavity using a GMR mirror as the output coupler. (a) The GMR mirror is mounted at normal incidence giving fixed monochromatic output. (b) The output spectrum of the dye laser is shown to have a FWHM of 0.28nm at $\lambda_{res} = 859.5$ nm.

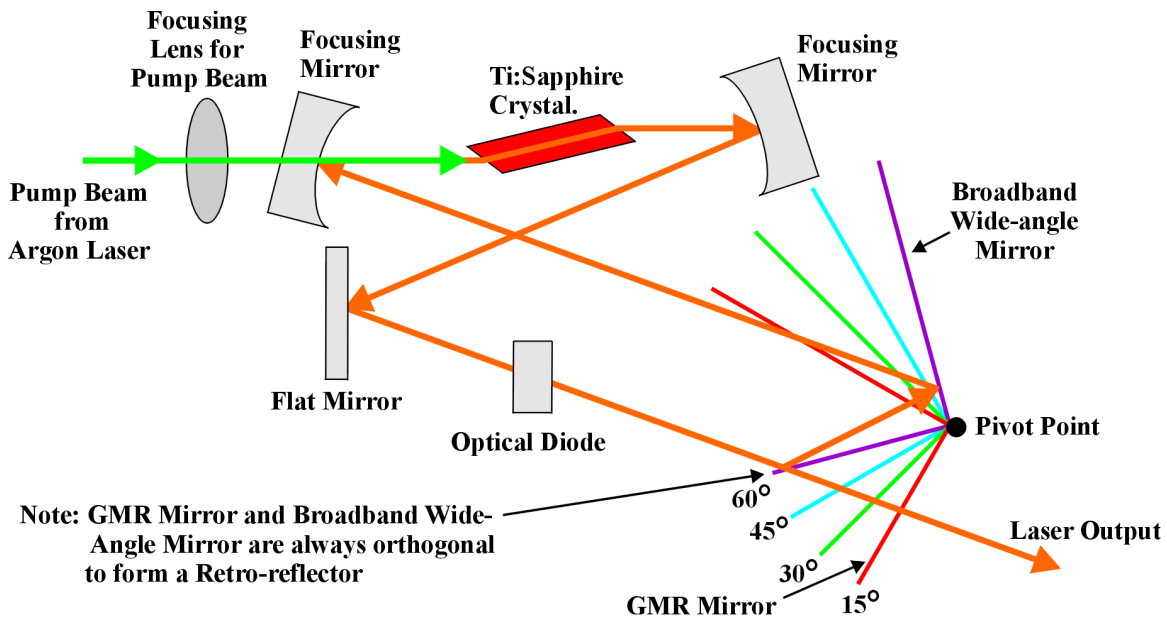


Figure 2.8. Schematic of a practical Ti:Sapphire unidirectional ring laser cavity using optimized components. The GMR mirror is mounted as one arm of a retro-reflector corner mirror. The configuration is shown with the GMR positioned at 60° corresponding to an output wavelength near 957 nm. The optical diode consists of a Faraday rotator and a half wave plate.

The angular dispersion characteristic of GMR mirrors as shown in Fig. 2.4 can also be utilized to allow tuning of the laser output wavelength. A schematic of a Ti:Sapphire laser incorporating a GMR mirror in a corner reflector configuration is shown in Fig. 2.8. As the corner reflector is rotated, the angle of incidence for the GMR mirror varies, thus the peak reflectivity wavelength of the cavity follows the GMR resonance wavelength. The GMR mirror serves as the output coupler as well as the tuning mechanism. The laser output linewidth is determined by the linewidth of the GMR reflectivity that exceeds the minimum reflectivity required for the laser to reach lasing threshold (typically 95% to 98%). This laser cavity configuration is similar to conventional Ti:Sapphire ring laser configurations that use a quartz plate birefringent filter as a tuning element.

The optical diode (optical isolator) shown in Fig 2.8 is included to provide unidirectional light propagation around the laser ring cavity. This element consists of an optical Faraday rotator and a half-wave plate. The Faraday rotator consists of a magneto-optic material (typically terbium-doped borosilicate glass or a terbium-gallium-garnet crystal (TGG) for Ti:Sapphire laser applications [90]) placed in a strong magnetic field. Linearly polarized light passing through the Faraday rotator in either direction experiences polarization rotation perpendicular to the magnetic field. For a conventional polarization rotator such as a birefringent quartz half-wave plate, the direction of polarization rotation is dependent on the direction of propagation through the crystal.

By combining the Faraday rotator with a second polarization-rotating element (birefringent quartz half-wave plate), with proper alignment, the polarization rotation due to the Faraday rotator can be completely compensated, thus resulting in zero net polarization rotation for light propagation through the device in one direction. For light propagation in the opposite direction, the quartz plate provides an initial polarization rotation, and the Faraday rotator provides an additional rotation in the same direction. The optical diode is used routinely in Ti:Sapphire ring laser configurations where many components are aligned at the polarization-dependent Brewster's angle to minimize reflection losses in the laser cavity. For the specific tunable Ti:Sapphire laser design shown in Fig. 2.8, the polarization dependence of the GMR mirror only allows high reflectivity for TE linearly polarized light within the operating wavelength range.

In laser cavities using GMR mirrors as tunable output couplers, the GMR sideband response is not critical. The peak reflectivity characteristic of the GMR mirror

determines the laser output characteristic. From Fig. 2.4, the GMR mirror configuration can provide approximately 150 nm of tunability in a very compact configuration. This is a considerable improvement in tunability over compact designs employing birefringent or piezo-electric tuning elements [33]. The unidirectional ring laser configuration of Fig. 2.8 can also be converted to a standing-wave laser configuration by omission of the optical diode. In this case (as with conventional standing-wave Ti:Sapphire ring laser configurations), two laser output beams emerge from the output coupler (each corresponds to the incident direction on the output coupler.)

CHAPTER 3

GUIDED-MODE RESONANCE SURFACE-EMITTING LASER DESIGN, WAFER CHARACTERIZATION, AND DESIGN OPTIMIZATION

Guided-mode resonance (GMR) devices have been proposed as enabling structures for high-performance surface-emitting lasers [1, 7, 12]. This new class of lasers provides surface-emitting lasers (SELs) with improved resonator gain and single wavelength output in a horizontal-cavity distributed feedback (DFB) or distributed Bragg reflector (DBR) structure. In this chapter, the design of an optically pumped guided-mode-resonance surface-emitting laser (GMR-SEL) is presented.

3.1 Preliminary GMR-SEL Design Analysis

The GMR surface-emitting laser (GMR-SEL) design process is begun by selecting the appropriate material system based on the desired operating wavelength. For the designs and analysis presented in this work, the laser operating wavelength is near 980 nm allowing use of the GaAs/Al_xGa_{1-x}As material system utilizing an In_{0.2}Ga_{0.8}As strained quantum well for the light-emitting layers. This well-characterized material system has been used extensively for both edge-emitting and surface-emitting laser designs [40-46]. The GMR-SEL design was then based on the nominal refractive indices at the operating wavelength [47].

To demonstrate proof-of-concept operation of a semiconductor GMR-SEL, a simplified optically-excited (pumped) structure was chosen. Since the device is optically pumped,

all semiconductor layers are undoped. A schematic of the GMR-SEL structure is shown in Fig. 3.1. The design employs 810 nm resonant pumping at an oblique input angle. To minimize optical losses in the waveguide, grating, and cladding layers, the AlGaAs layers must have aluminum content sufficient to place the layer band gap energy above that of the 810 nm pump wavelength. All layers except for the quantum-well structure and substrate are transparent at the 810 nm pump wavelength. The only layer with optical absorption at the 980 nm operating wavelength is the quantum-well. Under lasing conditions this quantum well layer is saturated to transparency, therefore subsequent analysis assumes the quantum well is lossless.

Figure 3.1 also shows the resonant gain path for the GMR-SEL that satisfies both a horizontal and vertical resonance. The $\text{In}_{0.2}\text{Ga}_{0.8}\text{As}$ quantum-well layer produces 980nm light near the center of the waveguide. At resonance, this light is emitted into the fundamental leaky waveguide modes. This light is coupled out of the GMR waveguide-grating structure and is incident on the lower 20-period GaAs/AlAs Bragg mirror in this example; other types of mirrors can be used. This light is then reflected back into the GMR structure further enhancing the fundamental leaky waveguide modes. The laser output is due to residual transmission of the light not reflected by the GMR structure.

For this design, $\text{Al}_{0.2}\text{Ga}_{0.8}\text{As}$ with a 741 nm bandgap cutoff wavelength for optical transparency was chosen for the waveguide-grating structure. AlAs was chosen for the cladding / substrate spacer layer. This presents the largest possible refractive index

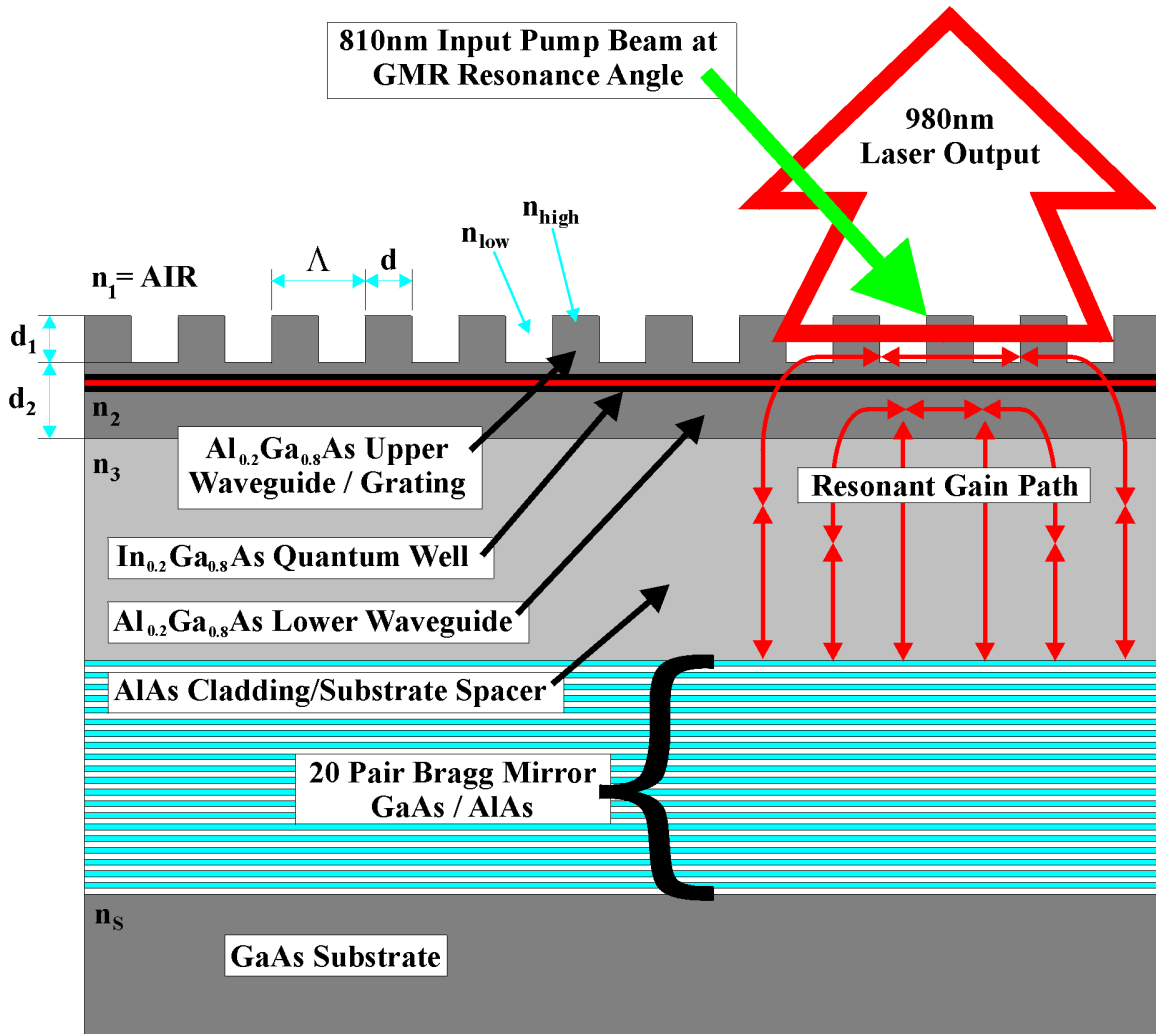


Figure 3.1. Schematic of GRM-SEL structure with 980 nm laser output using 810 nm GMR resonant optical pumping. The enhanced resonant gain path satisfies both a horizontal and vertical resonance. 980nm light is produced in the $\text{In}_{0.2}\text{Ga}_{0.8}\text{As}$ quantum-well layer. At resonance, this light is emitted into the fundamental leaky waveguide modes. Light coupled out of the GMR waveguide-grating structure is incident on the lower 20-period GaAs/AlAs Bragg mirror. This light is reflected back into the GMR structure further enhancing the fundamental leaky waveguide modes. The laser output is due to residual transmission of the light not reflected by the GMR structure.

contrast between the waveguide and cladding while also maintaining waveguide transparency to the pump wavelength. The substrate spacer layer thickness is a critical design parameter for the GMR-SEL design.

The spacer layer provides the proper phase between GMR mirror and lower Bragg mirror as well as minimizes substrate coupling losses. This layer must be sufficiently thick to prevent coupling of the GMR-SEL waveguide modes into the substrate. The required thickness of the substrate spacer layer can be reduced by increasing the waveguide thickness or refractive index contrast between the waveguide and cladding. The maximum waveguide thickness is limited by the single-mode cutoff thickness at the operating wavelength. For practical GMR-SEL designs, the AlAs substrate spacer thickness is approximately $1\mu\text{m}$.

The basic strained quantum-well light-emitting layers consist of an 8.0 nm $\text{In}_{0.2}\text{Ga}_{0.8}\text{As}$ layer sandwiched between two 10 nm GaAs barrier layers. The barrier layer thickness above approximately 10 nm is not critical. Typical thickness values range up to 25 nm [43], but for this optically pumped design, the GaAs layer represents an optical loss causing increased heating at the 810 nm pump wavelength. This quantum-well structure is used as-is in this work and no further theoretical analysis is performed.

The lower Bragg stack mirror in this design example consists of alternating quarter-wavelength high and low refractive index material. This mirror design typically exhibits high reflectivity over a broad spectral range. The spectral bandwidth, angular sensitivity, and peak reflectance, is determined by the refractive index contrast between the two material types and the total number of alternating high-low periods [48]. The

integrated Bragg mirror of Fig. 3.1 is implemented with 20-pair of GaAs/AlAs quarter-wavelength (at $\lambda = 980$ nm) layers and exhibits a 99.53% peak reflectivity.

3.2 Initial GMR-SEL design

GMR mirror structures operating at normal incidence satisfy the second-order Bragg condition given by (3.1). This equation gives the conditions for which incident

$$\lambda_o = \frac{2\Lambda n_g}{m}, \quad m = 1, 2, 3, \dots \quad (3.1)$$

light with wavelength λ_o is reflected through 180° by a periodic medium with refractive index n_g and period Λ for each Bragg order m . A rough approximation for the GMR grating period can be obtained by simple solution of (3.1) using the nominal refractive index for an unperturbed waveguide. In this case, for a desired GMR resonance wavelength of 980 nm in $\text{Al}_{0.2}\text{Ga}_{0.8}\text{As}$ ($n_g = 3.4$) and second-order diffraction, the grating period is approximately 290 nm. This also corresponds to the approximate coupled-wave analysis of weakly perturbed waveguides given by [49]. Based on the fabricated grating profiles as shown in Chapter 4, a 1:1 aspect ratio of grating depth to width is a practical fabrication goal for wet-etched gratings in GaAs.

Since the waveguide-grating structure includes an embedded quantum-well, the maximum grating etch depth was limited to within approximately 20 nm from the quantum-well layers to avoid damage. For this design with an approximate 290 nm grating period, a 1:1 depth aspect ratio dictates a 145 nm maximum etch depth. After including the 20 nm clearance between the bottom of the grating and the quantum-well layers, the top waveguide thickness then becomes approximately $d_1 = 165$ nm.

An initial estimate for the overall waveguide-grating thickness is obtained by assuming the quantum-well layers are centered within the waveguide. Using an effective-medium approximation for the grating structure, (and assuming a 50% grating fill factor), the grating equivalent layer thickness is approximately 73 nm. After including approximately 15 nm for half of the quantum-well / barrier thickness, the initial lower waveguide thickness is estimated to be approximately $d_2 = 85$ nm.

At this point, a simple slab waveguide analysis was performed on the preliminary waveguide structure to insure single-mode operation. For a slab waveguide laser structure, single-mode operation at the operating wavelength is assumed in this dissertation. Key equations for this analysis [22] are given by (3.2), (3.3), and (3.4).

$$V = \frac{2\pi t_g}{\lambda} \sqrt{n_2^2 - n_3^2} \quad (3.2)$$

$$a_{TE} = \frac{n_3^2 - n_1^2}{n_2^2 - n_3^2} \quad (3.3)$$

$$V\sqrt{1-b} = m\pi + \tan^{-1} \sqrt{\frac{b}{1-b}} + \tan^{-1} \sqrt{\frac{b+a_{TE}}{1-b}} \quad (3.4)$$

Equation (3.2) gives the well-known expression for normalized waveguide frequency in terms of the operating wavelength λ , the effective waveguide thickness t_g , and the waveguide and substrate refractive indices n_2 and n_3 . (3.3) defines the asymmetry parameter a_{TE} used in the normalized waveguide dispersion relation given by (3.4). This dispersion relation is defined in terms of the asymmetry parameter in the waveguide a_{TE} , the normalized guide index b , and the normalized frequency V . Solving (3.2) for the initial $\text{Al}_{0.2}\text{Ga}_{0.8}\text{As}$ ($n_2 = 3.4$, $t_g = 250$ nm) waveguide estimate and AlAs ($n_3 = 2.97$)

substrate yields $V = 2.64$. Since $V < \pi$, the waveguide supports only the fundamental mode. (3.4) can then be solved to obtain the various other waveguide parameters including the mode propagation constant, guide wavelength, Goos-Hanchen shifts, and effective waveguide thickness. A Mathcad worksheet for solving these equations is given in the Appendix.

The initial waveguide parameters are now used for an iterative analysis and optimization using the modified RCWA software described in Chapter 2. The initial GMR structure is given in Table 3.1. The analysis can be first conducted for only the GMR waveguide-grating structure. During GMR-SEL operation, light emitted from the GMR waveguide-grating is reflected back to the GMR with near 100% efficiency by the lower Bragg mirror. This can be equivalently modeled by assuming the light source is at the top layer of the Bragg mirror to simulate the GMR structure response for the reflected light. In turn, this is equivalently modeled by omitting the Bragg mirror from the analysis. The GMR structure effectively “sees” the incident light originating from a source located at the same distance as the substrate. The light incident on the GMR structure is effectively modeled as emanating from the top of the substrate interface. For the remaining analysis, the GMR-SEL structure is modeled as a passive GMR mirror and simply referred to as a GMR structure.

A final design consideration is that during growth of the GaAs/AlGaAs wafer structure, a thin GaAs cap layer is typically included if the topmost layer contains aluminum. This prevents aluminum oxidation when the wafer is removed from the growth chamber. This layer can be easily removed if necessary, however since the cap

layer is etched-through during grating fabrication, this layer contributes little to the overall structure. Effectively, this layer can remain as part of the GMR grating structure. All following analysis includes this GaAs cap layer. The initial GMR structure and design refractive indices [47] are given in Table 3.1.

Table 3.1. Initial GMR-SEL Design Parameters and Nominal Refractive Indices

Layer #	Material	Thickness	Refractive Index (at $\lambda = 980$ nm)	Comment
1	GaAs	20 nm	3.515	Cap
2	$\text{Al}_{0.2}\text{Ga}_{0.8}\text{As}$	70 nm	3.397	Grating
3	$\text{Al}_{0.2}\text{Ga}_{0.8}\text{As}$	70 nm	3.397	Top Waveguide
4	GaAs	10 nm	3.515	Barrier
5	$\text{In}_{0.2}\text{Ga}_{0.8}\text{As}$	8 nm	3.600	Well
6	GaAs	10 nm	3.515	Barrier
7	$\text{Al}_{0.2}\text{Ga}_{0.8}\text{As}$	80 nm	3.397	Bottom Waveguide
8	AlAs	1000 nm	2.966	Spacer
Substrate	GaAs	--	3.515	

3.3 RCWA Analysis of Initial GMR-SEL Design

The rigorous coupled-wave analysis (RCWA) described in Chapter 2 is now used to analyze and optimize the initial GMR structure of Table 3.1. The first step is to find the resonant wavelength of the GMR structure as a function of grating period. From the initial estimate, a series of RCWA analysis are performed to determine the sensitivity of the resonant wavelength to the grating period. The initial grating period estimate from the Section 3.2 is 290 nm. Additionally, the initial grating depth is assumed to be one half of the upper waveguide thickness. The GMR-SEL wavelength response as a function of grating period is shown in Fig. 3.2.

This figure shows that this GMR-SEL grating structure exhibits a resonant wavelength sensitivity of 29 nm wavelength shift per 10 nm increase in grating period.

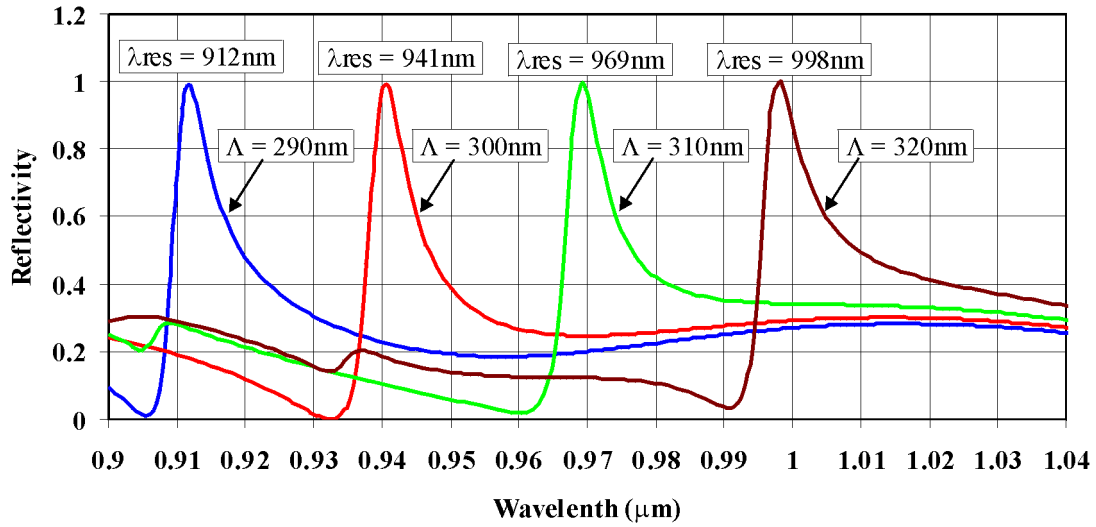


Figure 3.2. Simulated GMR-SEL response versus wavelength as function of grating period Λ for the structure of Table 4.1. The curves exhibit a resonant peak wavelength sensitivity of 29 nm wavelength shift per 10 nm increase in grating period. Parameters are: Grating Depth = 90 nm and Fill Factor = 0.5.

Based on these results, the GMR resonant peak will occur at 985 nm for a grating period of 314 nm. This value is then used to determine the resonant wavelength sensitivity as a function of grating depth. This response is shown in Fig. 3.3.

Fig. 3.3 shows that as the grating depth increases, the GMR resonant frequency is shifted toward shorter wavelengths. The resonant frequency dependence on grating depth is non-linear due to the change in effective waveguide thickness with increasing grating modulation. For the depth range given in Fig. 3.3, the resonance wavelength sensitivity is an average of 4.5 nm shift in resonant wavelength per 10 nm change in grating depth. Qualitatively, as the grating depth increases, the overall waveguide thickness is reduced thus decreasing the waveguide cutoff frequency.

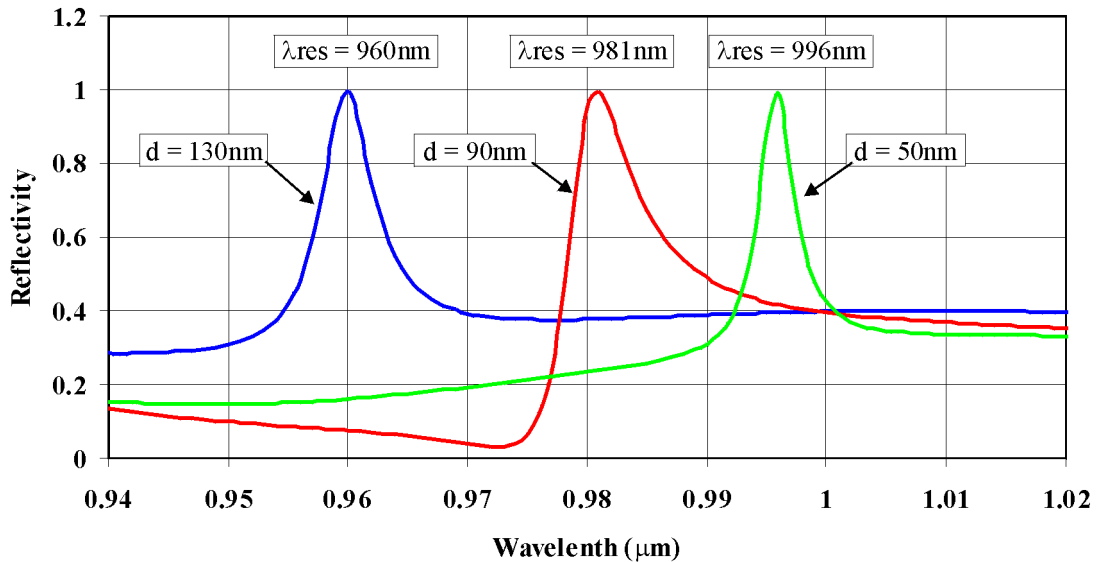


Figure 3.3. Simulated GMR-SEL response versus wavelength as function of grating depth d_1 for the structure of Table 3.1. The curves exhibit a resonant peak wavelength sensitivity of approximately 4.5 nm wavelength shift per 10 nm increase in grating depth. Parameters are: Grating Period = 314 nm and Fill Factor = 0.5.

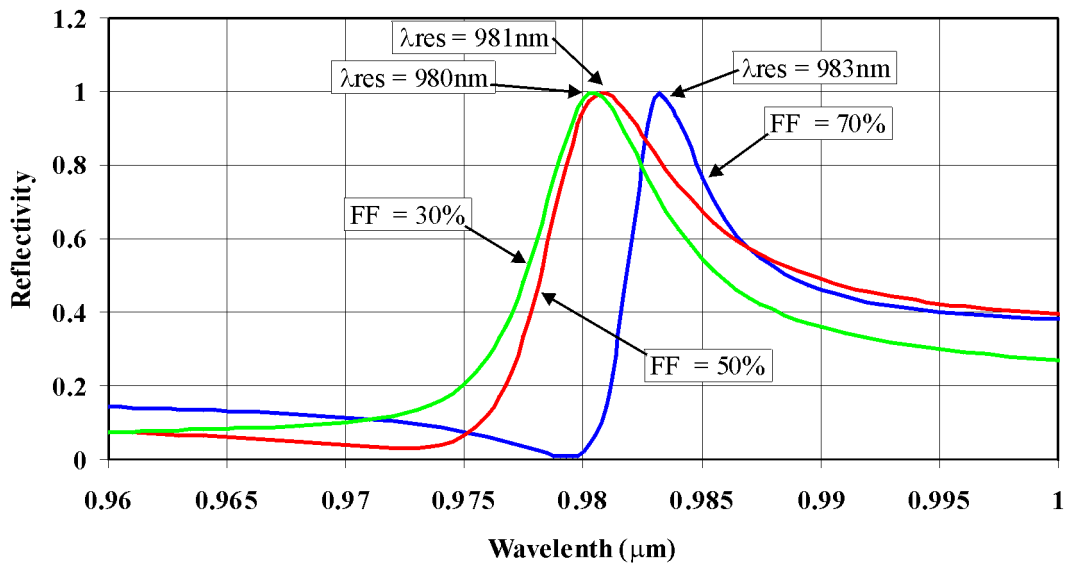


Figure 3.4. Simulated GMR-SEL response versus wavelength as function of grating fill factor for the structure of Table 3.1. The curves exhibit only a small shift in resonant peak wavelength for changes in grating fill factor. The results show that there is only a 3 nm shift between 30% and 70% fill factors in this case. Parameters are: grating period = 314 nm, and grating depth = 90 nm.

A similar effect occurs for the wavelength dependence of the GMR structure as a function of grating fill factor. Fig. 3.4 shows the change in resonant frequency with increasing fill factor. The figure shows that there is little change in the resonant frequency between 50% and 30% fill factors (1 nm total shift.) Additionally, the resonant frequency shift is only approximately 3 nm between 30% and 70% fill factors. The simulation results of Figures 3.2 through 3.4 clearly indicate that the grating period is the dominant parameter in setting the GMR structure resonant frequency.

The grating depth is the second most dominant parameter in controlling the GMR peak resonant frequency. Again, virtually all post wafer-growth tunability of the GMR-SEL structure is through variation of the grating period and depth. The grating fill factor has little effect on the operating frequency however the resonance linewidth, and as shown in the following fields analysis, the peak fields in the GMR under resonance conditions are affected.

3.4 RCWA Fields Analysis of Initial GMR-SEL Design

The next step in the design analysis of the GMR-SEL layer structure is by performing an RCWA electric fields analysis on the layer structure. One key requirement for the GMR-SEL design of Table 3.1 is proper thickness of the AIAs substrate spacer layer. Fig. 3.5 shows a plot of the electric fields as a function of position in the GMR-SEL layer structure. The relative field strengths are based on a unit-amplitude normally-incident plane wave (UANIPW) emanating from a plane inside the substrate. The plot shows the peak fields generated in the GMR waveguide-grating at resonance. These

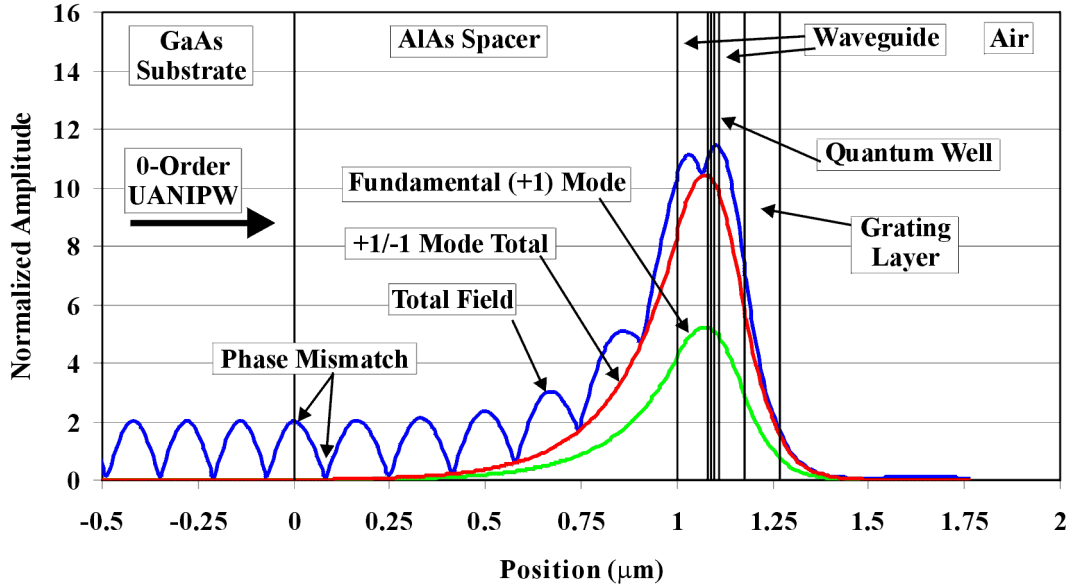


Figure 3.5. Plot of electric fields as a function of position in the GMR-SEL layer structure. The relative field strengths are based on a unit-amplitude normally-incident plane wave (UANIPW) emanating from a point inside the substrate. The plot shows the peak fields generated in the GMR waveguide-grating at resonance. These include the +1 propagating waveguide mode, the total standing waveguide mode field, and the total fields in the simulated structure. The phase mismatch due to incorrect spacer layer thickness is indicated. Simulation parameters are: Grating Period $\Lambda = 314$ nm, Grating Depth $d_1 = 90$ nm, Fill Factor = 0.5, and Resonant Wavelength $\lambda_{\text{res}} = 981$ nm.

include the +1 propagating waveguide mode, the total standing waveguide mode field, and the total fields in the simulated structure.

The fundamental (+1 and -1) counter-propagating waveguide modes have identical amplitudes for resonance at normal incidence, and the total of these propagating modes is shown. A standing wave is produced by interference of the incident and reflected zero-order modes. This standing wave is superimposed on the waveguide modes which decay exponentially outside the waveguide-grating structure. The mismatch of this standing wave with respect to the GaAs substrate / AlAs spacer layer

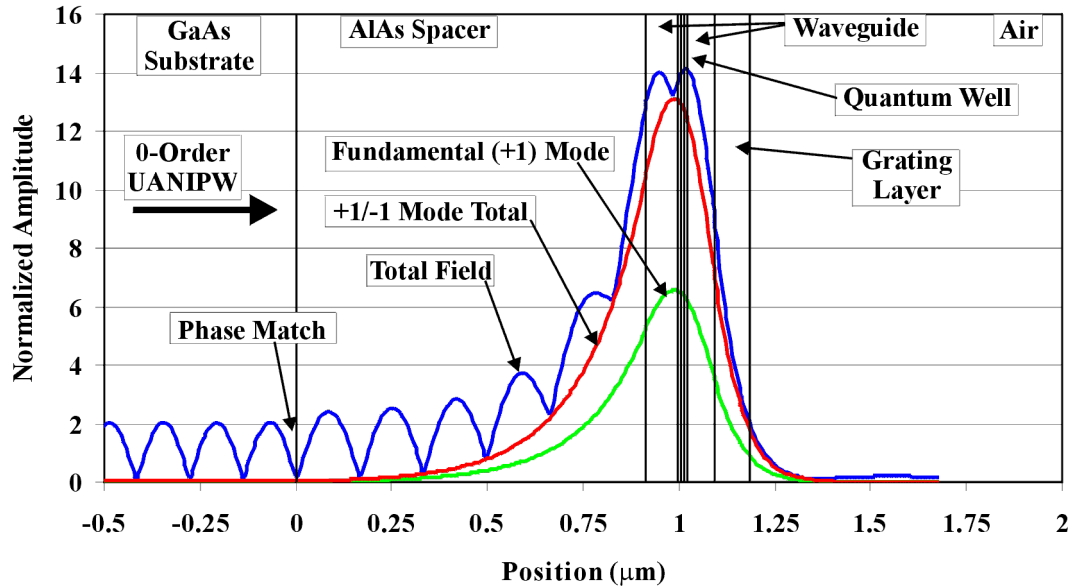


Figure 3.6. Plot of electric fields as a function of position in the GMR-SEL layer structure for adjusted spacer layer thickness. The Total Field curve shows that the phase mismatch at the substrate interface has been corrected by reducing the spacer layer thickness to 912 nm. The simulation parameters are the same as those of Fig. 3.5.

interface due to incorrect spacer layer thickness is indicated. The substrate spacer thickness is reduced to 912 nm and the simulation is repeated to yield the plot of Fig. 3.6.

The results of Fig. 3.6 show that the fields of Fig. 3.5 are essentially unchanged with the exception of the phase mismatch at the substrate / spacer layer interface. The total field curve shows that the null of the standing wave is now located at the substrate interface which is the identical to the reflection that occurs at the top layer of a periodic Bragg mirror. The vertical cavity length (normal to the substrate) set by the AlAs layer is now an integer multiple of half-wavelengths away from the zero-phase reflection plane of the GMR structure. This is the desired operating condition for the GMR-SEL in which both the vertical [37] and horizontal resonance conditions are satisfied. A summary of

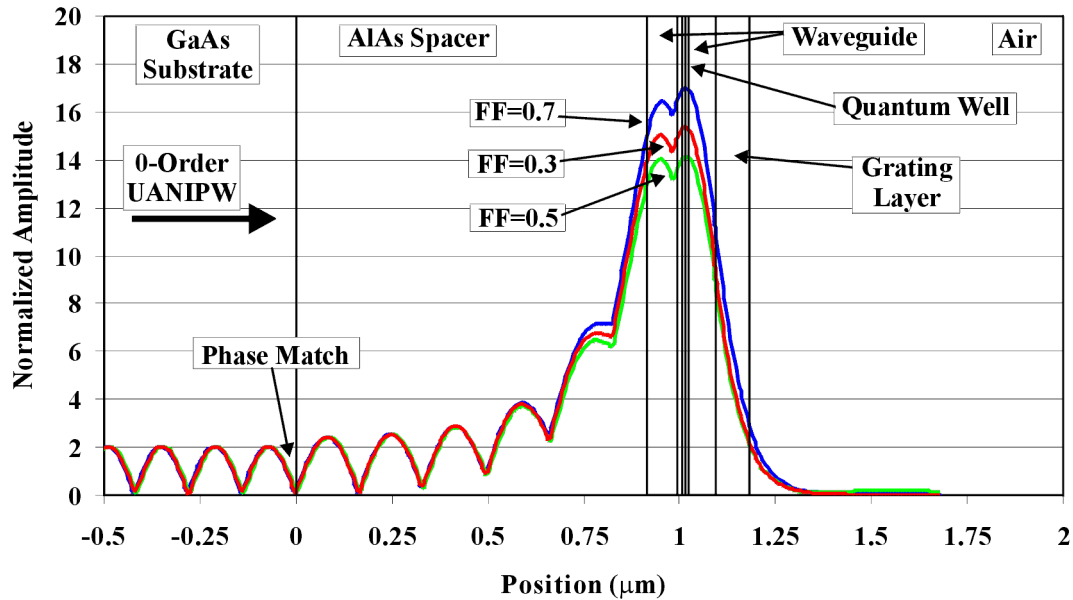


Figure 3.7. Plot of total electric fields as a function of position in the GMR-SEL layer structure showing the effect of variation in grating fill factor. Fill factor values range between 0.3 and 0.5. The resonant wavelengths corresponding to each fill factor are given in Fig. 3.4. The Total Field curves show that only difference between the curves is that the peak field in the waveguide is minimized for 50% fill factors and increases for 30% and 70% fill factors. The phase mismatch at the substrate interface remains at zero. The simulation and grating parameters are the same as those of Fig. 3.5.

the final structure is given in Table 3.2. Final analysis consists of variation of parameters to insure GMR-SEL operation for the widest possible range of fabricated grating parameters. An example of variation in grating fill factor is shown in Fig. 3.7.

The simulation of Fig. 3.7 was performed for the structure of Table 3.2 with the fill factor varied between 0.3 and 0.7. The GMR resonant frequencies of Fig. 3.4 corresponding to each fill factor value were used to calculate the fields within the structure. Fig. 3.7 shows that the only change in the resonance conditions (other than resonant frequency) is the overall peak amplitude of the propagating waveguide modes. The results show that for this particular structure, the peak waveguide fields are a

minimum for the $FF = 0.5$, while the total fields at resonance slightly increase for 30% and 70% fill factors. The phase of the standing wave at the substrate interface is nearly zero for each case.

For the final steps of the design process, an analysis is performed at the 810 nm pump wavelength as shown in Fig. 3.8. The thin GaAs cap layer and quantum well barrier layers are absorptive at the 810 nm pump wavelength. The initial pump wavelength analysis is performed assuming all GMR layers materials are lossless. This allows the resonant angle at the pump wavelength to be determined for a given grating period and layer parameters. The optical loss terms can then be included in subsequent

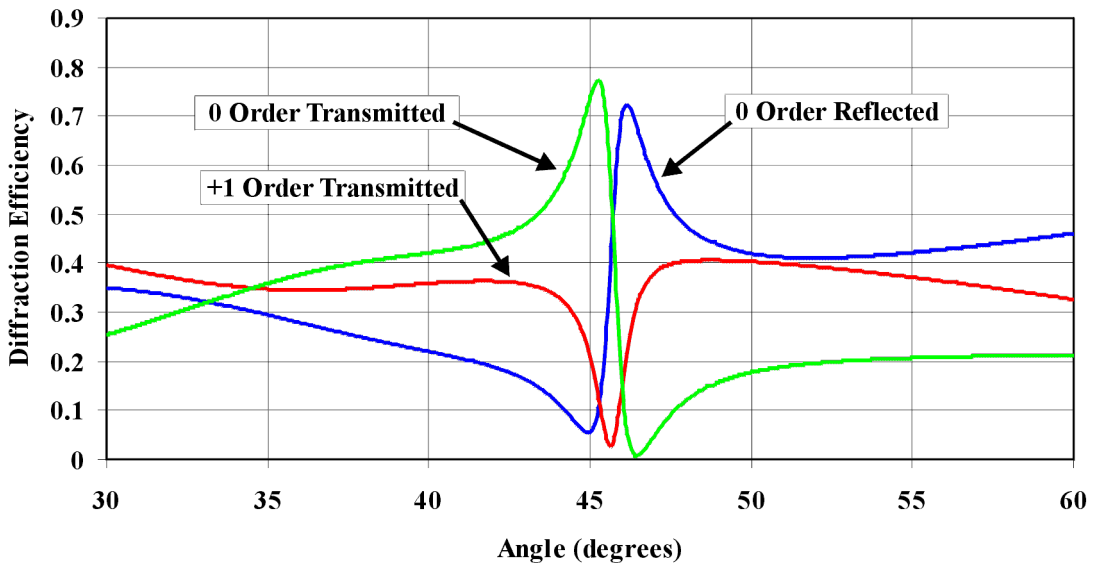


Figure 3.8. Diffraction efficiency response of the basic GMR-SEL structure of Table 3.2 for 810nm TE polarized illumination. The incident wave is from the top (air). This simulation assumes no optical absorption in quantum well layers. Note that for oblique illumination at 810nm, the +1 transmitted order is propagating, thus reducing the optical pump efficiency. Simulation parameters are: $\Lambda = 314$ nm and $\lambda = 810$ nm The zero order reflection resonance occurs at: $\theta_{res} = 46.2^\circ$.

analysis to determine the field enhancement in the waveguide due to resonant pumping. Note that the waveguide-grating now allows propagation of the +1 diffracted order for the shorter pump wavelength and grating period. The energy in this order is lost and results in slightly reduced optical pumping efficiency.

3.5 Summary of GMR-SEL design

The basic GMR laser structure without integrated substrate reflector is given in Table 3.2. A full design for an optically-pumped GMR-SEL with integrated Bragg mirror is given in Table 3.3. The Bragg mirror is positioned at an integral half

Table 3.2. Basic GMR-SEL Structure

Layer #	Material	Thickness	Refractive Index (at $\lambda = 980$ nm)	Comment
1	GaAs	20 nm	3.515	Cap
2	Al _{0.2} Ga _{0.8} As	60 nm	3.397	Grating
3	Al _{0.2} Ga _{0.8} As	80 nm	3.397	Top Waveguide
4	GaAs	10 nm	3.515	Barrier
5	In _{0.2} Ga _{0.8} As	8 nm	3.600	Well
6	GaAs	10 nm	3.515	Barrier
7	Al _{0.2} Ga _{0.8} As	80 nm	3.397	Bottom Waveguide
8	AlAs	912 nm	2.966	Spacer
Substrate	GaAs	--	3.515	

Table 3.3. Full GMR-SEL Structure with Integrated Bragg Mirror

Layer #	Material	Thickness	Refractive Index (at $\lambda = 980$ nm)	Comment
1	GaAs	20 nm	3.515	Cap
2	Al _{0.2} Ga _{0.8} As	60 nm	3.397	Grating
3	Al _{0.2} Ga _{0.8} As	80 nm	3.397	Top Waveguide
4	GaAs	10 nm	3.515	Barrier
5	In _{0.2} Ga _{0.8} As	8 nm	3.600	Well
6	GaAs	10 nm	3.515	Barrier
7	Al _{0.2} Ga _{0.8} As	80 nm	3.397	Bottom Waveguide
8	AlAs	912 nm	2.966	Spacer
9	GaAs	70 nm	3.515	$\lambda/4$ High Index
10	AlAs	83 nm	2.966	$\lambda/4$ High Index
11-48		153 nm	--	Rest of 20 Period Bragg Mirror
Substrate	GaAs	--	3.515	

wavelength from the GMR layers to provide in-phase feedback to the GMR resonant mode. This was verified in the simulation results of Fig. 3.6. In summary, the design listed in Table 3.2 was used for the fabrication of the GMR-SEL Wafer #1 described in the following sections.

Surface relief GMR structures fabricated with semiconductor materials generally possess wide spectral bandwidths due to the large refractive index contrast between the grating structure and air. Figures 3.2 through 3.4 show the spectral resonant response for the basic GMR-SEL waveguide-grating structure of Table 3.2. Although the structure exhibits a spectral bandwidth FWHM of approximately 5 nm, lasing will only occur at wavelengths above the minimum reflectivity required for laser threshold. This threshold requirement is determined by the GMR reflectivity, quantum well gain characteristic, and bottom mirror reflectivity [7].

The full structure of Table 3.3 with high reflectivity lower Bragg mirror is an ideal integrated structure. The Bragg mirror requires significant crystal growth time, therefore the basic structure of Table 3.2 was chosen for initial fabrication. Since the substrate is transparent at the fundamental wavelength, the bottom mirror will first be implemented by depositing a thick layer of silver or gold. According to previous analysis, the minimum reflectivity of the lower substrate mirror is approximately 75% [7]. Alternate mirror configurations may be implemented by etching a window through the backside of the substrate followed by metal deposition in the exposed window.

GMR waveguide structures fabricated on high refractive index substrates require a thick spacer layer to minimize coupling of propagating waveguide modes into the

substrate. Energy lost to substrate coupling cannot be recovered and will degrade or even prevent active GMR device operation. RCWA is used to calculate the relative magnitudes of the evanescent fields in the spacer layer. From RCWA diffraction efficiency analysis, the calculated resonance peak will be reduced if energy is lost to the substrate. The peak resonance for simulated designs is approximately 100%. In practice, this high GMR reflectivity cannot be achieved due to imperfections in the waveguide-grating structure. This practical aspect of fabricated GMR structures allows surface emission by transmission through the active GMR mirror.

For the GaAs / AlGaAs laser structure in this work, the grating fill factor is assumed to be in the range of 0.3 to 0.5. This approximates the behavior of tapered grating profiles obtained by wet etching techniques. The average refractive index for arbitrary grating shapes of the same period can be approximated by decomposition of the grating profile into an appropriate number of thin rectangular gratings having the same grating period with different fill factors and starting positions within the grating period. Although not shown here, this simulation was performed for the basic structure of Table 3.2 with a trapezoidal grating and fill factors ranging from 60% to 30%. The resonant response was essentially identical to the response with a rectangular grating with 30% fill factor. The GMR wavelength response is relatively insensitive to fill factor variation between ~ 0.3 to ~ 0.5 . Additionally, variation in grating fill factor between 0.3 and 0.5 does not introduce significant phase mismatch at the GaAs substrate / AlAs spacer interface.

Post-growth tunability of the GMR laser structure is through etching. For this design with nominal refractive indexes and a fixed grating period (314 nm), the resonant wavelength can vary between approximately 975 nm to 995 nm as a function of etch depth (20 nm-100 nm) and top waveguide thickness. After the initial anisotropic etching of the grating structure (ideally 80 nm deep), if necessary, a second isotropic etch may be performed to reduce the overall grating and waveguide thickness. This allows a measure of further tunability to resonant wavelength and substrate reflection phase.

3.6 Laser Wafer Characterization

The critical parameters for fabrication of GMR-SEL lasers include material layer thickness and refractive index. All analysis in the design phase is based on the nominal refractive indexes and thicknesses of the waveguide-grating structure. Additionally, all design phases assume that the laser crystal structure is uniform. The as-grown laser wafer structure parameters typically deviate from the nominal design values thus requiring minor adjustments to the grating design parameters. Spectroscopic ellipsometry is main analysis method used in this work to determine layer thickness and refractive indices. Room temperature photoluminescence measurements are used to determine the gain characteristic of the quantum well structure. This measurement ensures overlap of the gain curve with the cavity resonance. The results of the characterization are then used to select the proper grating period, etch depth, and fill factor.

Due to the relatively slow MBE growth rates, the integrated lower Bragg mirror was omitted from the prototype designs to minimize the crystal growth time and cost.

Based on previous analysis [7], the reduced reflectivity requirements for the substrate mirror indicate that a simple metal mirror can be substituted for the Bragg mirror shown in Fig. 3.1 and described in Table 3.3. The first GMR-SEL device (Wafer #1) based on the design of Table 3.2 was MBE-grown by a commercial wafer foundry service on a two-inch GaAs substrate. The device design utilized a single AlAs substrate spacer layer

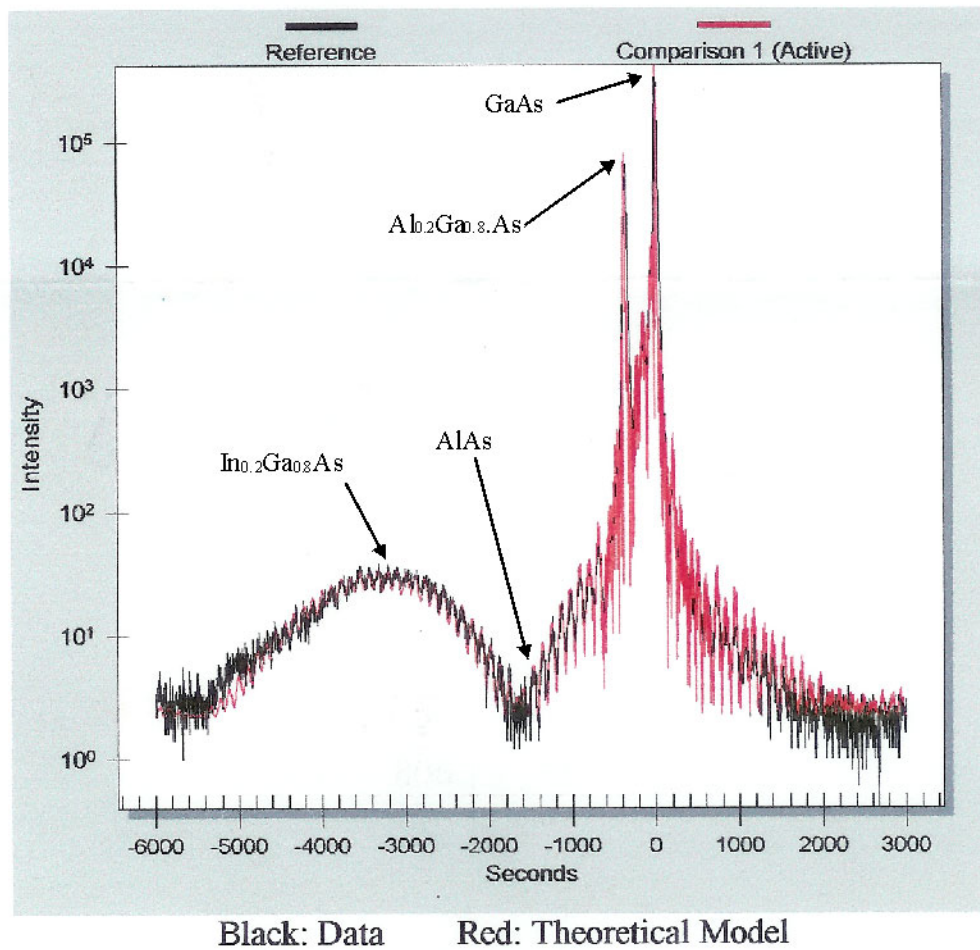


Figure 3.9. DCC X-Ray diffractometry results for commercial MBE-grown GMR-SEL laser wafer (Wafer #1). The curves show a close qualitative match between the design and grown layer parameters. The black data curve indicates that the grown layers are both single-crystal and epitaxial with the substrate.

approximately 915 nm thick to prevent evanescent coupling from the waveguide modes into the substrate. At the time of this first wafer growth, the commercial wafer foundry indicated that the relatively thick 915 nm AlAs spacer layer could be reliably grown as a single layer.

The wafer foundry provided the measured results and theoretical response of an in-house doubly-curved-crystal (DCC) X-ray diffractometry analysis shown in Fig. 3.9. Analysis parameters were based on electron wavelength $\lambda_e = 1.54056 \text{ \AA}$ using the 4th diffracted order reflected at a Bragg angle of 33.0250° . The curves are given in seconds of arc with the diffraction peak for GaAs centered at zero seconds. Well-defined peaks for the GaAs barrier and cap layers and $\text{Al}_{0.2}\text{Ga}_{0.8}\text{As}$ waveguide layers are shown with the broad peak near -3200 seconds corresponding to the $\text{In}_{0.2}\text{Ga}_{0.8}\text{As}$ strained quantum well. Lattice constants for GaAs, $\text{Al}_{0.2}\text{Ga}_{0.8}\text{As}$, AlAs, and bulk $\text{In}_{0.2}\text{Ga}_{0.8}\text{As}$ are 5.6533 \AA , 5.6548 \AA , 5.6600 \AA , and 5.8354 \AA respectively [50]. These crystal lattice constants correspond to peaks at angles of 0 seconds, -350 seconds, -1570 seconds, and -4150 seconds respectively. Although a peak for the lower AlAs substrate spacer layer does not appear in the curves of Fig. 3.9 at -1570 seconds, it can be inferred that this layer is single crystal and epitaxial to the substrate due to the strong signals obtained for the topmost wafer layers. Additionally, the peak corresponding to bulk $\text{In}_{0.2}\text{Ga}_{0.8}\text{As}$ that would normally occur near approximately -4150 seconds relative to GaAs is shifted to approximately -3200 seconds (5.7923 \AA) due to compressive strain. Finally, the measured data for Wafer #1 is well correlated with the given theoretical curve indicating good crystal quality and correspondence with the design material values.

Upon receipt of the grown Wafer #1, the layer thicknesses and refractive indices were measured with a spectroscopic ellipsometer. The spectroscopic ellipsometer measures the intensity of light reflected from the substrate layers at variable wavelengths, polarization, and angles of incidence [51]. The complex ratio ρ of the magnitudes and phases of the parallel and perpendicular-polarized reflected beams is given by (3.5).

$$\rho = \frac{R_p}{R_s} = \tan(\psi)e^{i\Delta} \quad (3.5)$$

The ratios of the magnitudes and phases for each polarization state are used to define the respective measured PSI (Φ) and Delta (Δ) of the layer structure. By numerical curve fitting of the measured PSI and Delta data, the thickness and refractive indices of the layer structure can be determined. The correlation (goodness of fit) between the numerical simulation and the measured data is given by the mean-squared error (MSE) between the two curves [51].

Table 3.4. shows a comparison between the design and fitted parameters for the as-grown structure of Wafer #1. The results indicate that the 905 nm AlAs spacer layer was approximately 5% thicker than expected, and the thicknesses of the upper and lower $\text{Al}_{0.2}\text{Ga}_{0.8}\text{As}$ waveguide layers were approximately 12% to 14% thinner than the design values. The results also show that the material nominal refractive indices used for the design differ by less than 1%. The effects of the minor variations in the thin strained $\text{In}_{0.2}\text{Ga}_{0.8}\text{As}/\text{GaAs}$ quantum-well layer thicknesses could not be assessed by spectroscopic ellipsometer analysis. The reduced overall waveguide thickness from the design values indicate that the design grating parameters required adjustment to allow overlap of the

Table 3.4. Ellipsometer Analysis Summary for GMR-SEL laser Wafer #1

Layer #	Nominal Material	Nominal Refractive Index	Design Thickness (nm)	Fitted Thickness (nm)	Fitted Refractive Index	Comments
8	GaAs-Oxide	--	--	1.1512±0.02	--	Surface Oxide
7	GaAs	3.515	20	23.073±0.17	3.516	Cap Layer
6	Al _{0.2} Ga _{0.8} As	3.397	140	123.31±0.45	3.385	Fitted Aluminum: x = 0.1749
5	GaAs	3.515	15	11.896±1.03	3.516	
4	In _{0.2} Ga _{0.8} As	3.600	7	9.6		Strained n, x not fitted
3	GaAs	3.515	15	22.739±0.98	3.516	
2	Al _{0.2} Ga _{0.8} As	3.397	80	68.602±0.44	3.388	Fitted Aluminum: x = 0.17092
1	AlAs	2.966	905	951.95±0.09	2.951	
Substrate	GaAs	3.515	--	--		S.I. substrate

Note: Refractive index values are estimated at 985 nm

Goodness of Fit for PSI data = 4.276 MSE.

GMR resonant mode with the quantum well gain spectrum. The quantum-well gain spectrum follows the spontaneous emission characteristic (photoluminescence) of the quantum well region.

A simple photoluminescence measurement setup using an optical spectrum analyzer (OSA) was constructed as shown in Fig. 3.10. It was found for the specific implementation of this configuration, difficulty in fiber coupling the wafer photoluminescence combined with the minimum sensitivity (10^{-9} Watts) of the OSA prevented clear measurement of the Wafer #1 photoluminescence. A second photoluminescence system was set up using a 0.9 m double grating spectrometer with a liquid nitrogen (LN₂) cooled Germanium detector. At this point, it was found that Wafer #1 had suffered catastrophic damage to the top wafer layers. The wafer surface exhibited

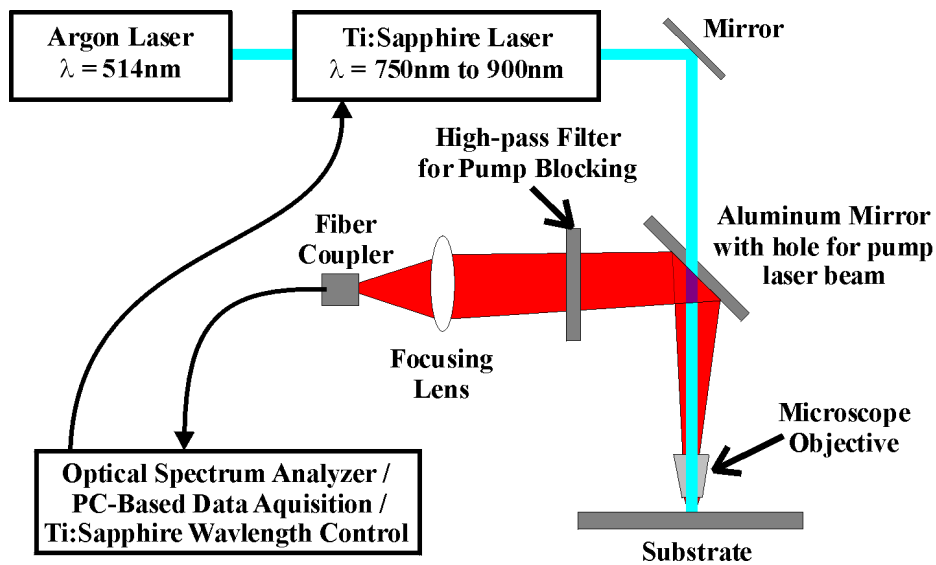


Figure 3.10. Schematic of basic photoluminescence (PL) setup for characterization of quantum-well structure under short and long wavelength illumination conditions. The long-wavelength illumination is provided to simulate the illumination conditions during GMR-SEL resonant pumping.

cracks, pitting, and large cloudy areas. This damage occurred despite the fact that the wafer had been stored in a vacuum.

The lattice constants of GaAs and AlAs are 5.6533 Å and 5.6600 Å respectively, with the $\text{Al}_x\text{Ga}_{1-x}\text{As}$ ternary compound values occurring within this range as a function of Aluminum content. Although the lattice matching between AlAs and GaAs is very close, a small amount of strain is present at an interface between these materials. Thick AlAs layers often suffer from nucleation processes during MBE growth resulting in defects and roughness in the topmost growth layers. For the GMR device of this work, these defects can induce strain in the bulk of the AlAs material as well as create a rough interface with the upper waveguide layer. Any roughness in the waveguide interfaces will result in

optical scattering losses that degrade device efficiency. The surface degradation of Wafer #1 is attributed to the induced strain of a single thick layer of AIAs.

3.7 Design Changes for GMR-SEL Wafer #2

When AIAs is grown on a GaAs wafer surface, the AIAs crystal molecules are initially in compressive strain. When thick layers of AIAs are grown, defects can occur which are manifested as wafer surface damage as occurred with GMR-SEL Wafer #1. One way to avoid the defects encountered for GMR-SEL Wafer #1 is by reducing strain in the thick AIAs substrate spacer layer of the design given in Table 3.2. This can be accomplished by inserting thin GaAs growth planarization layers in the AIAs layer. These 10-20 nm thin GaAs layers can improve the quality of the grown wafer layer structure and have minimal effect on the overall device characteristics.

For this work, the AIAs Layer #8 was split into 3 layers with the GaAs growth planarization layers positioned at nulls of the 0-order standing wave. This process required iterative RCWA analysis to obtain proper placement of the GaAs spacer layers for the widest possible range of GMR-SEL operating wavelengths. The results of this analysis yielded the design of Wafer #2 given in Table 3.5 corresponding to the response shown in Fig. 3.11.

Fig. 3.11 shows the RCWA field plots for Wafer #2 with GaAs growth planarization layers included to split the thick AIAs substrate spacer layer used for GMR-SEL Wafer #1. This figure shows that each GaAs spacer layer is placed at nulls of the 0-order standing wave pattern so that any coupling into these layers is minimized. This

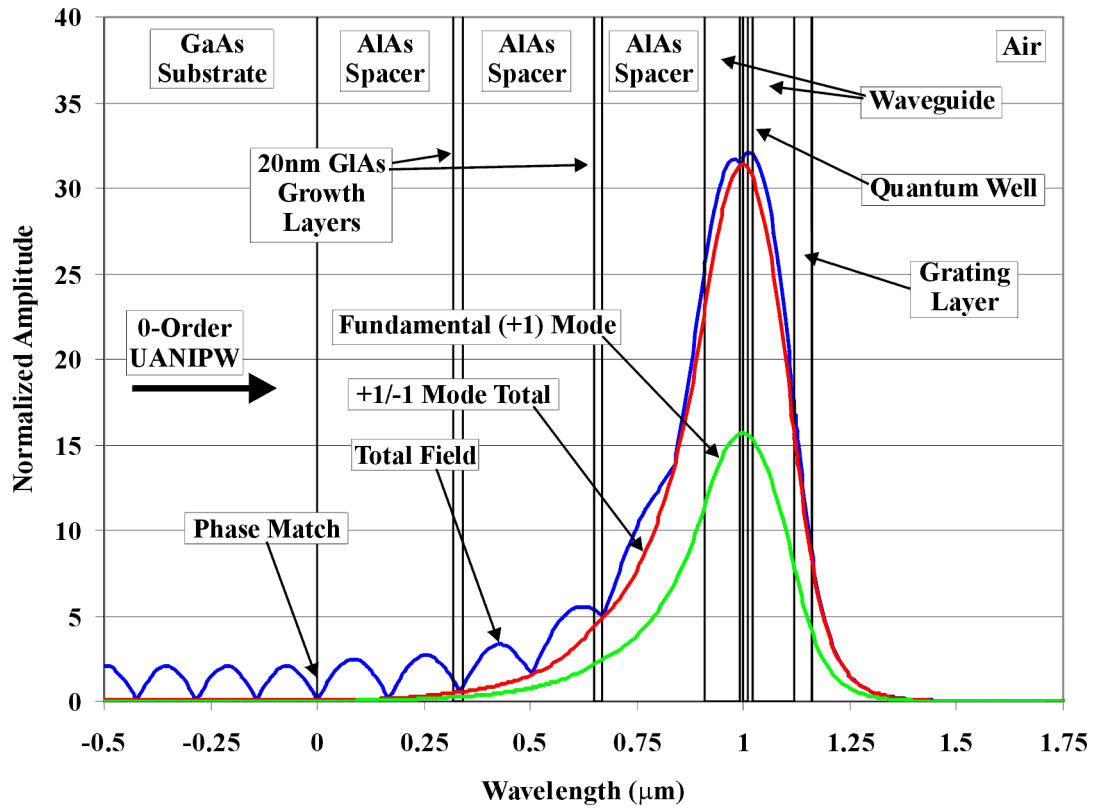


Figure 3.11. Simulated plot of electric fields as a function of position in the GMR-SEL layer structure for Wafer #2 described in Table 3.5. For this structure, the thick AlAs layer has been separated by two thin GaAs growth planarization layers. Simulation parameters are: Grating Period $\Lambda = 314$ nm, Grating Depth $d_1 = 40$ nm, Fill Factor = 0.5, and Resonant Wavelength $\lambda_{\text{res}} = 993$ nm.

layer structure was MBE-grown and evaluated by spectroscopic ellipsometry as with Wafer #1. Table 3.5 gives both the design and measured layer parameters.

The results shown in Table 3.5 show that the as-grown wafer structure is an excellent match to the design values. The fitted aluminum content and measured refractive index values vary slightly from the nominal design values, but this can be compensated through minor changes to the fabricated grating parameters. The next step

Table 3.5. GMR-SEL Wafer #2 Design and Measured Layer Parameters

Layer #	Material	Nominal Refractive Index	Design Thickness (nm)	Fitted Thickness (nm)	Fitted Refractive Index	Comment
12	GaAs-Oxide	--	--	1.3506±0.0379	--	
11	GaAs	3.515	20	19.805±0.271	3.516	
10	Al _{0.2} Ga _{0.8} As	3.397	140	126.13±0.95	3.402	Fitted Aluminum: x = 0.149±0.003
9	GaAs	3.515	10	8.9026±2.1	3.516	
8	In _{0.2} Ga _{0.8} As	3.600	8	10.554±1.67		Strained n, x not fitted
7	GaAs	3.515	10	9.7959±4.3	3.516	
6	Al _{0.2} Ga _{0.8} As	3.397	80	73.38±1.81	3.405	Fitted Aluminum: x = 0.145±0.003
5	AlAs	2.966	250	247.11±0.155	2.951	
4	GaAs	3.515	20	19.764±0.146	3.516	
3	AlAs	2.966	310	307.46±0.214	2.951	
2	GaAs	3.515	20	19.402±0.152	3.516	
1	AlAs	2.966	320	320.1±0.199	2.951	
Substrate	GaAs	3.515	--	--		Assume S.I. substrate

Note: Refractive index values estimated at ~985 nm

in wafer characterization is evaluation of the active layer gain profile. The photoluminescence curve for Wafer #2 is given in Fig. 3.12.

In Fig. 3.12, the measured photoluminescence for the quantum-well indicates that the peak value occurs at 1000 nm which represents a 20 nm shift from the design value of 980 nm. To better match the GMR-SEL resonant wavelength with the peak gain wavelength, the grating period required adjustment to 320 nm from the 314 nm design value. The 320 nm grating period is the design value for the fabrication steps outlined in Chapter 5.

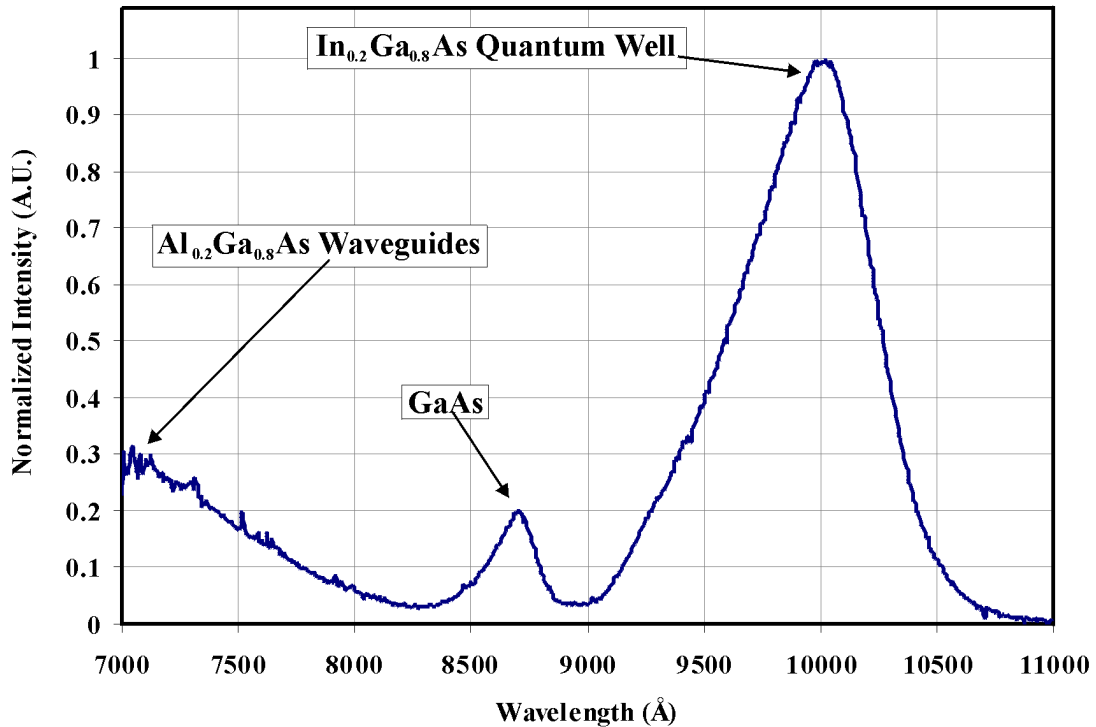


Figure 3.12. Plot of measured photoluminescence for GMR-SEL Wafer #2. The data indicates that the peak quantum-well photoluminescence occurs at 1000 nm. This represents an approximate 20 nm shift from the 980 nm design value. Data was obtained from approximately 14 W/cm² illumination at 488 nm.

3.8 Summary of GMR-SEL Design and Design Optimization

This chapter has outlined the design process for an optically-pumped guided-mode resonance surface-emitting laser (GMR-SEL). The design procedure includes initial design based on nominal material characteristics, design optimization through iterative RCWA and RCWA fields analysis, post-growth wafer layer characterization, and finally, refinement of the grating parameters for fabrication. The grating fabrication and device testing are outlined in the following chapters.

CHAPTER 4

HOLOGRAPHIC SUB-WAVELENGTH GRATING FABRICATION, ACTIVE FRINGE STABILIZATION, AND PHOTORESIST STACK DESIGN

A critical design step for fabrication of conventional dielectric as well as semiconductor GMR devices is the consistent and predictable patterning of sub-wavelength photoresist gratings. Sub-wavelength photoresist gratings planned for use in parts of this work are patterned using ultra-violet (UV) interference lithography on a wide variety of substrates and layer systems. The photoresist grating profile should have good removal (clearing) of the photoresist at the bottom of the grating grooves as well as smooth sidewalls. Additionally, the operating characteristics such as resonant wavelength, linewidth, and efficiency of diffractive waveguide-grating structures including GMR devices are very sensitive to the final grating fill factor, etch depth, and smoothness of the grating profile. Variations in the photoresist grating fill factor as well as any irregularities in the photoresist grating profile are ultimately transferred to the underlying substrate during the etching process. These irregularities result in defects that cause scattering losses during device operation resulting in reduced device efficiency and increased resonant linewidth [52].

To provide consistent patterning of high-quality photoresist gratings, each step of the lithographic process must be characterized and controlled. This characterization includes tailoring the photoresist layer thickness to optimize the lithographic exposure

process for the given material system and specific substrate layer reflectivity. This chapter describes the major considerations and techniques employed to fabricate photoresist gratings for GMR devices on both conventional dielectric substrates as well as semiconductor substrates. The lithographic interferometer design, implementation of an active fringe stabilization system, and design of the photoresist masking layers with resulting grating structures are presented.

4.1 Holographic Interferometer Performance Characteristics

The exposure system initially used for this research was the Lloyd's mirror interferometer [1, 10, 52] using an ultraviolet (UV) argon laser. This interferometer design was employed because of simplicity and rapid reconfigurability for producing different grating periods. Fig. 4.1 shows a schematic example of the Lloyd's mirror interferometer. The laser output is focused through a spatial filter / pinhole assembly to expand the beam as well as to provide a near-uniform beam intensity near the substrate plane. Fig. 4.1 shows that the beam emitted from the aperture of the spatial filter diverges with a spherical wavefront. Since the substrate is typically positioned far away

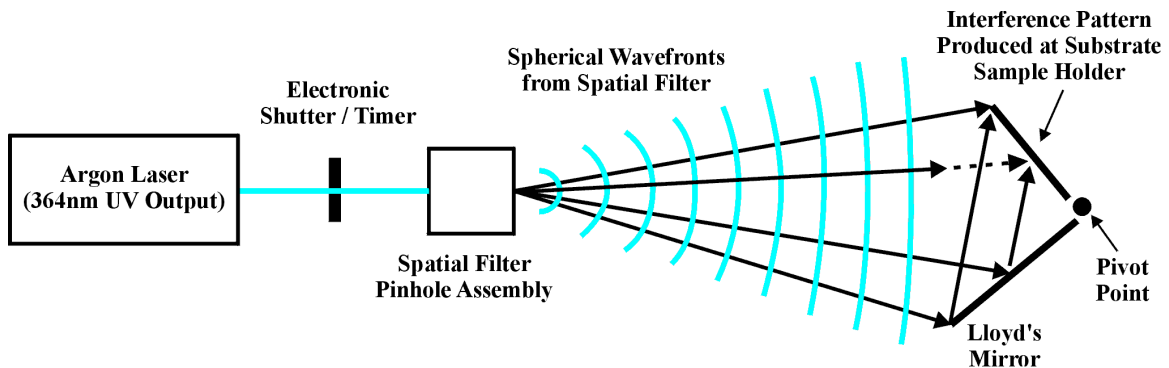


Figure 4.1. Schematic of Lloyd's mirror interferometer for exposure of sub-micron photoresist gratings.

(approximately 150 cm from the spatial filter in this work) the wavefront-phase curvature of the interfering beams is negligible and the interfering beams can be approximated by plane waves.

Typical substrate sizes exposed with this interferometer setup are between one and two inches in diameter. For a two-inch substrate, the wavefront-phase curvature of the exposing beams across the substrate area is calculated to be approximately 250 μm which is much less than the coherence length of the laser (greater than two meters for the laser used in this research) and can therefore be neglected [52]. Additionally, the curvature of the interfering wavefronts results in variation of the grating period (chirp); but over the relatively small substrate area, this effect can also be neglected in practice. As an example, when the interferometer is setup for exposure of 500 nm grating periods on two-inch substrates, the grating chirp is approximately 0.03 nm confirming that the incident plane wave assumption is reasonable [52]. Achieving a spatial intensity balance between the two interfering beams at the substrate exposure plane is of greater importance to consistently produce high-quality photoresist gratings.

Two difficulties in using the Lloyd's mirror single-beam interferometer are in achieving a uniform spatial intensity across the substrate and in achieving intensity balance between each of the two interfering beams. The beam intensity emitted from the spatial filter follows a Gaussian intensity profile with the peak centered on the beam axis. The substrate and Lloyd's mirror are then placed to each side of the peak intensity of the expanded beam profile as shown in Fig. 4.2. This figure is exaggerated to show the difference in intensity between the portions of the expanded beam used to form the

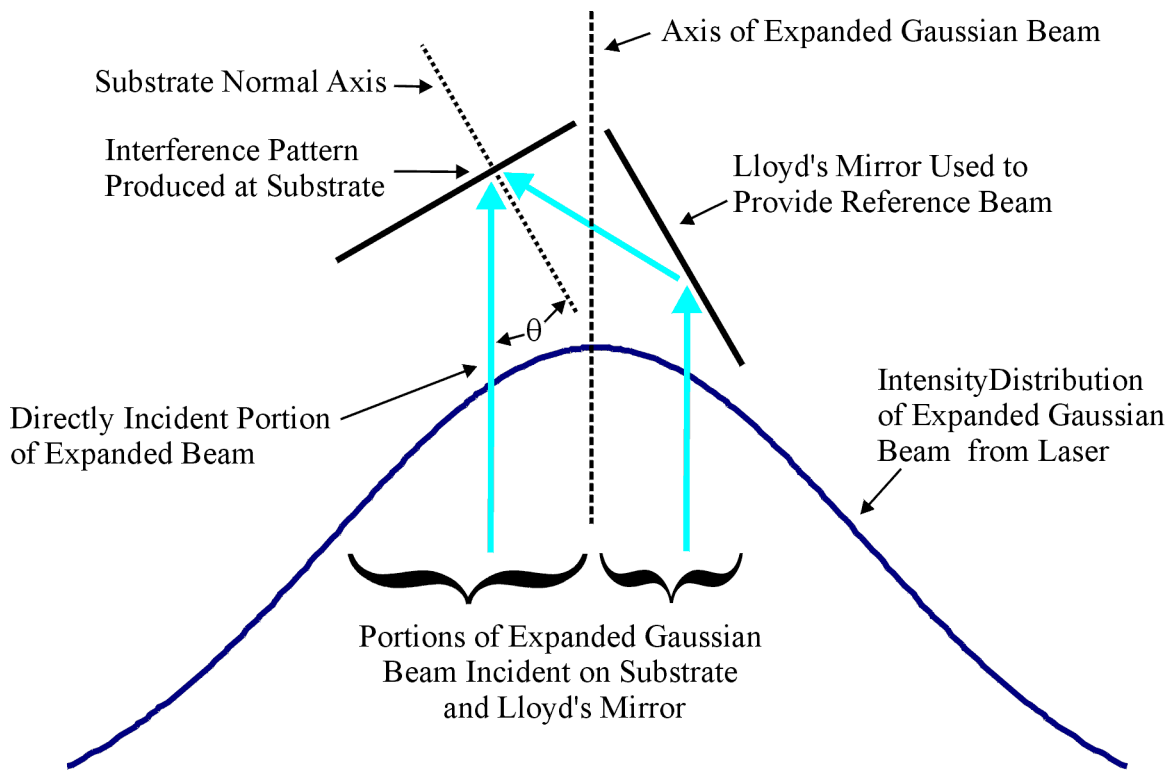


Figure 4.2. Schematic of intensity distributions for respective portions of expanded Gaussian beam incident on substrate and Lloyd's mirror.

interference pattern at the substrate. In practice, the intensity varies in a near-linear fashion across both the substrate and mirror although not at the same rate. As shown in Fig. 4.2, this is due to the difference in intensity across the cross-sectional area of the expanded beam incident on the substrate, and the smaller change in intensity for the portion of the expanded beam incident on the mirror.

The intensity distribution of the reference beam is more uniform since it is obtained from a narrower cross section of the expanded Gaussian beam. The substrate is positioned normal to the bisector of the interference angle θ required to produce the desired grating period Λ as shown in (4.1) and shown as θ in Fig. 4.2. The effects of

$$\theta = \sin^{-1}\left(\frac{\lambda}{2 \cdot \Lambda}\right) \quad (4.1)$$

non-uniformity in the beam intensity balance become most pronounced when there is a large difference between angles of incidence on the substrate and Lloyd's mirror. The angle between the substrate and the Lloyd's mirror is always fixed at 90 degrees for this style of interferometer. This insures that the incident and reference beams symmetrically illuminate the substrate at the same half-angle relative to the substrate normal.

Variation in the intensity between the incident and reference beams results in variation of the exposing irradiance across the substrate. (4.2) gives the total irradiance

$$I_{total} = I_{inc} + I_{ref} + 2\sqrt{I_{inc}I_{ref}} \cos \delta \quad (4.2)$$

of the interference pattern where δ is the phase difference between the incident and reference beams. An example plot of the variation in total normalized irradiance due to linear variation in the individual interfering beams is given in Fig. 4.3. In this figure, it is assumed that the incident beam intensity decreases linearly by 20% from unity over the substrate area while the second (reference) beam decreases by approximately 10% over the same area. (Variations of 10% are commonly measured in practice during experimental setup and alignment of the Lloyd's mirror interferometer for exposing photoresist gratings. All practical effort should be spent to minimize these intensity variations.) This figure shows only seven fringes projected over the substrate area. In practice, there are a few thousand fringes projected over the substrate area. The variation of irradiance is independent of the number of fringes.

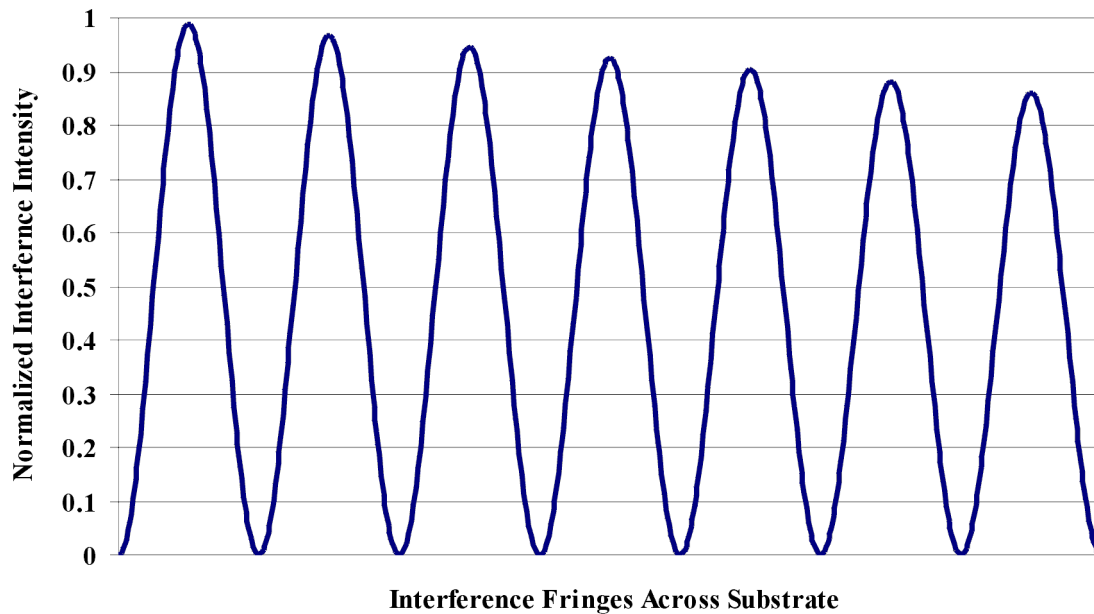


Figure 4.3. Stylized irradiance profile in substrate exposure plane with 20% and 10% variations in intensity of the respective incident and reference beams. Note that the number of interference fringes across the substrate is not to scale. The peak amplitudes of the fringes are independent of the number of fringes. The normalized interference intensity profile shows that there is an approximate 15% difference in exposure dose across the substrate.

Fig. 4.3 shows that the normalized interference intensity varies from unity at one edge to approximately 85% at the opposite edge of the substrate. The non-uniformity of exposure dose typically results in large differences in photoresist grating fill factor as well as variation in the overall grating profiles from one edge of the substrate to the other. This non-uniformity is typically manifested as over-exposure of the gratings on one edge while areas near the other edge of the substrate are under-exposed. One disadvantage in the Lloyd's mirror interferometer lies in the practical setup of the system. To compensate for any measured intensity differences in the exposing beams, it is necessary to physically

translate either or both the substrate holder and the Lloyd's mirror to obtain a useable beam balance. This translation becomes difficult in that all angles and alignment as well as the incident and reference beam intensity profiles must be measured for each change in the setup.

The Lloyd's mirror interferometer setup was used successfully in the initial parts of this work, but the reproducibility of results were observed to be inconsistent – especially for large-area gratings (several cm^2). Numerous interferometer configurations were evaluated in an effort to consistently produce high-quality photoresist grating structures. In all cases, it was found that the lithography setup was subjected to environmental disturbances present in the laboratory.

4.2 Interference Fringe Stabilization

Fabrication of devices with large-area diffraction gratings employing sub-wavelength periods begins by recording high-quality photoresist gratings. Non-linear photoresist exposure characteristics allow only narrow latitude for exposure dosages that produce optimum photoresist grating profiles with predictable fill factors. Thermal fluctuations, air currents, and vibration are environmental sources of fringe instability during holographic exposure. Numerous passive methods are available to improve the holographic environment, but often, active fringe stabilization becomes necessary to obtain consistent photoresist exposure [53].

Although single-beam lithographic interferometer setups such as the Lloyd's mirror interferometer of Fig. 4.1 can be quickly reconfigured to produce different grating periods, they are not easily stabilized to compensate for localized disturbances that cause

fringe movement during the exposure. One primary advantage of the two-beam interferometer configuration is that it is easily configured to incorporate active fringe stabilization. Additionally, in contrast to the non-uniform beam intensity often present for single-beam configurations, the two-beam interferometer typically exhibits excellent uniformity over the exposure area.

The uniform exposure area for a two-beam setup is approximately double that for the single beam, but the splitting of the available exposure energy typically dictates longer exposure times over that of the single-beam lithography system. For both types of interferometer, exposure times are also greatly increased when recording short grating periods approaching 200 nm due to the high angles of incidence at the substrate. These longer exposure times further necessitate active fringe stabilization to reduce blurring and loss of contrast during exposure.

4.3 Fringe Stabilization Methods

Traditional fringe stabilization methods include locking to discrete analog photodiode signals [54-56], mixing of substrate reflection beams [57], and digital heterodyne beam modulation [58, 59]. The simplest of these methods described in [54-56] utilizes two photodiodes placed alternately in one peak and one null of a projected interference pattern. The method of [57] utilizes self-induced diffraction by the photoresist during holographic exposure to perturb the phase of one of the beams reflected from the substrate. The negative feedback control system then maintains this same phase throughout the exposure. The method described in [58, 59] utilizes scanning-beam interference lithography (SBIL) to generate periodic fringes onto a moving

substrate. The methods of [57-59] each require additional optical and mechanical components and sophisticated control equipment such as lock-in amplifiers, and multiple acousto-optic modulators.

Video-based fringe stabilization systems have been implemented as fringe detectors for use in metrology applications such as fringe shift interferometry and electronic speckle pattern interferometry (ESPI) [53, 54, 60] for measurement of surface deformations. These methods utilize 2-D image data for comparison against stored reference image data. The fringe pattern is purposely shifted in several steps over a full fringe period and then compared to the reference images to determine the phase error in the fringe pattern due to environmental effects. The image processing required for multiple images typically limits the stabilization frequency to a few Hertz without additional dedicated image processing hardware. Applications in ESPI and fringe-shift interferometry are typically performed with visible wavelength lasers allowing simplified setup and alignment of the fringe detection system.

A primary complexity in setup of the UV lithographic interferometer for exposure of photoresist grating patterns is detection of the stabilization fringe pattern. The proper fringe spacing for stabilizing a UV interferometer is difficult to detect when the beam intensities are weak and the interference pattern from near-parallel beams cannot be visually observed. Properly aligning two discrete photodetectors significantly increases the time necessary to reconfigure a UV lithographic interferometer. The use of a charge-coupled device (CCD) camera-based system allows simplified interferometer setup as well as provides the fringe detector for the active feedback system.

4.4 CCD Camera-Based Fringe Stabilization Method

In this work, initial experimental setup and alignment is enabled by use of a CCD camera. The CCD element directly detects the projected fringe pattern and is employed for active feedback and stabilization. The projected UV fringes are generally weak or invisible, making proper placement of discrete photodetectors in the fringe field difficult to achieve. In contrast, system reconfiguration with the CCD method is straightforward.

Fig. 4.4 shows the basic two-beam UV grating exposure system employed in most of this research. In this configuration, the feedback system functions as a fringe stabilization system (rather than as a fringe-shifting interferometer described in [54]) with PC-based hardware and software that allows data acquisition and processing at the camera frame rate. As with the single-beam Lloyd's mirror interferometer described in

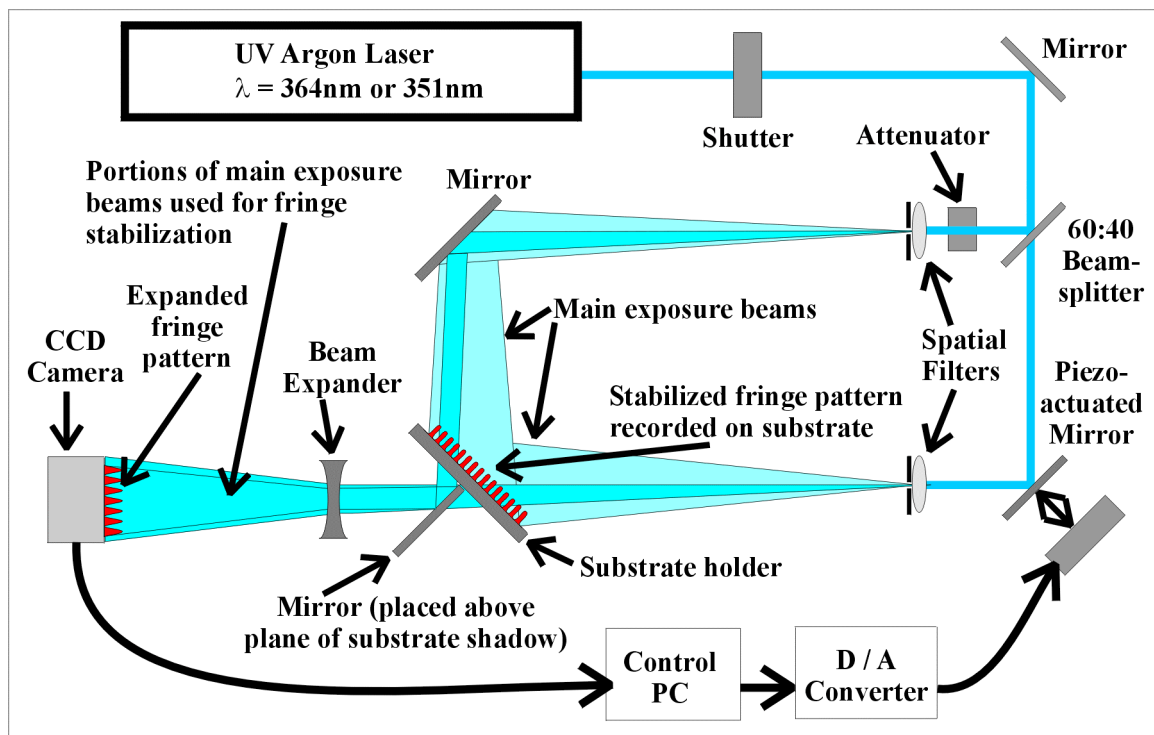
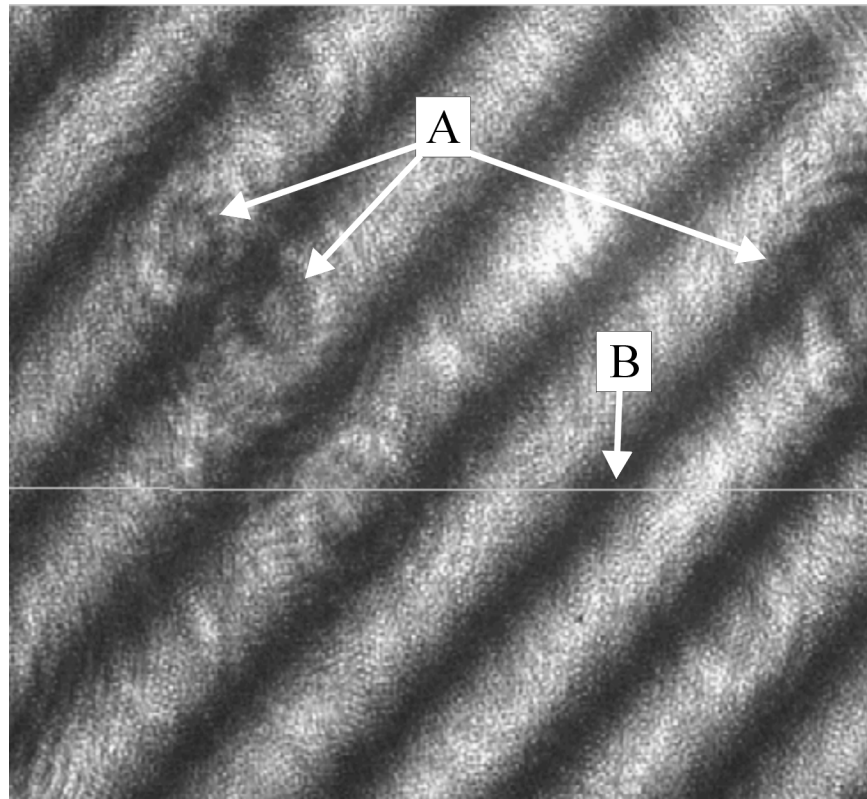


Figure 4.4. Schematic layout of interferometer and fringe control system.

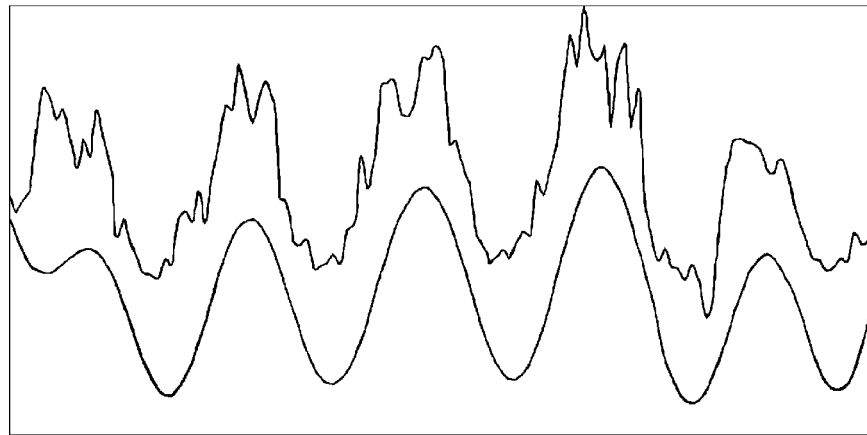
the previous sections, collimating optics are not used after the spatial filters, thus the beams are highly expanded to provide near-uniform illumination over the substrate area. With this configuration, the intensity peaks of the incident and reference beams (collinear with the beam axis) are simply aligned to the center of the substrate.

The system is easily reconfigured to produce different grating periods by moving the single mirror, similar to the single-beam setup. An attenuator (Glan-Thompson polarizer) is used before one or both spatial filters to provide intensity balance between the two interfering beams. This method to obtain acceptable beam intensity balance as well as beam uniformity at the substrate exposure plane is far simpler than the single-beam setup of Fig. 4.1. The beam sampling mirror(s) near the substrate allow the CCD camera to be positioned at any convenient location in the setup. A PC-based frame grabber card processes the CCD video data while an inexpensive 14-bit D/A converter drives the piezo-actuated mirror. The CCD camera used for this research had a 640 x 480 pixel array with each pixel providing 8-bit intensity resolution.

In typical configuration, 3-5 fringes are projected across the CCD detector element using a beam expander. Speckle noise from the beam expander optics and CCD shot noise have high spatial frequencies compared to the fundamental frequency of the interference fringes. Fig. 4.5(a) shows a typical full frame of the CCD video data. The points shown by Marker A indicate typical spatial noise artifacts introduced by imperfect optics. These spatial noise patterns remain spatially fixed for any given setup. A single line of the CCD video frame data is extracted at any convenient location within the full



(a)



(b)

Figure 4.5. Video frame and spatial intensity data. (a) Full frame of acquired interference pattern acquired from CCD camera with Marker A showing typical spatial noise patterns. (b) Unfiltered (top curve - omitting highest-order spatial harmonic) and filtered (bottom curve) intensity data reconstructed from single line of data indicated in the full frame by Marker B.

frame data to determine the relative position of the fundamental interference fringe pattern. Marker B in Fig. 4.5(b) indicates this single line of video data.

The PC-based frame grabber card and hardware driver performs direct memory access (DMA) to the PC memory at the completion of each acquired frame of video data. This frame data is then simply copied to a free memory location during each subsequent frame acquisition. A Discrete Fourier Transform (DFT) is performed on the 8-bit intensity data allowing decomposition into spatial harmonics. The DFT for N data points is defined by (4.3):

$$H_n \equiv \sum_{k=0}^{N-1} h_k e^{2\pi i k n / N} \quad (4.3)$$

where the complex data points H_n are obtained by using the summation of the h_k complex coefficients to approximate the integral of the forward Fourier transform equation [60]. By performing an inverse DFT (IDFT) while retaining only the low spatial frequency components associated with the fundamental fringe pattern, a smooth waveform with discrete peaks and minima is obtained. The IDFT is based on the coefficients of the DFT as shown in (4.4).

$$h_k \equiv \frac{1}{N} \sum_{n=0}^{N-1} H_n e^{-2\pi i k n / N} \quad (4.4)$$

Implementation of these equations as well as an efficient algorithm for performing calculation of the complex coefficients is given in [61]. One key point to the DFT / IDFT algorithm given in [61] is that the number of data points N should be an integer power of 2. This requires padding the array of 640 pixel intensity values from the line of acquired data with zeros to form an array of 1024 data points. The DFT operation

provides spatial harmonics of the video intensity data over the video frame width, i.e. $1/1\text{Frame}$, $1/2\text{ Frame}$, ... $1/2^N\text{ Frame}$. Filtering of the high-order spatial harmonics is simply performed by applying a square window function (multiplying the unwanted high-order complex coefficients, H_N , by zero, and multiplying all retained low-order coefficients by 1) before performing the IDFT function.

Figure 4.5(b) shows the reconstructed reference frame data with two levels of filtering. The two curves are offset for clarity. The unfiltered reference data retains 256 spatial harmonics (highest order harmonic omitted) while the filtered fringe pattern is reconstructed from the lowest 35 spatial harmonics of the video frame width. On the start of phase correction during exposure, an initial pattern of filtered data is established as the zero-phase reference for the remainder of the exposure. Subsequent frames are processed in a similar manner, revealing lateral shifts in the fundamental fringe pattern irrespective of any noise superimposed on the acquired intensity waveform. The software then simply tracks the minima and maxima of the most recently acquired waveform relative to the reference, and issues an error signal through the D/A converter to correct the fringe shift.

The stabilization system is controlled through the software interface shown in Fig. 4.6. The software is implemented in Visual C++ using ActiveX controls. The software interface allows configuration of the camera and image settings, image filtering, initialization, and statistical output. A separate threaded software application monitors the frame grabber hardware drivers and transfers image frame data into shared computer memory. The software then issues an error signal through a serial port to the D/A

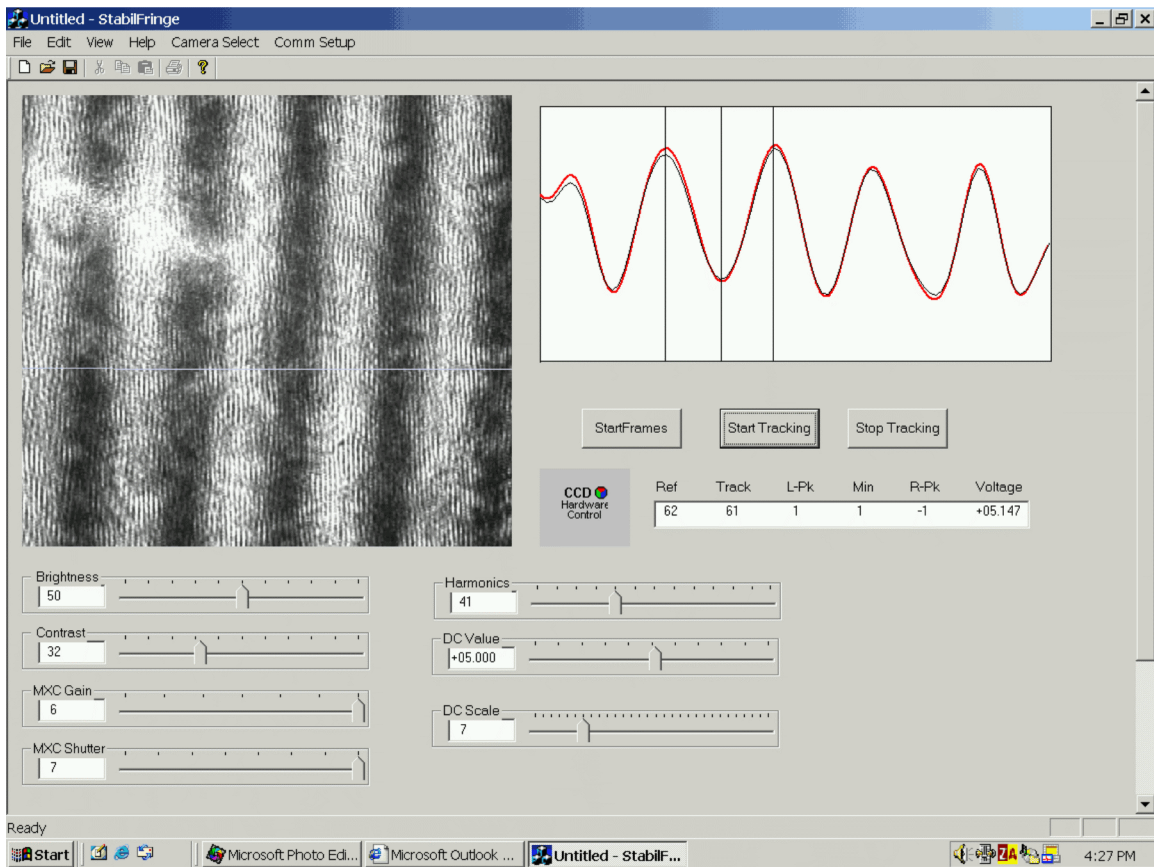


Figure 4.6. Snapshot of main software user interface.

converter to correct the fringe shift. The gain of the error signal can be set as needed in the software graphical interface shown in Fig. 4.6. For this application, the piezo-element is typically driven between 0 and 10 volts by the D/A converter. This control voltage range provides a maximum shift of approximately 4 fringes at the 364 nm exposure wavelength. The small control voltage range allows hysteresis of the piezo-element to be neglected.

Since the IDFT places the filtered intensity data in bins (memory locations) indexed according to the original reference frame pixel data, the fringe minima and

maxima are followed within an accuracy better than one pixel. For five fringes projected across a 640 pixel element CCD detector, one pixel corresponds to $\sim 1/100$ fringe. For ~ 2.5 projected fringes, the detection and correction accuracy is $\sim 1/200$ fringe. This accuracy is a significant improvement over conventional photodiode-based fringe stabilization systems, especially in the presence of laser intensity noise. Laser intensity noise affects the amplitude of the peaks and minima of the fringe pattern, but not the actual spatial position of the fringes. The fringe stabilization system described in this work operates only on the relative fringe positions independent of the actual fringe amplitude. In two-photodiode detector systems, laser intensity variations are measured as changes in differential intensity and are indistinguishable from lateral fringe shifts.

4.5 Fringe Stabilizer Performance Results

Figure 4.7 shows an example of a typical uncorrected (total accumulated fringe shift from initial reference) and the corresponding corrected fringe shift during a 150-second exposure. The results show that the uncorrected fringe pattern of Fig. 4.7(a) would drift over a full fringe (360°) causing degradation or loss of definition of the recorded pattern. Fig. 4.7(b) shows the actual measured fringe shift during the same time period. The results indicate that the stabilized fringe shift is typically less than two degrees with maximum deviations less than four degrees over the duration of the exposure. Statistics for the 150 second exposure are: mean = 0.12° , standard deviation = 1.50° (before initial lock), maximum deviation = 3.0° . The standard deviation is reduced to 1.34° after initial lock.

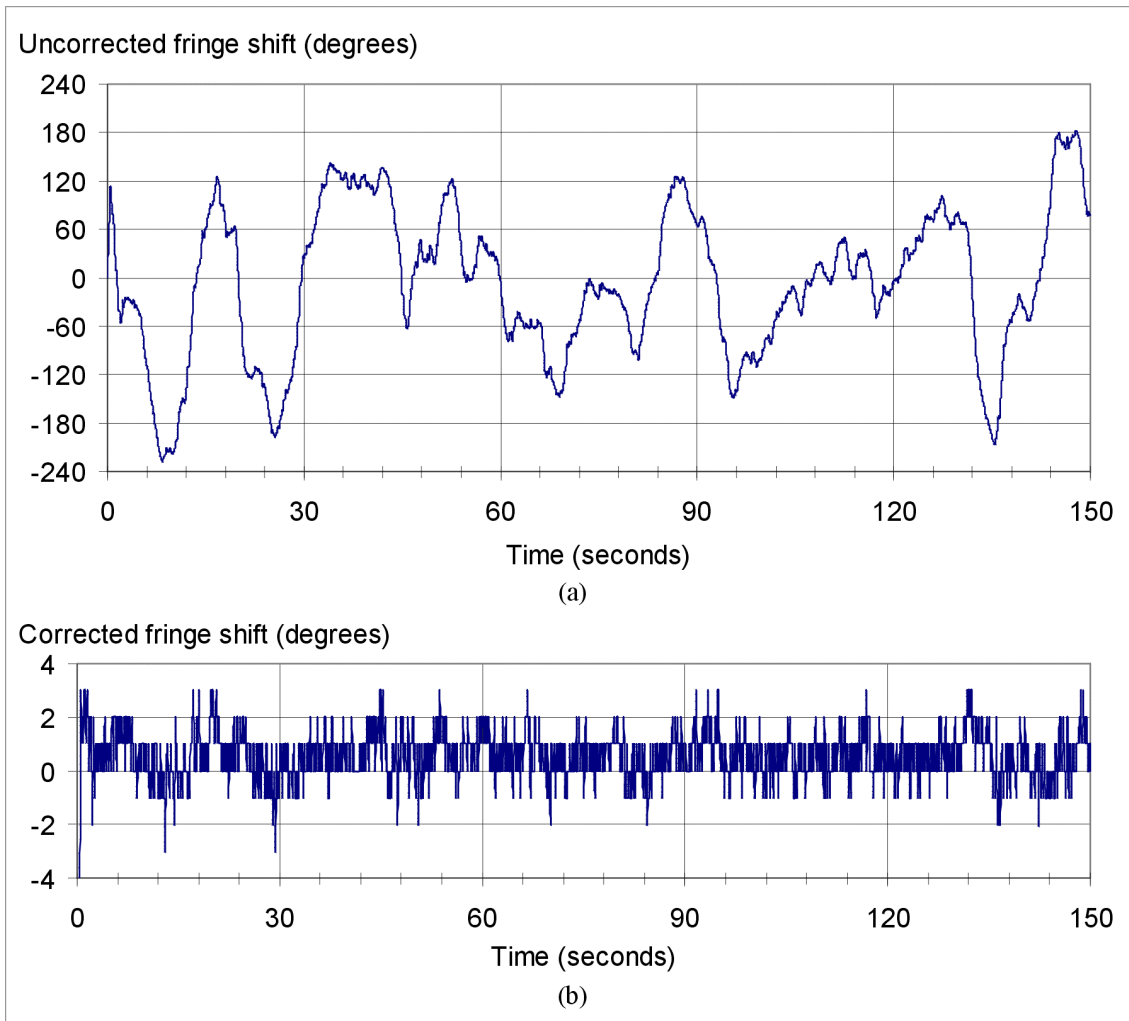


Figure 4.7. Measured uncorrected (a) and corrected (b) fringe shift in degrees versus time for a 150 second exposure. One fringe period corresponds to 360° .

Figure 4.7(b) also shows that the corrected fringe shift maxima ($>\pm 2$ degrees) occur when the uncorrected fringes of Fig. 4.7(a) are shifting most rapidly. The camera sample rate of 25 Hz is fast enough in this example that feedback positioning of the piezo-element can be performed by direct control rather than the proportional-integral-differential (PID) method implemented in [60]. PID control has proven unnecessary to accurately stabilize the UV lithography system in the current environment, but could be

easily implemented in software if necessary. A camera with an increased frame rate would further eliminate the need for a more sophisticated control algorithm such as the PID method.

The excellent fringe stability provided by the CCD camera-based system has allowed consistent fabrication of sharp photoresist grating features with periodicity near 200 nm (100 nm line features) over a 20 cm² area. Fig. 4.8 shows typical photoresist grating structures that have been fabricated with the UV lithography system described. Fig. 4.8 also illustrates the sensitivity of the grating fill factor to the photoresist exposure dosage. The exposure of Fig. 4.8(b) is approximately 10% greater than that of Fig. 4.8(a), showing that the grating fill factor decreases from ~60% to less than 50%. The CCD camera-based fringe stabilization system allows consistent reproduction of these results.

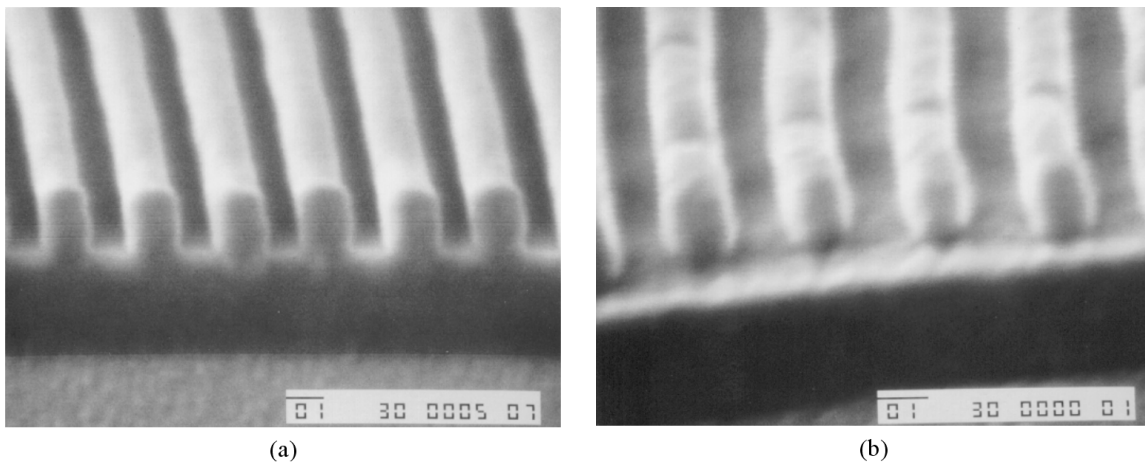


Figure 4.8. SEM photographs of 250 nm photoresist grating structures with variable exposure energy: (a) $E = 71 \text{ mJ/cm}^2$ in 170 seconds. (b) $E = 77 \text{ mJ/cm}^2$ in 190 seconds. The scale bar in each figure is 100 nm. Curvature of the grating fringes is an artifact of SEM sample preparation and imaging.

4.6 CCD-based Fringe Stabilization Summary

After frequency domain removal of the high spatial frequency intensity noise components, the fringe stabilization system provides immunity to noise sources such as shot noise, speckle noise, and variations in laser output intensity. The CCD camera-based active fringe stabilization system provides fringe control better than $\pm 1/100$ fringe using inexpensive off-the-shelf components. The UV lithography system can be rapidly reconfigured to produce different photoresist grating periods with minimum realignment of the optical components. A single line of the frame data is used to determine the exposure fringe position in the experimental results presented. Performance is largely dominated by the CCD camera frame rate since all other processing occurs in less than 1mSec. A high-performance line-scan CCD element similar to those used in commercially available scanners and copier technology with an increased refresh rate would allow fringe correction to be performed at 500 Hz rates or higher with current PC-based hardware.

4.7 Design of photoresist stacks for optimum exposure characteristics

To produce high-quality photoresist grating profiles, it is necessary to optimize the photoresist layer thickness before lithographic exposure. The use of monochromatic coherent laser light during for photoresist exposure produces the desired periodic interference pattern in the substrate plane that defines the required grating structure as functions of wavelength and interference angle as given by (4.1). At the same time, an unwanted secondary interference pattern normal to the substrate is produced via the reflected beams that can significantly affect both the resulting photoresist grating profile

as well as the overall reproducibility of the photoresist grating exposure process. This secondary interference can produce vertical standing waves in the photoresist and cause complete degradation of the final photoresist profile, reduce the photoresist grating fill factor, and also lead to excessive exposure times. The secondary interference effect becomes most pronounced for substrates that exhibit high reflectivity at the exposure wavelength.

To control the photoresist exposure characteristics, it is necessary to model this secondary interference pattern standing wave pattern and design the photoresist stack layer thicknesses to minimize these deleterious effects [65]. This modeling work was originally developed for the photoresist gratings fabricated on the fused silica / dielectric waveguide GMR substrates described in Chapter 2 and [36] and was extended to the GaAs/Al_xGa_{1-x}As substrates used for the GMR-SEL device described in subsequent chapters.

4.8 Photoresist Grating Requirements and Exposure Characteristics

Most commercially available photoresists for use at exposure wavelengths near 364 nm (I-line) are designed for microelectronic fabrication with minimum feature sizes near 0.5 μm . For GMR devices operating at visible and near-infrared wavelengths, the required grating periods are in the range of approximately 200 nm to 600 nm having typical feature sizes between 100 nm and 300 nm. When fabricating sub-wavelength grating structures for GMR devices, the maximum feature sizes are typically equal to or smaller than the minimum resolution specified by the photoresist manufacturer. For sub-micron grating features, the grating aspect ratio (grating depth to line width) is often

limited to approximately 3 to 1 to avoid delamination or breakage of the photoresist grating lines. The photoresist typically requires dilution with a compatible thinner to reduce the layer thickness during spin application thus limiting the final grating aspect ratio.

The primary photoresist used in this work is Shipley Ultra-i123 positive photoresist diluted with the corresponding Shipley thinner. The developer used to remove the exposed areas of photoresist is Shipley Megaposit MC-26A. The Shipley Ultra-i123 positive photoresist used for this work is a high-resolution I-line (peak sensitivity near 364 nm wavelengths) commercial novolac-based photoresist [62, 63, 66]. (Novolac is the base resin used in modern high-resolution positive photoresists that promotes adhesion and reduces swelling during development [66].) Other novolac-based non-chemically amplified photoresists were previously evaluated, but are not reported as part of this work due to unsatisfactory results.

One primary characteristic for virtually all photoresists is the nonlinear exposure characteristic. Nonlinear photoresist exposure characteristics allow narrow latitude of exposure dosages that produce optimum photoresist grating profiles with predictable fill factors. This nonlinear characteristic is defined by an exposure threshold E_T above which, the exposed photoresist is completely removed (cleared) during the development process. Below the exposure threshold E_T , only some fraction of the resist is removed. E_I for which no material is removed during development defines a lower limit for exposure. These are stylistically represented in Fig. 4.9 [66]. The actual values for E_T and E_I are functions of the actual feature sizes, spacing, layer thickness, substrate

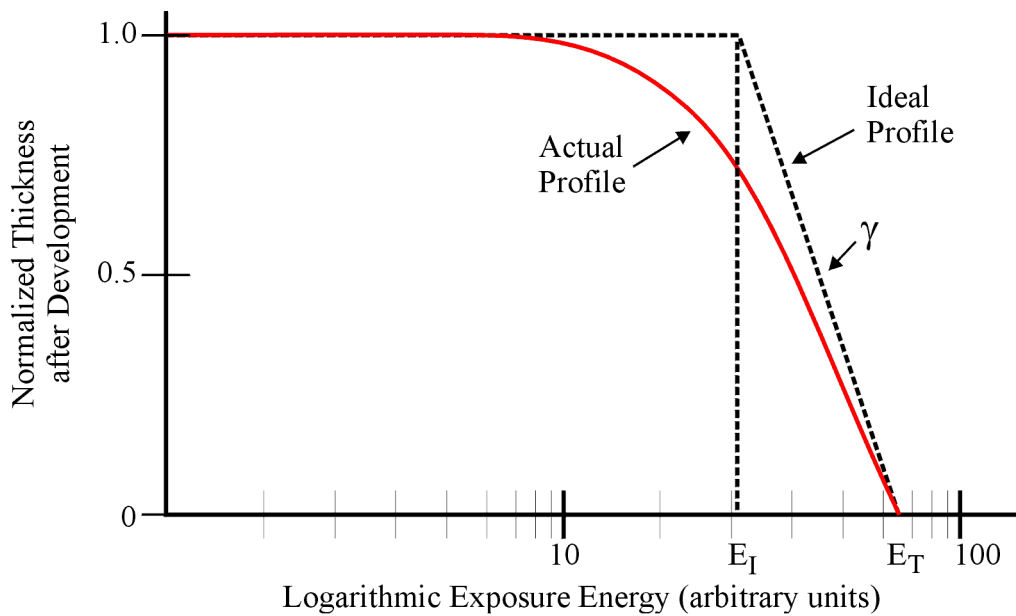


Figure 4.9. Stylized plot of normalized photoresist thickness remaining after development versus logarithmic exposure energy for a positive photoresist. The slope γ represents an ideal linear photoresist contrast ratio characteristic [Adapted from [66]].

reflectivity, as well as the soft bake and post exposure bake processes. The photoresist manufacturers typically only supply exposure values and processing parameters for large-area photoresist removal [63] that vary considerably in practice and thus must be empirically determined for the specific application such as the dense sub-micron lines and spaces patterned in this work.

These exposure threshold characteristics are also related to the photoresist contrast ratio. The photoresist contrast ratio is commonly expressed in the form of (4.5).

$$\gamma \equiv \frac{1}{\left[\ln \left(\frac{E_T}{E_I} \right) \right]} \quad (4.5)$$

The contrast ratio is simply a measure of the ideal tangential slope of the normalized thickness remaining after development versus exposure energy curve. A logarithmic profile is assumed for the curve between the actual upper and lower energy thresholds.

For interference lithography, the exposing interference pattern follows a squared sinusoid spatial energy distribution. This energy distribution in combination with the nonlinear photoresist exposure characteristic can be used to produce rectangular photoresist grating profiles with practical grating fill factors between approximately 0.3 and 0.6 [4, 36, 64]. For photoresist grating periods of 300 nm and below, the nonlinear exposure characteristic results in an upper limit on the grating fill factor of approximately 0.6 in practice.

Figures 4.10 and 4.11 show two sets of examples of the sensitivity of the grating clearing and profile to the exposure dose. In each figure, the photoresist gratings have 250 nm periods fabricated on GaAs substrates with a bottom anti-reflection coating (BARC) described below. Fig. 4.10a shows that for the given exposure, the grating fill

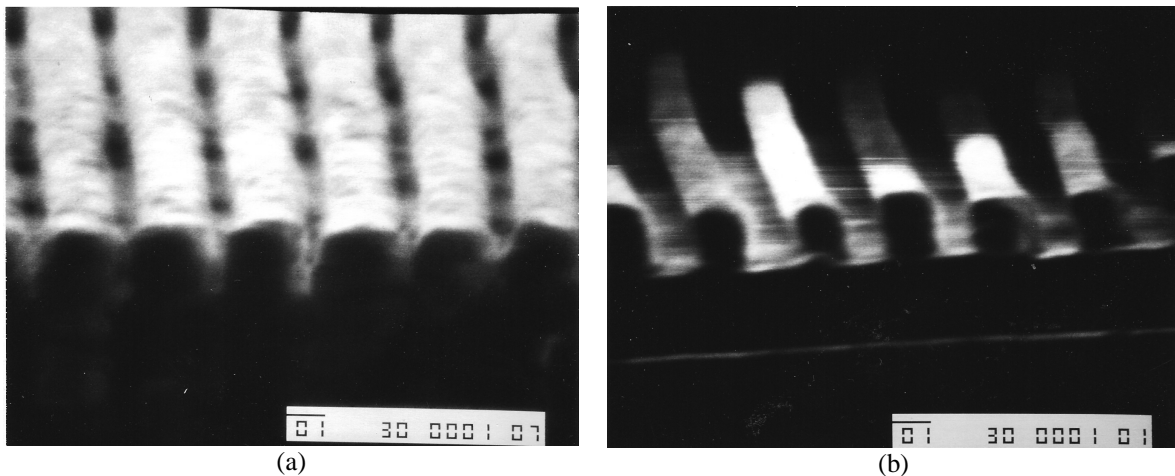


Figure 4.10. 250 nm photoresist grating structures with variable exposure energy: (a) $E = 62 \text{ mJ/cm}^2$ in 140 seconds. (b) $E = 65 \text{ mJ/cm}^2$ in 150 seconds. The scale bar in each figure is 100 nm.

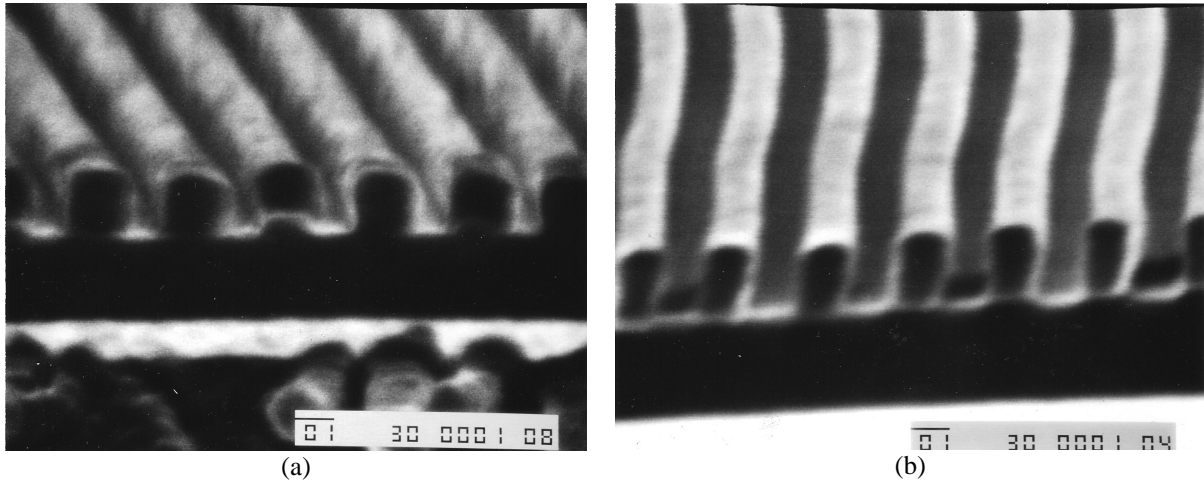


Figure 4.11. 250 nm photoresist grating structures with variable exposure energy and increased development time: (a) $E = 62 \text{ mJ/cm}^2$ in 140 seconds. (b) $E = 65 \text{ mJ/cm}^2$ in 150 seconds. The scale bar in each figure is 100 nm.

factor is approximately 75%, but there is incomplete clearing of the photoresist in the grating grooves. By increasing the exposure dose, from 62 mJ/cm^2 to 65 mJ/cm^2 (approximately 5%), good clearing occurs between the grating lines. For this small change in exposure dose, the grating fill factor decreases to approximately 0.6. The post-exposure bake was 60 seconds at 110°C with a 60-second development for both gratings. Fig. 4.11 shows a similar set of gratings processed with the same exposure and post-exposure bake parameters with the development time extended by 50% to 90 seconds. Fig. 4.11(a) shows that the grating has acceptable clearing between the grating lines, but also that the grating has an approximate 0.6 fill factor for the same exposure as in Fig. 4.10(a). Fig. 4.11(b) shows the corresponding photoresist grating with a 5% increase in exposure dose. The fill factor is now again reduced to approximately 0.6% showing that this is a practical upper limit on the photoresist grating fill factor with this fabrication method. In each case for Fig. 4.11, the grating profiles are smoother with good clearing in the grating grooves when

compared to those of Fig. 4.10. The difference between the gratings in Figures 4.10 and 4.11 indicate that the longer 90-second development is a preferable processing parameter. This 90-second value is twice the 45-second development time recommended by the photoresist manufacturer for dense lines and spaces [62].

Fig. 4.12(a) shows the practical lower limit for photoresist grating fill factors is approximately 0.3. This figure shows well-defined grating fringes approximately 100 nm wide with a 30% fill factor of the grating period. Fig. 4.12(b) shows a typical effect that occurs for smaller fill factors. The photoresist grating lines are too narrow to support themselves structurally and are easily broken during the photoresist development processing. In this figure, the grating lines are still attached to the substrate, but have broken and are leaning against the adjacent grating lines. These results clearly

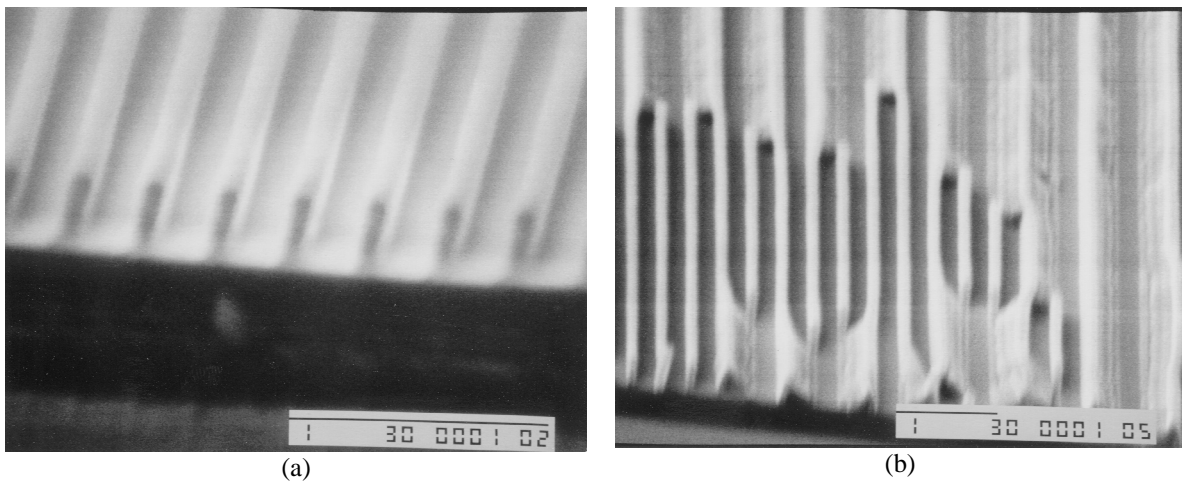


Figure 4.12. Example of a photoresist grating profile showing a minimum practical fill factor of approximately 0.3. (a) shows well defined lines for 30% fill factor. (b) When the photoresist grating fill factor is reduced below approximately 0.3, structural failure of the photoresist often occurs. In this figure, most of the grating fringes have fractured near the base, but have not detached from the substrate. The fractured photoresist grating fringes are leaning against the adjacent grating fringes. The scale bar in each figure is 1 μm.

indicate that the Shipley Ultra-I 123 photoresist can be reliably “pushed” to produce grating lines of approximately 100 nm which are less than half the 230 nm minimum feature sizes specified by the manufacturer [62].

Typically, the photoresist grating pattern is transferred into the substrate layers by reactive-ion-etching (RIE) with the RIE etch chemistry determined by the specific material system. In most RIE etching processes, there is significant removal of the photoresist mask as well as the substrate material. The specific RIE etch chemistry can be adjusted to provide preferential etching of the substrate material while minimizing removal of the photoresist mask material for a given etch chamber; but again, this requires extensive characterization of both the specific process and RIE etch tool. Often when even small changes are made in either the substrate design or photoresist processing, the RIE etch process requires re-characterization to obtain the desired etch profiles. An often beneficial improvement to the fabrication process is to employ a secondary etch mask such as a dielectric or metal layer to serve as a robust “hard mask” to mitigate the effects of photoresist mask degradation during RIE etching.

Two common methods of providing a hard mask for RIE processing are by direct inclusion of the mask layer into the substrate design, or by employing a lift-off method where the hard mask is provided after photoresist exposure and development processing. The direct method includes the secondary mask material as the top layer of the substrate design (below the photoresist layer) during the lithographic patterning steps. The lift-off method is typically accomplished by depositing a metal layer over the top of the

photoresist pattern followed by chemically removing (lifting-off) the metal-covered photoresist leaving a patterned metal mask on the top surface of the substrate.

In this work, the lithography on directly-deposited hard mask layers was investigated as a method for improved RIE etch processing as well as to reduce the unwanted effects of reflections from the back side of transparent substrates during grating exposure. These studies lead to the related work using the lift-off process in References [4, 36, 64]. In this work, the process included deposition of a thin metal layers (approximately 15 nm) of Chromium or Titanium on top of the basic GMR waveguide / substrate structure of Fig. 2.1 before deposition of the photoresist layers. The inclusion of this metal layer increased the reflectivity of the substrate which in turn required use of a bottom anti-reflection coating (BARC) below the photoresist layer to enable definition of the photoresist gratings. This same analysis method for design of photoresist layer stacks including the use of BARC coatings on high-reflectivity substrates was applied for the GaAs / AlGaAs substrates to be used in fabrication of the GRM-SEL device described in later chapters.

4.9 Photoresist stack design using a bottom anti-reflection (BARC) coating

The BARC coating used in this work was Brewer Science XHRIC-11 with refractive index values of $n = 1.86$ and $k = 0.37$. This coating is applied by substrate spinning followed by a 90 second hard bake at 175°C which removes the solvent and makes the BARC coating resistant to the photoresist solvent applied in the next step. Layer refractive index and thickness versus spin speed curves were determined empirically by measurement with a spectroscopic ellipsometer. These curves are given in

[36]. Inexpensive silicon wafers were used throughout this work as test substrates for measuring the thickness and refractive index of deposited layers, as well as for optimizing the intensity balance between the two interfering exposure beams and post-exposure processing.

Additional processing after exposure and development of the photoresist grating includes an oxygen plasma (ashing) etch step to transfer the photoresist grating lines into the BARC layer which opens a window exposing the thin metal layer in the base of the grating grooves. A wet chemical etch is then applied to the metal layer to expose the substrate and allow the grating groove profiles to be RIE etched into the waveguide-grating structure. After RIE processing, the metal and any remaining photoresist stack materials are removed in a final wet etch step. This work is focused primarily on the design and processing of the photoresist layer stack; results from the additional processing including RIE ashing and etching are not presented here.

Without proper design of the photoresist and BARC layers, photoresist gratings fabricated on high-reflectivity substrates often yield photoresist gratings profiles with grating fringe heights corresponding to the first interference peak of the standing wave normal to the substrate during exposure. The grating fringe heights fall in the range between approximately $1/4^{\text{th}}$ and $1/2$ of the exposing wavelength regardless of the original photoresist thickness. This effect is shown in Fig. 4.13 for a pair of exposures performed with single photoresist layer with the BARC layer omitted. The unexposed photoresist thickness was approximately 290 nm with resulting developed grating profile heights of approximately 70 nm corresponding to the first intensity peak near $\lambda/2$ from the substrate.

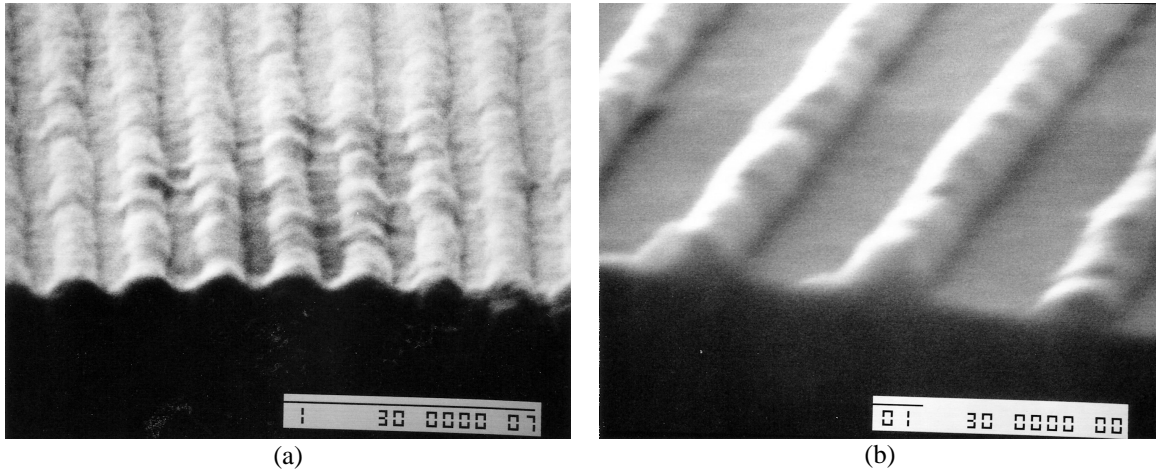


Figure 4.13. The SEM photos of 310 nm photoresist grating on a silicon wafer. (a) and (b) show the height of photoresist grating lines limited to approximately 70 nm corresponding to the first peak of the standing wave normal to the substrate during exposure. As with previous results, the increased exposure time for the grating of (b) results in a reduced grating fill factor and improved clearing in the grating grooves.

This effect is due to large-amplitude standing wave effects normal to the substrate produced by high substrate reflectivity. A commercial thin-film design software package was used to calculate these standing wave effects for various photoresist stack designs [67]. An illustration showing the calculated amplitude of this standing wave for a substrate without a BARC coating is given in Fig. 4.14.

Figure 4.14 shows a calculated intensity profile for an unoptimized photoresist stack on a silicon wafer. This figure shows the interference standing wave within a 280 nm ($5\lambda/4$) photoresist layer on a silicon substrate. A general rule for conventional photolithography as used in semiconductor manufacturing, the exposure is optimized when the photoresist layer thickness is an odd multiple of quarter wavelengths. For this thickness, the reflected energy is minimized, thus the exposure energy is maximized. In Fig. 4.14, the reflected standing wave peaks are approximately 1.5 times the incident

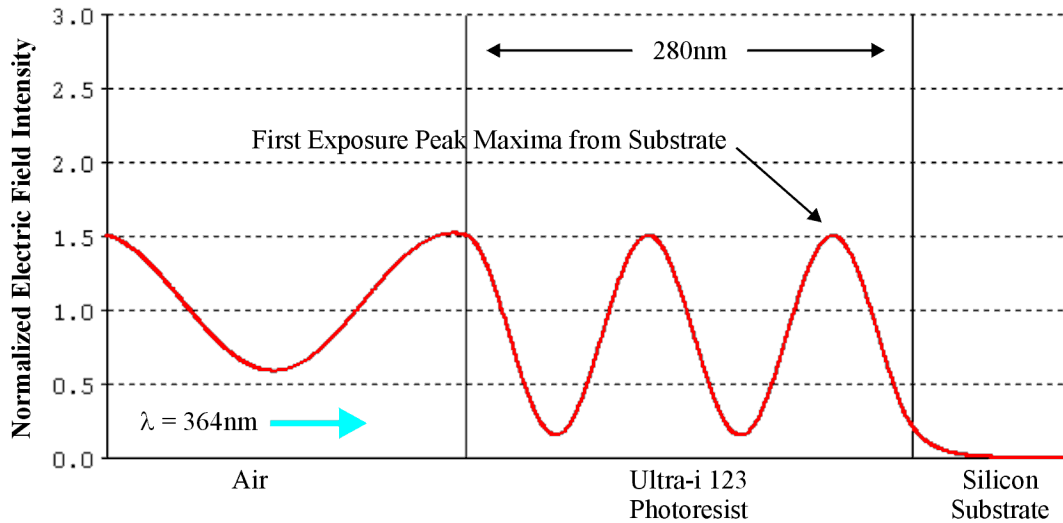


Figure 4.14. Calculated profile of normalized electric field intensity in the direction normal to the silicon substrate. The ratio of the peak to minimum intensity values of the standing wave in the photoresist is approximately 7. $\theta_{\text{half}} = 36^\circ$ corresponding to the incident angle to produce a 310 nm grating period.

intensity. Within the photoresist layer, the standing wave peak and minimum intensity values are 1.5 and 0.2 respectively giving an intensity standing wave ratio of 7.5. This large standing wave prevents uniform exposure within the grating grooves (for positive photoresist, the grating line is created by zero exposure within the null of the lateral standing wave). When the exposure dose is sufficient to expose the photoresist within the grating groove (to be removable by developing), the photoresist in regions near odd multiples of a quarter wavelength from the substrate become highly overexposed.

This large exposure dose “bleeds” into the adjacent grating fringe region and exposes this region also. Upon development, the exposed photoresist is dissolved effectively removing the tops of the grating fringes leaving only the unexposed photoresist attached to the substrate. The standing wave effectively limits the maximum height of the grating fringes to the height of the first standing wave peak above the

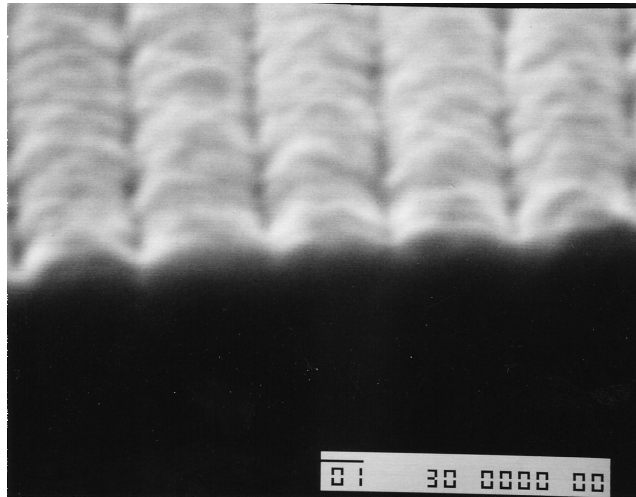
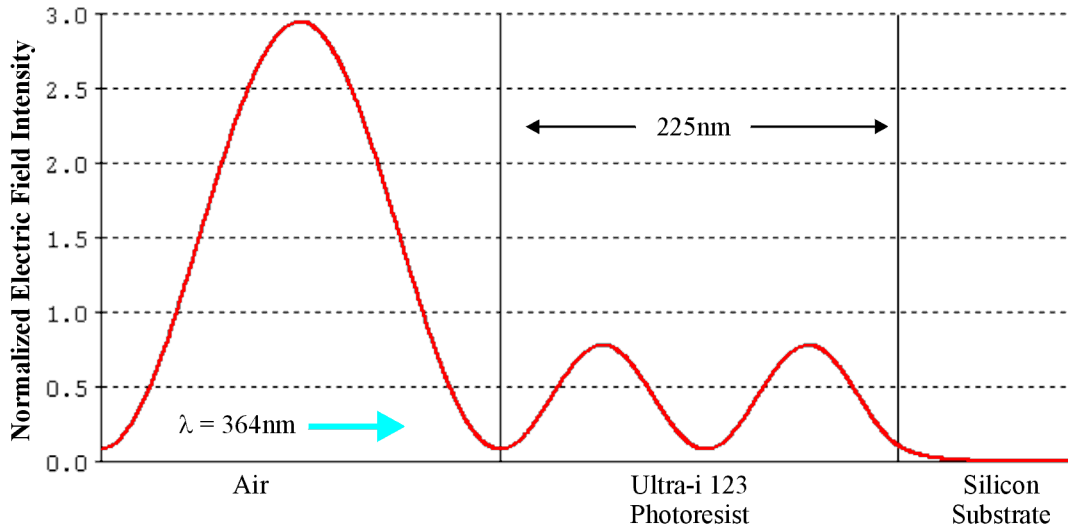


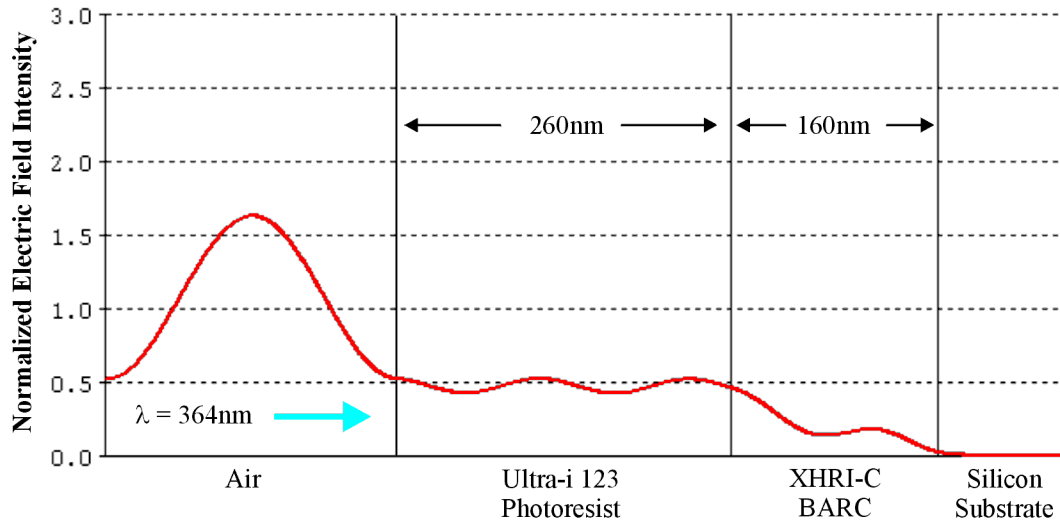
Figure 4.15. SEM photo of a photoresist grating on a silicon wafer exposed to threshold of clearing in the grating groove during development.

substrate. If the exposure dose is reduced, the grating grooves are not cleared during development as shown in Fig. 4.15. In this figure, the photoresist is exposed just to the threshold to begin clearing the grating groove at the top of the photoresist, but the photoresist is underexposed in the regions below the surface. For exposures without using a BARC layer, a small improvement in the photoresist exposure can be gained by changing the photoresist thickness to an even multiple of the quarter wavelengths as shown in Fig. 4.16(a). This profile shows that although the reflected intensity in air increases to approximately 2.9, the ratio of the standing wave intensity peaks to minimums within the photoresist layer is reduced to approximately 5. This standing wave ratio is still too large for exposure of high quality photoresist gratings with sub-micron periods.

Figure 4.16(b) shows the effect of including a BARC layer with optimized thickness below the photoresist. The BARC material has a higher refractive index than



(a)



(b)

Figure 4.16. Calculated profile of normalized electric field intensity in the direction normal to the substrate. (a) Intensity profile for a single photoresist layer with single wavelength thickness (even number of quarter wavelengths.) (b) Intensity profile for optimized photoresist stack including a BARC layer. $\theta_{\text{half}} = 36^\circ$ corresponding to the incident angle to produce a 310 nm grating period.

the photoresist and is absorptive at the exposing wavelength. This layer allows matching the amplitude and phase of the incoming exposure beam with the various amplitudes and phases reflected at the substrate, interlayer, and photoresist / air interfaces. The standing wave in the photoresist is largely eliminated. The inclusion of the BARC layer allows fabrication of photoresist gratings with near rectangular profiles shown in Fig. 4.8 and in [4, 36]. Under some conditions, when highly reflective layers are present in the substrate layers, an intermediate low refractive index layer may be required between the BARC and photoresist layers [65]. This allows improved amplitude and phase matching between the various layers including the photoresist-to-air and the BARC-to-photoresist interfaces. A deposited SiO_2 or TiO_2 layer is often used for this intermediate matching layer. As the photoresist stack design increases in complexity, the layer material properties and thicknesses must be well characterized and controlled. The design process for the optimized photoresist stack becomes very similar to that employed for thin-film optical coatings.

4.10 Photoresist stack design for basic two-layer dielectric GMR structure

To improve lithographic exposure and RIE fabrication of GMR devices based on the two-layer structure of Fig. 2.1 (fused-silica substrate with 190 nm HfO_2 waveguide with 110 nm SiO_2 grating layer), the use of a thin metal layer below the photoresist was investigated. The basic two-layer structure on transparent fused silica substrates suffered from an unwanted low-frequency “noise” interference pattern superimposed on the desired primary grating structure [36]. This effect is shown in Fig. 4.17.

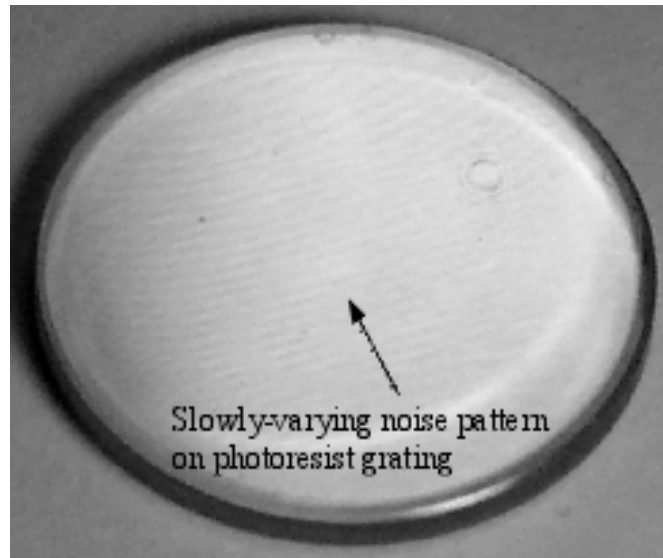


Figure 4.17. Low-frequency noise pattern on a photoresist grating. This noise is due to back-surface reflection from the transparent fused-silica substrate [4, 36].

This slowly-varying, unwanted interference pattern is due primarily to reflections from the back surface of the fused-silica substrate during photoresist exposure. By depositing a thin (approximately 15 nm) layer of Chromium on the top surface of the substrate before deposition of the photoresist layer, the back reflections during photoresist exposure were largely attenuated. Thin metal layers on the order of 15 nm are transparent both at visible and UV wavelengths although the transmitted intensity is attenuated by approximately 50% to 85%. Fig. 4.18 shows the simulated intensity profiles for the two-layer dielectric waveguide structure on a fused silica substrate.

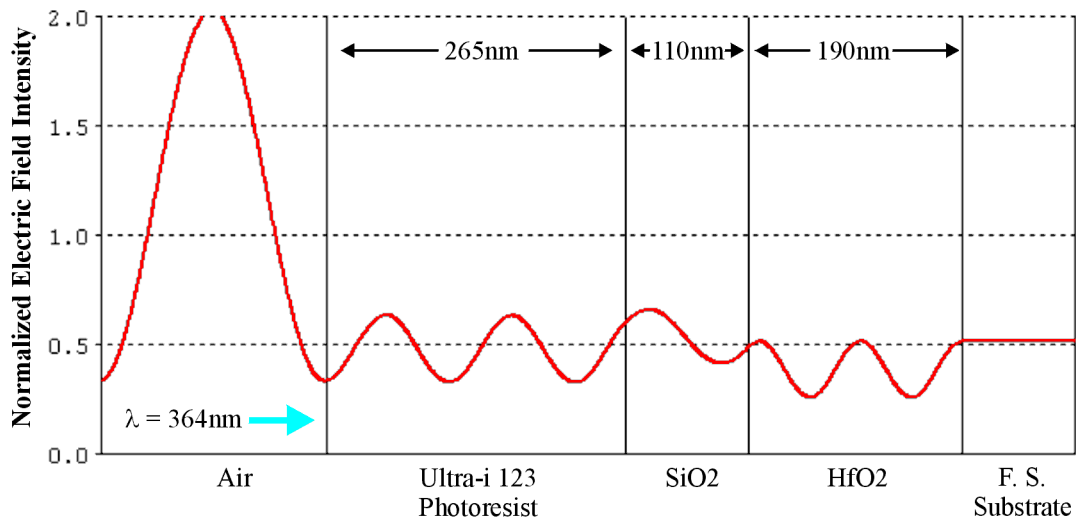
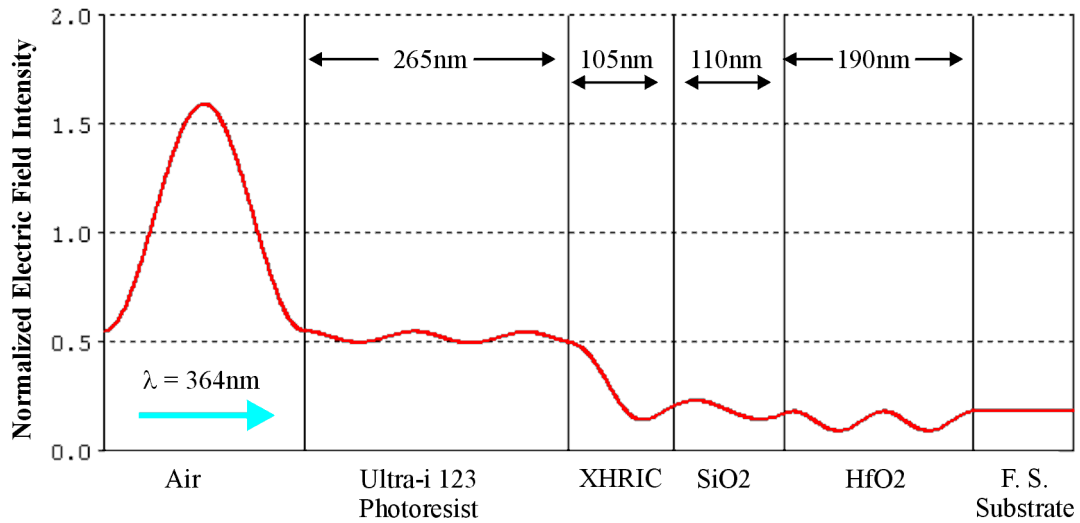
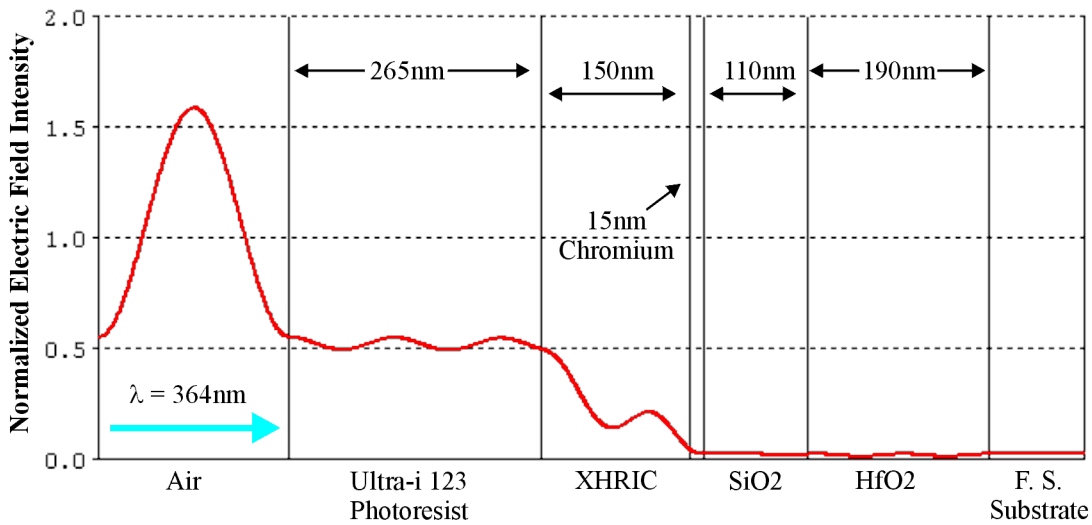


Figure 4.18. Calculated profile of normalized electric field intensity in the direction normal to the substrate during photoresist exposure for two-layer GMR structure of Fig. 2.1. The photoresist layer thickness is optimized to minimize standing waves in the photoresist layer without inclusion of a BARC layer. $\theta_{\text{half}} = 36^\circ$ corresponding to the incident angle to produce a 310 nm grating period.

Fig. 4.18 shows the intensity profile in the photoresist layer due to reflection at the various interfaces between the substrate, waveguide, cover, and photoresist layers without inclusion of a BARC layer. For this design, the photoresist layer thickness has been optimized to reduce amplitude of the standing waves during exposure. Note that due to the substrate transparency, 50% of the 364 nm incident light is transmitted into the substrate. A significant fraction of this transmitted light is reflected back from the substrate air interface and contributes to the slow-varying interference pattern shown in Fig. 4.17. For this simulation model, the actual phase of the light reflected from the back side of the substrate is neglected (assumed to be 0 degrees) due to the large substrate thickness (approximately 2.0 mm).



(a)



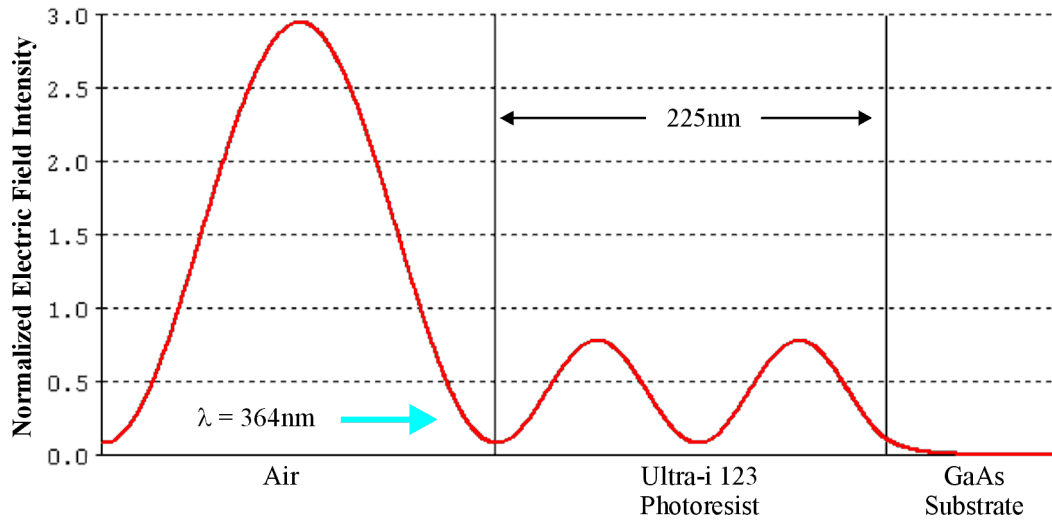
(b)

Figure 4.19. Calculated profile of normalized electric field intensity in the direction normal to the substrate for two-layer GMR waveguide structure with inclusion of BARC layer. (a) Intensity profile after inclusion of an optimized BARC layer. Note that the intensity in the substrate has been reduced to approximately 20%. (b) Intensity profile after inclusion of a 15 nm Chromium hard mask layer and BARC coating. Note that the BARC layer thickness must be adjusted to compensate for the increased reflectivity of the Chromium layer. $\theta_{\text{half}} = 36^\circ$ corresponding to the incident angle to produce a 310 nm grating period.

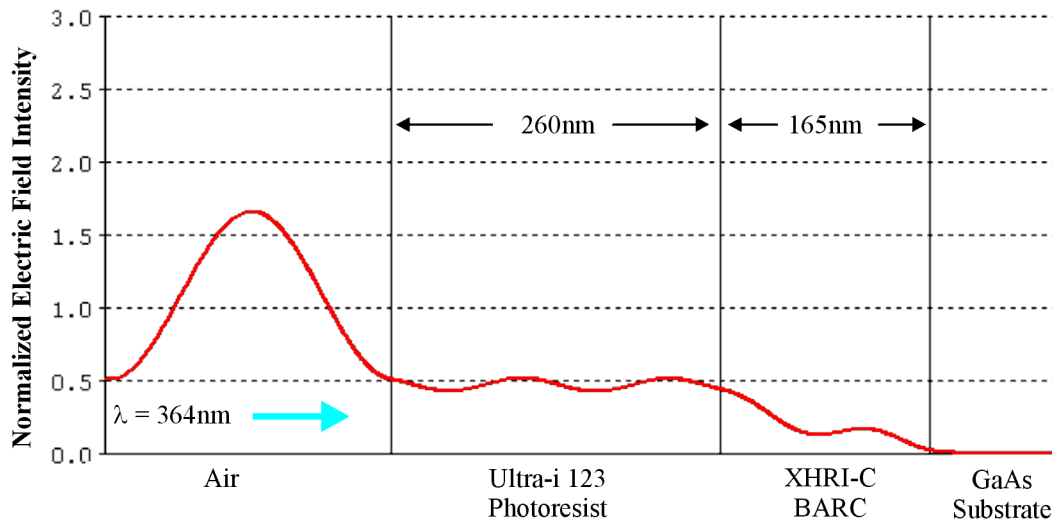
Figure 4.19(a) illustrates the effect of adding an optimized BARC layer below the photoresist layer. The BARC layer both reduces the amplitude of the standing wave in the photoresist layer as well as the magnitude of the light transmitted through the substrate to approximately 20%. Fig. 4.19(b) shows the optimized photoresist stack exposure profile after including the 15 nm Chromium hard mask layer. Note that it is necessary to adjust the BARC layer thickness from that of Fig. 4.19(a) to provide proper phase matching in the photoresist layer. The results of Fig. 4.19 indicate that the inclusion of the optimum thickness BARC layer can greatly reduce the photoresist standing wave effects as well as attenuate the standing wave contribution from the back side of the substrate. The inclusion of the 15 nm Chromium hard mask layer essentially eliminates any interference effects from the backside of the substrate. It was found in practice that the standing wave effects in the photoresist were mitigated both with and without inclusion of the Chromium hard mask layer. Due to simplified dry etch processing, the lift-off mask method was ultimately employed in the work of [4, 36].

4.11 Photoresist stack design for patterning of GMR-SEL structure on GaAs

The incorporation of GMR mirrors into semiconductor lasers as described in later chapters requires patterning of sub-micron gratings on GaAs/AlGaAs substrate layers. The GaAs substrate reflectivity characteristics are similar to those of the silicon wafers used in Figures 4.13 through 4.15. The high reflectivity causes large amplitude intensity standing wave ratios in the photoresist layer during exposure without inclusion of a BARC layer below the photoresist. Fig. 4.20(a) shows this for a single optimized



(a)



(b)

Figure 4.20. Calculated profile of total electric field intensity in the direction normal to the GaAs substrate. (a) Intensity profile for a single photoresist layer with single wavelength thickness (even number of quarter wavelengths) provides minimized standing wave in photoresist. (b) Intensity profile for optimized photoresist stack including a BARC layer. $\theta_{\text{half}} = 36^\circ$ corresponding to the incident angle to produce a 310 nm grating period.

photoresist layer on a GaAs substrate. The actual substrate layers of the GMR-SEL structure are comprised of $\text{Al}_x\text{Ga}_{1-x}\text{As}$ layers with a 20 nm GaAs cap layer

These GaAs/ $\text{Al}_x\text{Ga}_{1-x}\text{As}$ layers are highly absorptive at the 364 nm exposing wavelength and the light transmitted into the substrate is absorbed within approximately 20 nm. For the simulated intensity profiles of Fig. 4.20, the underlying AlGaAs layers were neglected to allow simulation with a simple GaAs substrate. Fig. 4.20(b) shows the effect of adding an optimized thickness BARC layer below the photoresist. As with previous results, the inclusion of the BARC layer greatly reduces the standing waves in the photoresist layer, thus enabling the formation of the required high-quality photoresist grating structures.

4.11 Summary of sub-micron photoresist grating fabrication

This chapter has outlined major factors that must be considered when fabricating high-quality sub-micron diffraction gratings on a variety of substrates. This begins with proper design and setup of the exposure interferometer. For this work, it was found that a two-beam interferometer provided superior results and ease of setup compared to the single-beam interferometer used in earlier work. It was also found that an active fringe stabilization system was necessary to compensate for environmental disturbances that reduced the quality or even prevented formation of high quality photoresist grating. A simple active fringe stabilization system using a CCD camera was described and implemented. This system provided fringe correction better than $\pm 1/100$ fringe during the exposure period. Finally, careful analysis of the photoresist layers must be performed to mitigate unwanted secondary standing wave effects in the photoresist layer during

exposure. These secondary interferences patterns become significant on high-reflectivity substrates and can completely degrade the resulting photoresist structure. The inclusion of a bottom anti-reflection coating (BARC) with optimized thickness below the photoresist layer can effectively eliminate these unwanted standing wave effects. In summary, this chapter has described necessary and practical methods and procedures for holographic patterning of high-quality sub-micron photoresist gratings. These methods can be useful for fabrication of the GaAs/Al_xGa_{1-x}As GMR laser structures of central interest in this research.

CHAPTER 5

ELECTRON-BEAM LITHOGRAPHY AND REACTIVE ION ETCHING FOR FABRICATION OF SUB-MICRON GRATINGS

Previous fabrication steps of the guided-mode resonance surface-emitting laser (GMR-SEL) devices included molecular-beam epitaxy (MBE) wafer growth, wafer material characterization, and refinement of the GMR grating design parameters as described in the Chapter 3. All post-wafer-growth output wavelength tunability is through variation of the grating parameters including period, depth, and fill factor. Subsequent fabrication steps include lithographic definition of the grating patterns and etch-transferal of the grating pattern into the GMR waveguide-grating layers. In this work, electron-beam lithography was selected to allow definition of different GMR-SEL device sizes and shapes as well as devices with different grating patterns.

This chapter describes patterning of the sub-micron grating structures required for GMR-SEL lasers by electron-beam lithography followed by reactive-ion-etching (RIE) transfer into GaAs substrates. The device patterns are written in hydrogen-silsesquioxane (HSQ) resist. RIE etching of HSQ grating patterns on GaAs substrates is performed with a $\text{Cl}_2 / \text{BCl}_3$ chlorine-based chemistry.

5.1 Sub-Micron Grating Fabrication for GMR-SEL devices

One of the most critical components of a GMR-SEL is the waveguide-grating structure. As detailed in previous chapters, the grating period, final etch depth, and grating fill factor determine the resonant operating wavelength as well as the coupling efficiency of the waveguide-grating device. A key requirement of the grating structure is uniformity of the grating parameters over the device area. The interferometric lithography system using active fringe stabilization described in Chapter 4 is an ideal system for producing uniform grating structures over large (several cm^2) substrate areas. One disadvantage of the interference lithography method is that to fabricate finite devices, a second lithography step must be performed to define the GMR device profile.

This extra lithography step requires fabrication of an additional mask pattern that must be accurately aligned with the grating pattern. Another difficulty in fabrication arises due to photoresist degradation during dry etch (RIE) processing; a secondary “hard mask” must be employed. For the GaAs/ $\text{Al}_x\text{Ga}_{1-x}\text{As}$ material system employed in this work, a deposited dielectric material such as SiO_2 is used since most etch processes for metal mask materials will damage the underlying substrate layers. Finally, GMR-SEL laser structures have been proposed [12] using second-order gratings in the central region with first-order gratings employed at each end of the structure [68] (similar to those employed in conventional distributed feedback / distributed Bragg reflector surface-emitting (DFB/DBR-SE) laser structures [69], but without the central grating phase-shift.) Fabrication of first-order gratings with UV interference lithography requires very large interference angles

beyond the limit of the interferometric lithography exposure system (approximately 190 nm for grating periods in air when utilizing a $\lambda = 364.6$ nm Argon laser.)

5.2 Electron-Beam Patterning of Sub-Micron Diffraction Gratings

An alternative to interferometric lithography definition of the sub-micron GMR-SEL grating patterns is the use of electron-beam lithography. In this method, a high voltage electron beam is scanned across the wafer surface exposing the desired pattern in a resist material. One primary advantage of electron-beam lithography is that both the grating pattern as well as the overall GMR-SEL device structure is patterned in one step. This eliminates the need for a second lithography step to pattern the GMR-SEL device perimeter after first defining a large-area uniform grating over the full substrate surface. Additionally, the use of electron-beam lithography allows patterning of GMR devices with both first and second-order grating periods in the same device. Fabrication of multi-period devices is more difficult with interference lithography techniques.

One primary disadvantage of electron-beam lithography is the limited field size that can be patterned without moving the substrate. To expose patterns larger than the electron-beam field size, the substrate is laterally shifted between adjacent fields resulting in some misalignment between the fields (stitch error). When patterning large-area optical diffraction gratings, this stitch error can significantly degrade the performance of the resulting structures due to the relative grating phase shift that occurs in the areas between adjacent fields. This effect is analogous to a discontinuity or impedance mismatch between regions of an electrical waveguide. Defects due to stitch errors can be minimized through maintaining rigorous environmental stability and by performing frequent machine

calibration. For this work, a Leica VB6-HR E-Beam Lithography System was used [Cornell Nanofabrication Facility (CNF), Ithaca, NY]. This is an advanced electron-beam lithography system operating with a 100kV field emission voltage for patterning up to 300 μ m square field sizes at a maximum beam frequency of 25MHz.

5.3 Electron-Beam Resist Materials

One of the most popular and commonly used resist patterning materials for e-beam lithography is polymethyl-methacrylate (PMMA) [70]. This material is typically used as a positive photoresist that is exposed by bombardment with high energy electrons. The electrons cause breakdown of the polymer allowing the exposed PMMA to be dissolved when developed in a diluted Methyl-Isobutyl-Ketone (MIBK) solution. A primary disadvantage of PMMA is the poor etch resistance characteristic. The PMMA photoresist mask is quickly eroded during dry-etch processing (RIE). For this reason, PMMA is often used to pattern a secondary hard mask such as SiO₂ or a metal that is more resistant to the RIE etch processing. Other polymer e-beam resist materials are available which provide improved etch process characteristics, but generally at the expense of reduced exposure sensitivity or resolution [71].

5.4 Hydrogen-Silsesquioxane (HSQ) as a Negative Electron-Beam Resist

One additional resist material gaining popularity for electron-beam lithography is Hydrogen-Silsesquioxane (HSQ). This material was originally developed as a spin-on low-k dielectric material used for trench isolation and planarization in semiconductor electronics applications [72]. It has been demonstrated that this material behaves as a high-resolution

negative resist when subjected to electron bombardment [73-81]. The smallest features defined by electron-beam lithography (less than 10 nm) have been exposed in HSQ resist [75,76]. HSQ is similar to spin-on glass (SOG) materials used in both semiconductor and optical applications. It is initially spin-deposited on the wafer followed by a low-temperature soft bake near 200°C to remove the solvent base. In conventional electronic applications, the HSQ layer is then baked at high temperature (near 400° C) yielding a semi-porous SiO₂ layer. Final layer thickness and density are determined by the starting HSQ viscosity (solids content), spun layer thickness, and final bake time and temperature.

Liquid HSQ is comprised of [HSiO_(3/2)]₈ (given as % solids) molecules suspended in an MIBK solution [73, 77, 82]. The percent solids and spin speed determine the initial deposited-layer thickness. When HSQ is used as an electron-beam resist, it is deposited and soft baked at low temperature (approximately 225°C) to remove the solvents. When exposed to the electron beam, the hydrogen bonds are broken leaving ionized SiO_(2/3) molecules. These molecules bond with adjacent SiO molecules resulting in a semi-crystalline SiO₂ matrix material (the SiO bonds are stronger than the SiH bonds). The HSQ layer is essentially cross-linked by exposure to the electron beam [80] resulting in patterned SiO₂-like regions in the resist layer. A post-exposure bake at 225°C is performed to drive off the excess hydrogen resulting from exposure and improve cross-linking. Immersion in tetra-methyl ammonium hydroxide (TMAH) or potassium hydroxide (KOH) solutions (standard organic photoresist developers) dissolves the unexposed regions leaving behind a SiO₂ hard mask layer. Since this SiO₂ hard-mask layer is patterned directly in the e-beam

lithography process, the need for deposition and etch processing of a secondary hard mask is eliminated.

A wide variety of prototype electrical, micro-mechanical, and optical devices with a wide range of feature sizes have been patterned by electron-beam lithography using HSQ as the resist [75-81]. Only limited patterning has been performed using HSQ resist on GaAs substrates [79, 80]. At the time of this writing, this is the first work describing the patterning of large-area uniform first and second-order diffraction gratings for laser devices with HSQ on GaAs substrates. Initial work was begun by performing basic dose characterization of the HSQ resist to produce uniform grating patterns.

5.5 Electron-Beam Exposure Dose Testing Using HSQ Resist on GaAs Substrates

The first test was begun by spin-coating a clean epitaxial-grade GaAs wafer with a diluted HSQ solution as used in previous work on silicon wafers [81]. In this case, the HSQ resist solution was made from Dow FOx-17 (HSQ) diluted 2:1 MIBK:HSQ yielding an unbaked film thickness of 155 nm. After an initial two-minute soft bake on a 225°C hot plate, the film thickness was reduced to approximately 145 nm. The wafer was mounted to a calibrated sample stage in the e-beam system and exposed with the pattern shown in Fig. 5.1. This pattern was 300 μ m x 300 μ m corresponding to the maximum field size of the e-beam lithography system (325 μ m is the absolute maximum dimension for the VB-6, but pattern distortion is likely near the edges.)

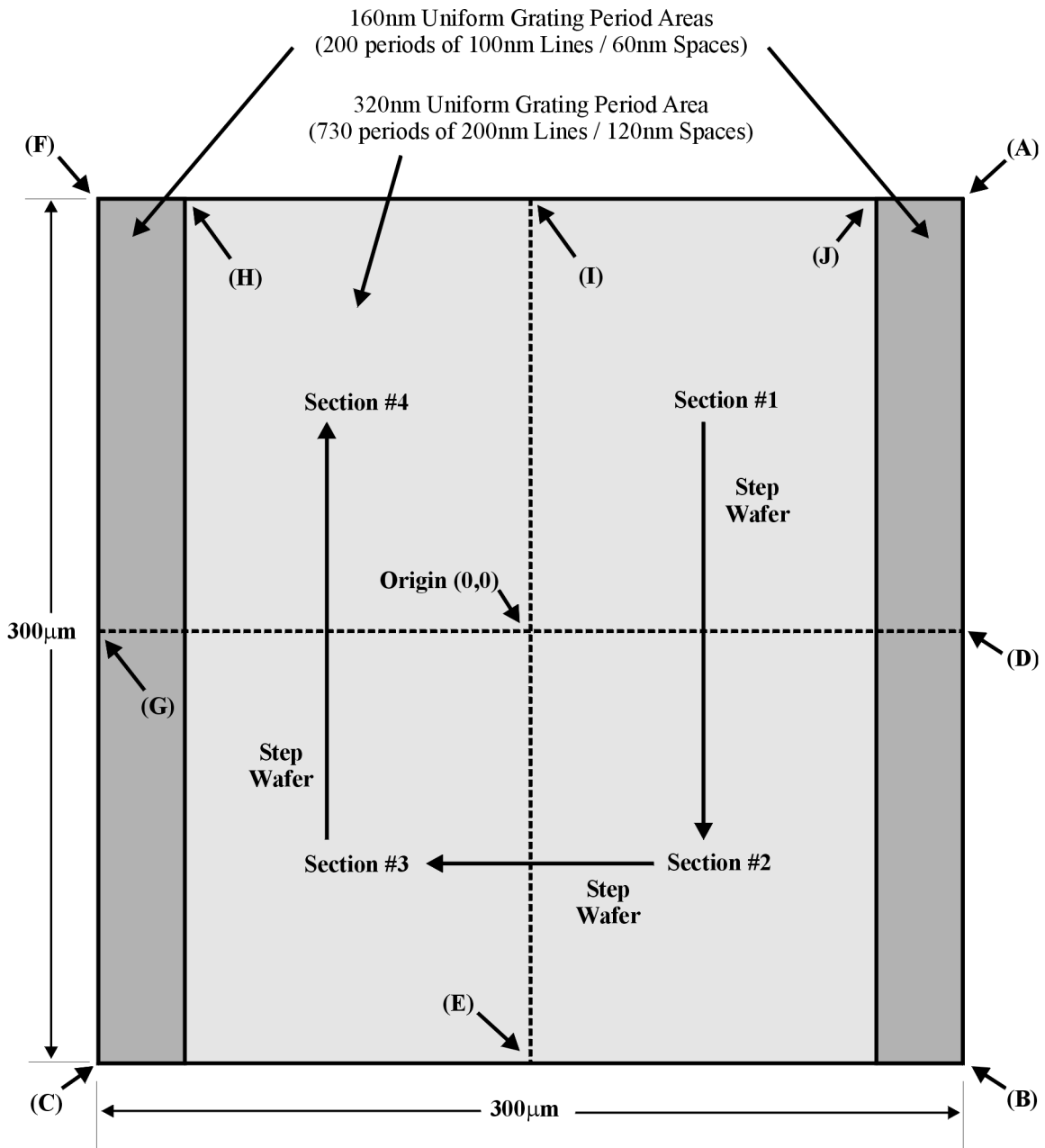


Figure 5.1. Exposure dose-test pattern for electron-beam exposure characterization of HSQ gratings on GaAs. Critical points for exposed-pattern inspection are labeled (A) through (J). Note that the 300µm x 300µm pattern is offset from the origin by 150µm causing the pattern to be exposed in four sections. This was done to allow characterization of the stitch overlap areas (D, E, G, and I) for both first and second-order gratings (160 nm and 320 nm periods respectively.)

This pattern was chosen to characterize both the required exposure dose range for HSQ resist on GaAs as well as the stitch error of the e-beam system. The pattern is comprised of 200 periods of 160 nm-period first-order grating (100 nm lines and 60 nm spaces) at each end of a second-order grating. The center section was comprised of 730 periods of 320 nm-period second-order grating (200 nm lines and 120 nm spaces.) The 62.5% grating fill factors for the 160 nm first-order and 320 nm second-order gratings were chosen to allow characterization of GaAs etch processing where mask erosion or etch undercutting occur. The exposure dose pattern of Fig. 5.1 was offset from the origin by 150 nm (half of the 300 μ m field size) in both x and y causing the e-beam system to stitch the full pattern in 4 stepped sections. This allowed the stitch error to be measured for overlapping sections for both types of grating period at points (A) through (J) indicated in Fig. 5.1.

A simple e-beam control software batch file was written to generate a 100-step (20 elements by 5 elements) array of the pattern with each pattern assigned a dose varying linearly from 280 μ C/cm² to 900 μ C/cm². Based on the 100 nm line widths of the 160 nm first-order grating pattern, a 10 nm step size was selected for the e-beam pattern generator. This allowed each patterned 100 nm grating line to be formed by 10 adjacent passes with 10 nm offset of the electron beam, thus giving a dose averaging effect to minimize any variations in the exposing beam current. Based on the 280 μ C/cm² minimum dose and the 25MHz maximum beam sweep frequency, a 5nA beam current was selected.

For the Leica VB-6 E-Beam patterning system, the selected beam current is fixed throughout the patterning session to maintain stable and repeatable exposure dosage. Typically, the field-emission electron beam current is set prior to sample loading and system

calibration to allow the field emission element to temperature-stabilize at the chosen beam current. The actual exposure dosage is controlled by the beam sweep time used to pattern specific features. Nominal beam current values relevant to this work for the VB-6 system are: 1nA, 2nA, 5nA, and 10nA. The actual value is chosen so that the minimum exposure dose corresponds to the maximum electron-beam sweep frequency (below the 25MHz maximum frequency.) For the $280\mu\text{C}/\text{cm}^2$ dose, the maximum beam sweep frequency is calculated to be 17.85MHz resulting in a 50.4 second exposure time for one pattern. For the pattern exposed at to $900\mu\text{C}/\text{cm}^2$, the beam sweep frequency is reduced to 5.55MHz corresponding to a 162 second pattern-writing time.

After exposure, a two-minute post-exposure bake was performed on a 225°C hot plate. The substrate was then developed for 2 minutes in diluted TMAH (AZ 300 MIF) developer followed by a 2 minute deionized (DI) water rinse and blown dry with dry-nitrogen. The resulting grating patterns were readily visible for all 100 patterned areas with visible diffraction being brightest for the devices with lower exposure doses. The exposure dose pattern wafer was then mounted (with no additional surface preparation) for SEM inspection.

The high-resolution scanning-electron-microscope (SEM) used in this work was capable of performing low voltage imaging of the SiO_2 HSQ pattern on a GaAs wafer without depositing a thin conducting film such as gold (Au) or gold / palladium alloy (Au /Pd) on the sample to enhance secondary-electron emission. For the exposure dose-test wafer, at low SEM accelerating voltages, there was sufficient detector gain to distinguish

the contrast in secondary-electron emission between the GaAs substrate and the SiO₂ resist layer, yielding the high-resolution micrographs as shown in Figures 5.2 and 5.3.

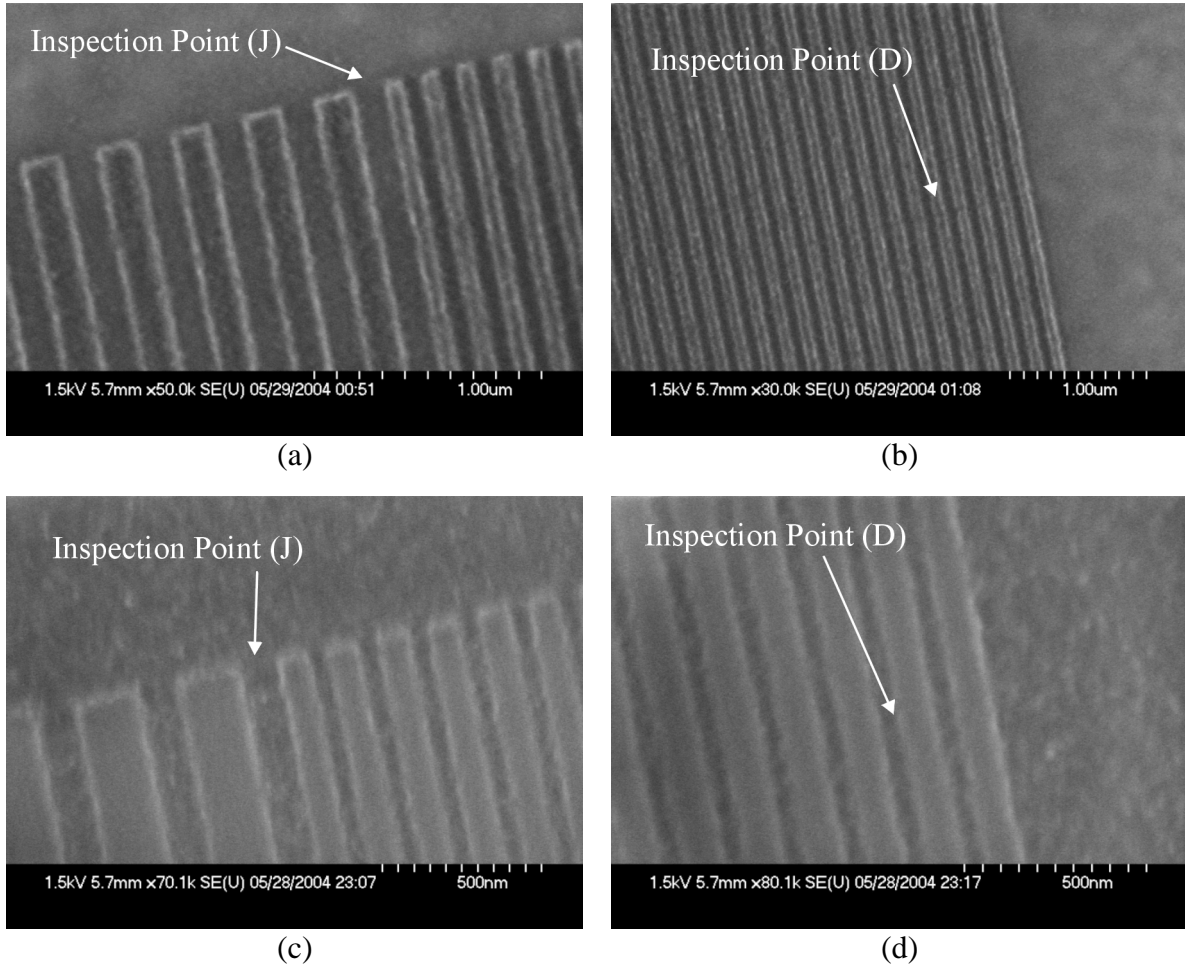


Figure 5.2. SEM micrographs of the initial exposure dose pattern shown in Fig. 5.1. Inspection Point J shows transition between 160 nm and 320 nm grating periods. Inspection Point D indicates an overlap area of adjacent exposure fields. For (a) and (b): Exposure dose = $288\mu\text{C}/\text{cm}^2$ and grating fill factors are approximately 50%. For (c) and (d): Exposure dose = $892\mu\text{C}/\text{cm}^2$ and grating fill factors are approximately 62%. Note that the stitch overlap areas are barely discernible in (b) and (d).

The low-voltage dielectric imaging technique works well for determining critical dimensions at normal incidence to the substrate, but image quality is degraded at oblique angles of incidence.

5.6 HSQ Exposure Dose Pattern Results

Selected results of the initial electron-beam exposure dose pattern test are shown in Figures 5.2 and 5.3. Figures 5.2(a) and (b) are for a pattern exposed at $288\mu\text{C}/\text{cm}^2$ at inspection points J and D. Inspection point J shows the transition between the 320 nm and 160 nm grating periods. Inspection point D shows the typical stitch overlap error obtained for this series of exposures. The stitch overlap areas are barely discernable indicating that the electron-beam exposure tool was in excellent calibration. The grating fill factors of Fig. 5.2(a) are approximately 50% indicating slight underexposure of the pattern from the 62.5% designed fill factor. Figures 5.2(c) and (d) show the same inspection points for a pattern exposed with $892\mu\text{C}/\text{cm}^2$. In this case, the grating fill factors at inspection point (J) are approximately the 62.5% designed value. Again, the stitch error occurring at inspection point (D) is negligible. In Figures 5.2(b) and (d), the grating duty at the edges of the 160 nm grating period area was approximately 70%. This was attributed to minor proximity-effect exposure described in following sections.

At many points during SEM inspection of the initial exposure-dose patterns, shadowing was observed in the SEM images taken near the outer corners of the patterns. The shadowing effect often occurs during SEM imaging due to specimen charging from the electron probe beam. This shadowing generally increases with dwell time in the SEM image area. This was also the case for the low beam voltage imaging used for inspection

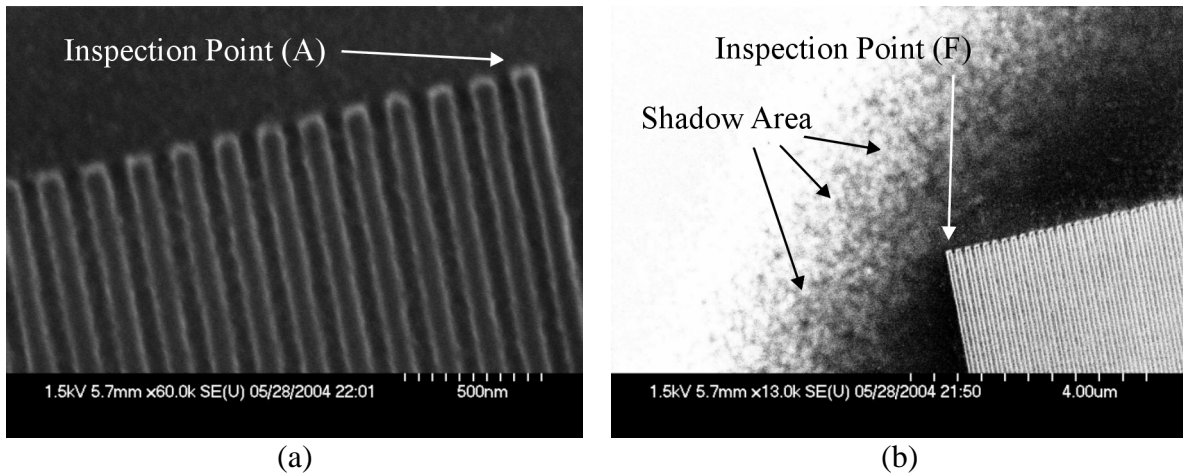


Figure 5.3. SEM micrographs of the initial exposure-dose pattern shown in Fig. 5.1. (a) Inspection point A shows the outer corner of the 160 nm grating period for an exposure dose of $892\mu\text{C}/\text{cm}^2$. (b) Shows inspection point F for the same device in reverse contrast at lower magnification to illustrate the shadow area attributed to sample saturation during SEM imaging.

of the initial exposure-dose patterns. Fig. 5.3(a) shows the same device of Fig. 5.2(a) and (b) at inspection point (A) at the outer corner of the 160 nm grating region. Here, the shadowing effect is not observed. Fig. 5.3(b) shows the same device near the corner at inspection point (F). The image is in reverse tone to better contrast the shadow area that was observed at lower magnifications for many of the devices. This shadowing effect was dismissed as an artifact from the SEM imaging process.

The results of the initial electron-beam exposure-dose characterization suggested that the HSQ resist material possessed wide exposure dose latitude for successful patterning of high-quality sub-micron grating patterns. The results indicated that the grating fill factors (linewidths) closely approximated the 62.5% design values for exposure doses near $900\mu\text{C}/\text{cm}^2$ while exposures at doses near $300\mu\text{C}/\text{cm}^2$ yielded slightly underexposed patterns with grating fill factors near 50% in the central regions.

5.7 Wet Etching of GaAs Gratings Using HSQ Resist

Due to the apparent high quality of the HSQ gratings obtained from the initial electron-beam exposure dose test, a wet-etch study was performed on this same sample to determine the feasibility of wet etching the GMR-SEL device gratings. A 1:8:1000 HSO₄:H₂O₂:H₂O solution was used to wet-etch the GaAs substrate [83]. Although this etch solution typically results in a 80% ratio of resist-undercutting to etch-depth for GaAs, the resulting triangular gratings would still be acceptable for use in GMR-SEL laser devices. The gratings would have sufficient etch depth to yield good optical coupling of the resonant waveguide modes. Various samples were etched for times ranging between one and four minutes to obtain expected etch depths in the range of approximately 35 nm to 140 nm.

Figure 5.4 shows the results of the wet etching study. At this point, it was discovered that all patterned areas from the initial dose test suffered from overexposure due to proximity effects. Fig. 5.4 shows that there is a uniform layer of exposed HSQ under the entire grating pattern areas. This layer effectively masked the substrate and prevented etching of the grating pattern. The overexposed regions became more pronounced at increased exposure doses approaching the 900 μ C/cm² maximum and are not shown here. At this point, the effects and methods for mitigation of the electron-beam exposure-proximity-effects were investigated.

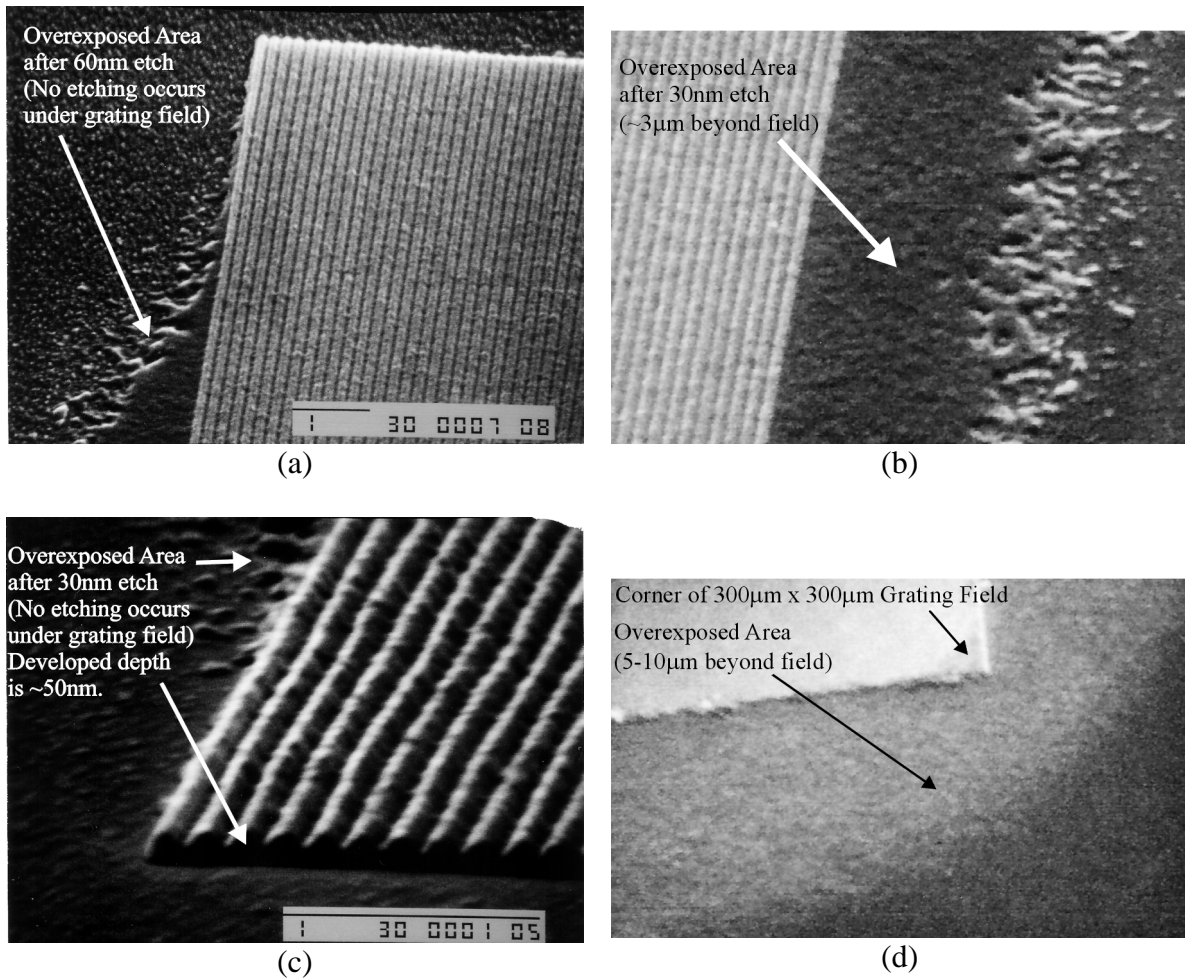


Figure 5.4. SEM micrographs of wet-etched initial exposure-dose patterns using an HSQ resist mask on a GaAs substrate. (a) Through (c) show that etching only occurs near the perimeter of the pattern with no substrate etching under the grating field. This is due to an overexposed HSQ layer below and around the patterned areas. The exposure doses for (a) through (c) are each $286\mu\text{C}/\text{cm}^2$. (d) Shows the extents of the overexposed layer before wet etching in a 1:8:1000 $\text{HSO}_4:\text{H}_2\text{O}_2:\text{H}_2\text{O}$ solution for an exposure dose of $315\mu\text{C}/\text{cm}^2$.

5.8 Electron-Beam Proximity Exposure Effects

The proximity effects that occur during electron-beam lithography are primarily a result of secondary-electron scattering caused by the high-energy writing beam. The incident high-energy electrons penetrate into the substrate layers as functions of electron velocity, material type, and density. The electrons experience both forward and large-angle back-scattering events. Additionally, electrons from the exposing beam can also produce secondary-electron scattering but with much lower electron energies. These low-energy back-scattered electrons are responsible for the proximity-effect overexposure shown in the previous Section. A typical illustration of this effect for PMMA resist on a silicon substrate is shown in Fig. 5.5 [70, 84].

A popular method for modeling the electron scattering events follows the Monte-Carlo method where a large number of individual electron trajectories are calculated based on random scattering events [84]. The initial electron energy and substrate material parameters allow the average of these scattering effects to be estimated.

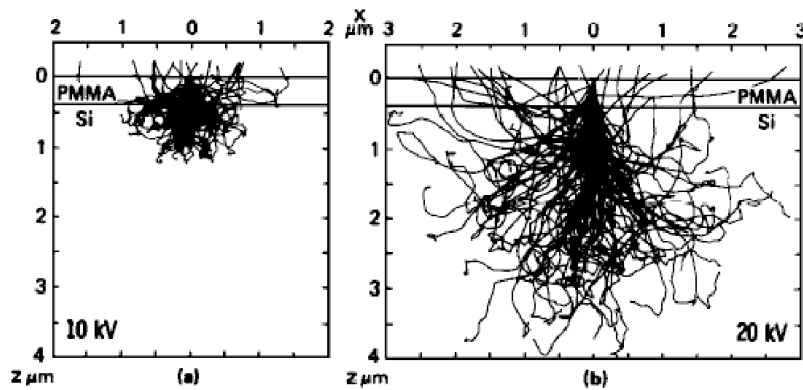


Figure 5.5. Monte Carlo simulation profiles for electron scattering events in a PMMA resist layer on a silicon substrate. Electron energies are (a) 10kV and (b) 20kV. [From Kyser and Viswanathan [84], 1975.]

Two Monte-Carlo simulation examples for different electron beam energies are shown in Fig. 5.5. Electron-beam lithography is typically performed at the highest available beam energy to minimize the electron scattering effects. The high-energy electrons penetrate deeply into the substrate causing the majority of scattering events to occur below the resist material. The exposure dose as well as exposure resolution is typically higher for increased electron-beam energy because the electrons undergo little scattering in the first pass through the resist material. For reduced electron-beam energy, more electrons are absorbed near the substrate surface (resist layer), but at the expense of beam broadening in the resist layer.

These effects are exemplified in the Monte Carlo simulations of Fig. 5.5. In Fig. 5.5(a), the majority of the scattering events occur near the PMMA to substrate interface. The trajectory simulations indicate that for the given conditions, the exposed dimension in the PMMA is approximately one micron due to the scattering events. In Fig. 5.5(b), the 20kV electrons penetrate deeply and most scattering events occur several microns below the substrate surface. The scattered dimension in the PMMA is approximately half that of Fig. 5.5(a), thus resulting in improved feature resolution and linewidth control.

5.9 Proximity-Effect Correction

Numerous exposure techniques are used to minimize proximity exposure effects in electron-beam lithography [70]. One type of improvement can be gained by decreasing the resist thickness and / or increasing the electron energy, thus allowing the electron-beam to penetrate further into the substrate and reducing the scattering at the substrate surface. Most other methods for controlling proximity effects involve altering the exposure dose in

different areas of the pattern to take advantage of the non-linear exposure threshold characteristic of the resist material. In these methods, the specific pattern is analyzed to calculate the total exposure from both primary and secondary exposure sources (scattering.) Similar methods are employed in optical lithography exposure systems where mask diffraction and scattering effects are estimated and used to optimize the lithography pattern to obtain the designed critical feature dimensions.

One method used successfully in electron-beam lithography is “GHOST” patterning as shown in Fig. 5.6 [85]. In this method, a large-area background dose pattern that is the inverse of the proximity effect is supplied to the resist. The background energy dose is below the exposure energy threshold for the resist material. The original pattern is then written at a reduced dosage so that only the desired pattern receives a combined dose above the resist exposure threshold.

A second method for proximity effect correction in e-beam lithography is dose-modulation patterning. With dose-modulation patterning, different exposure doses are applied to specific areas of the pattern so that each region receives the correct dose total from the combination of direct patterning and the proximity exposure. In this work, a commercial software package was utilized to “fracture” the pattern into the different dose regions.

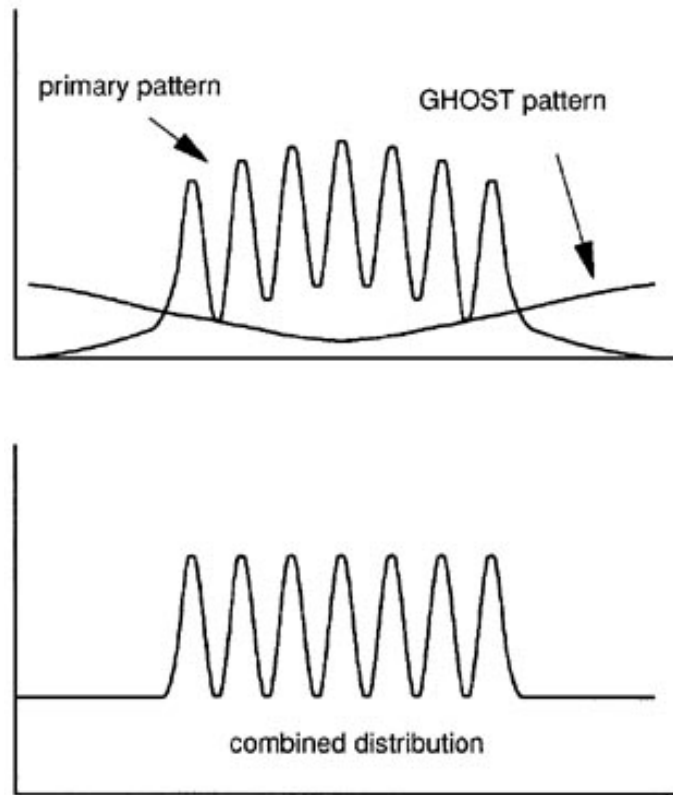
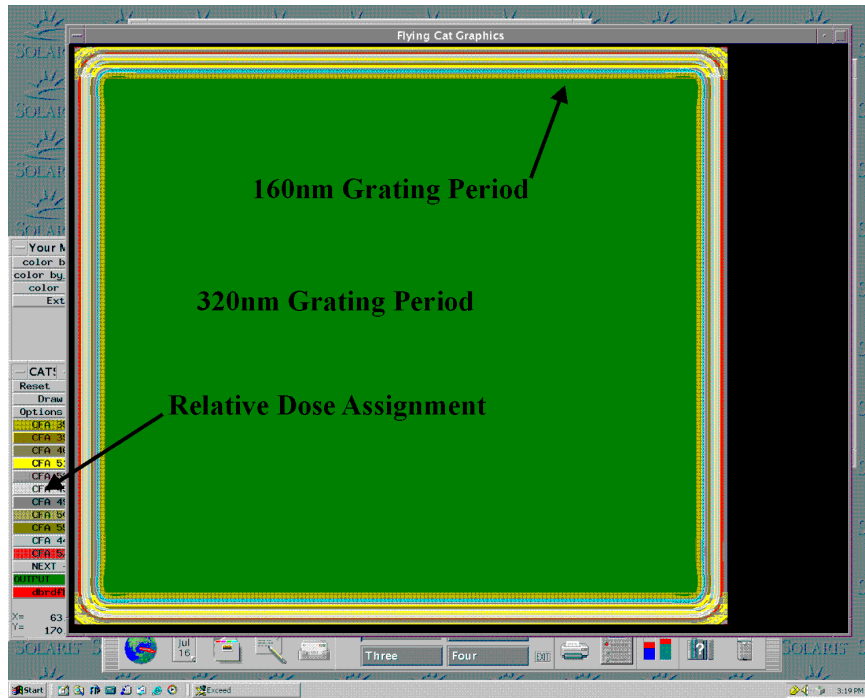
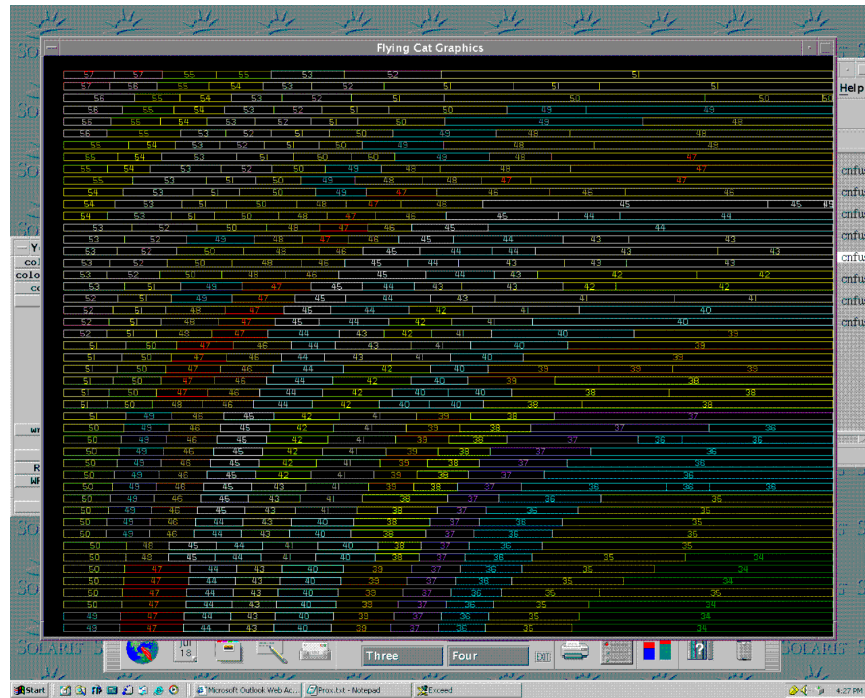


Figure 5.6. Schematic showing how the GHOST technique can be used to correct for the proximity effect. The top curves show the energy distribution in the resist for a group of seven lines from the primary exposure and from the GHOST exposure. The bottom curve is the resulting final energy distribution, showing the dose equalization for all the lines. [From [70]].

Monte Carlo simulations were performed for the test substrates used in this work with the SCELETON software package by the software vendor [86]. The first simulation was for a simple GaAs wafer with an 80 nm HSQ resist layer and the same Leica VB-6 e-beam system parameters used in the initial exposure dose tests. The GMR-SEL laser structure described in Chapter 3 (GaAs/Al_{0.2}Ga_{0.8}As waveguide) with an 80 nm HSQ resist layer was also analyzed with the SCELETON software. The output obtained from the SCELETON simulations was input to a second commercial software package



(a)



(b)

Figure 5.7. Screenshots of fractured grating pattern of Fig. 5.1 obtained from PROCECCO software. (a) shows the overall pattern with relative dose assignments according to color. (b) shows a detail of the fractured pattern and relative dose level numbering at inspection point C of Fig. 5.1. Note that this figure has been rotated by 90°.

PROXECCO by the same vendor, [87]. The PROXECCO software applies a meshing algorithm to “fracture” the desired pattern into different dose regions based on the combined energy of the original pattern and the electron-scattering dose caused by the patterning of adjacent dose regions. Each fractured area receives a different dose by varying the electron-beam sweep frequency in that region of the pattern area. Fig. 5.7 shows sample screenshots of the PROXECCO output. For the pattern of Fig. 5.1, there are 64 dose levels ranging between 0.64 to 2.4 times the base dose level.

5.10 Exposure Dose Testing for Proximity Effect Corrected Pattern

The proximity-effect corrected exposure-dose pattern of Fig. 5.7 was used both to characterize the useful HSQ exposure dose range and for RIE etch process optimization on GaAs substrates. The HSQ resist used in the remainder of this work was a 4% solids solution spun to a thickness of 80 nm. The soft bake and post-exposure processing remained the same from previous sections with the exception of the development time. It was observed that minor improvements in resist clearing between grating lines were obtained by increasing the development time in diluted TMAH to 6 minutes. Selected results are given in Figures 5.8 and 5.9.

Figure 5.8 shows HSQ grating structures obtained by exposure near the limits of the useful dose range for the pattern used and VB-6 E-Beam system parameters (100kV electron beam energy, 5 nm resolution, 10 nm step size, and basic stage calibration.) Fig. 5.8(a) shows that for an exposure dose of $420\mu\text{C}/\text{cm}^2$, the 160 nm period grating lines at the corners of the pattern (inspection point B) are slightly underexposed with variation

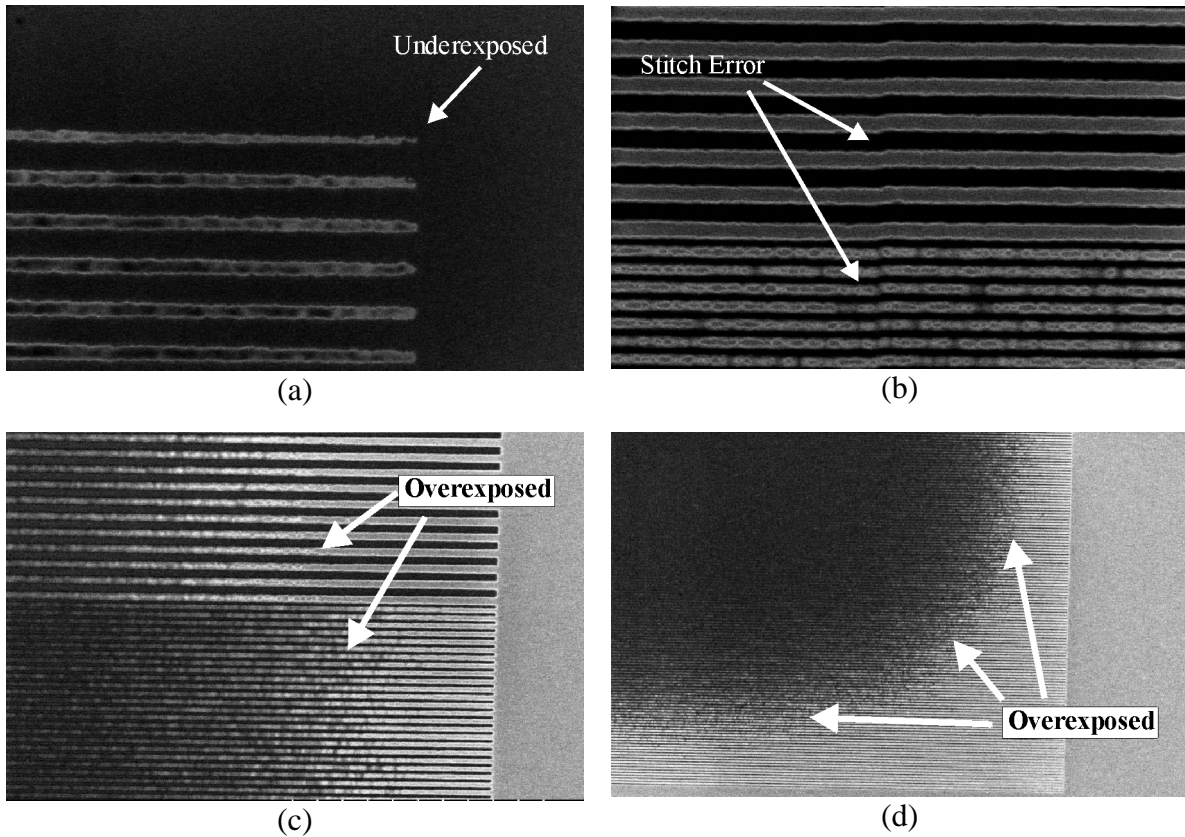


Figure 5.8. SEM micrographs of HSQ grating structures as functions of exposure dose. (a) shows that the 160 nm-period grating lines at the corners of the pattern (inspection point B) are slightly underexposed with variation in the final line width dimensions. The exposure dose for (a) and (b) is $420\mu\text{C}/\text{cm}^2$ and $540\mu\text{C}/\text{cm}^2$ for (c) and (d).

in the final linewidth critical dimensions. Fig. 5.8(b) shows that for the same exposure dose, at the transition areas between the 160 nm and 320 nm grating periods, the HSQ grating lines are clearly defined and there is good clearing between the grating lines.

Fig. 5.8(b) also shows that the VB-6 E-Beam lithography system exhibited approximately 30 nm of stitch error at the field overlap areas. This is in contrast to no measurable stitch error in the previous patterning results obtained after a full system calibration. (Full VB-6 system calibration takes approximately 10 hours of machine time and is generally cost-prohibitive to perform before each patterning session. Full system

calibration is typically performed on a bi-weekly to monthly basis for the VB-6 system used in this work. A basic stage calibration taking approximately 0.5 hours is performed before each patterning session.) The presence of significant stitch error indicated that field overlap of critical pattern areas should be avoided wherever possible. For the remainder of this work, most patterning and testing were performed with devices that fit within the 300 μm x 300 μm maximum field size.

Fig. 5.8(c) and (d) show that for a 540 $\mu\text{C}/\text{cm}^2$ exposure dose, central regions of the pattern are slightly overexposed. This characteristic is visibly apparent at low magnification, even under an optical microscope. The results of Fig. 5.8(c) and (d) show that for slightly overexposed areas, the widths of the grating lines remain relatively constant while the grating grooves are not completely cleared. Although these patterns were slightly overexposed, during RIE etching, some sputter-etching occurs that does allow substrate etching in the overexposed areas. This effect is described in greater detail in following sections.

Figure 5.9 shows grating patterns exposed with 440 $\mu\text{C}/\text{cm}^2$ and 500 $\mu\text{C}/\text{cm}^2$ doses within the 420 $\mu\text{C}/\text{cm}^2$ to 540 $\mu\text{C}/\text{cm}^2$ range of Fig. 5.8. Figures 5.9(a) and (b) show that while the patterns are completely defined, lines near the perimeter of the devices are slightly underexposed while the grooves between the lines are slightly overexposed. In Figures 5.9(a) and (b), the light areas between the grating lines indicate incomplete HSQ clearing within the grating grooves even after a 6 minute development. The poor groove clearing was more prevalent for shorter development times. Figures 5.9(c) and (d) are shown with higher contrast to illustrate that the patterned grating fill factor is

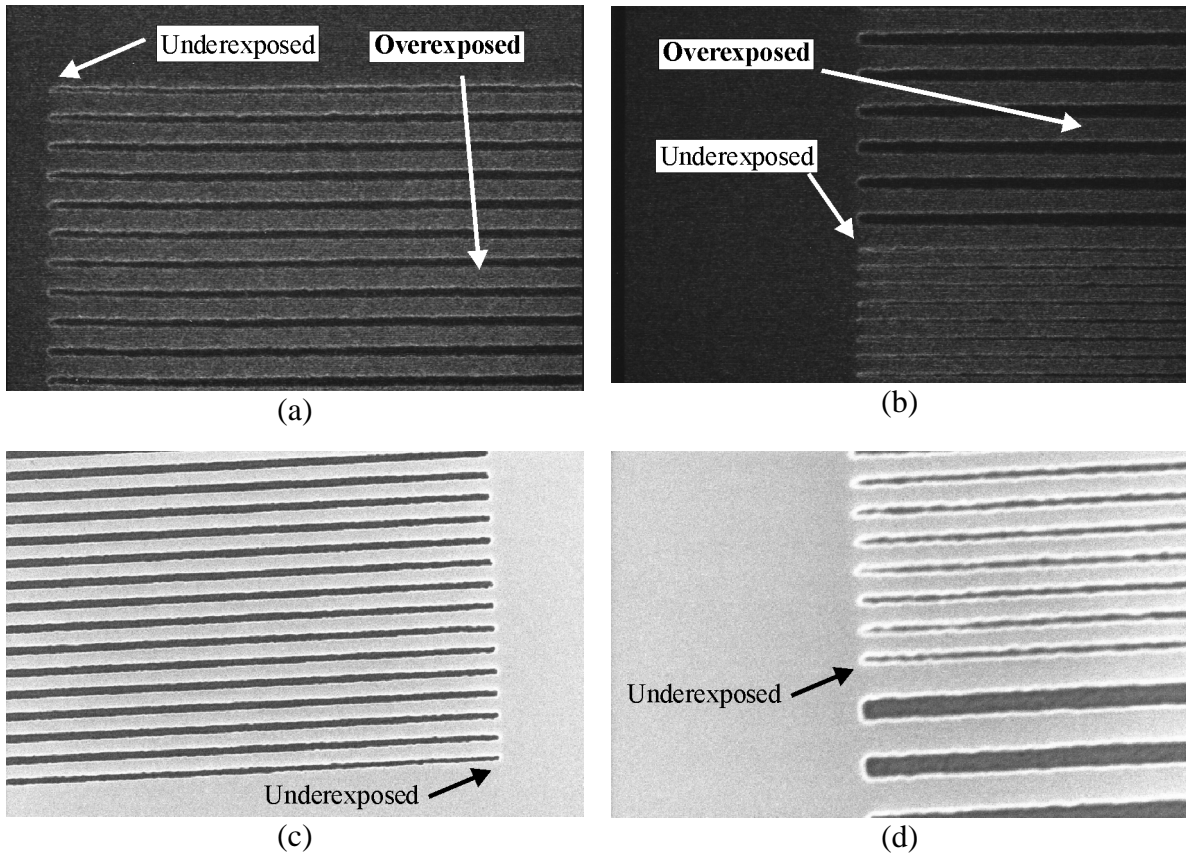


Figure 5.9. SEM micrographs of HSQ grating structures as functions of exposure dose. The exposure dose in (a) and (b) is $440\mu\text{C}/\text{cm}^2$; and the exposure dose in (c) and (d) is $500\mu\text{C}/\text{cm}^2$.

approximately 40% rather than the 62.5% design value. Under the high-contrast imaging conditions used for Figures 5.9(c) and (d), the overexposed areas are not readily visible, but do appear under the imaging conditions used in Figures 5.9(a) and (b).

The results of Fig. 5.9 show that the resulting patterns have fill factors significantly less than the 62.5% design value. Furthermore, the presence of both underexposed and overexposed areas in the same patterns indicates that the PROXECCO pattern-fracturing and dose-assignment algorithms require optimization. The proximity-corrected patterns used in this work were supplied free-of-charge by a third-party vendor and further

optimization or additional corrections were not available. While the proximity-effect corrections were not optimized, the resulting exposed patterns represented a significant improvement over the patterns without proximity correction. The results indicate that the optimized exposure dose for 100kV electron-beam patterning of 320 nm and 160 nm grating periods with 80 nm HSQ resist layers on GaAs substrates is in the range of $400\mu\text{C}/\text{cm}^2$ to $500\mu\text{C}/\text{cm}^2$. The remainder of this work including e-beam patterning of the GMR-SEL Wafer #2 described in Chapter 3 was performed with exposure doses in this range.

5.11 Reactive-Ion Etching (RIE) of HSQ Gratings on GaAs

The patterns obtained from the previous electron-beam exposure-dose characterization were used to develop a reactive-ion etching (RIE) process on GaAs substrates. The RIE etch processing parameters were then utilized for fabrication of the surface gratings required for the GMR-SEL devices. Ideally, the exposure-dose characterization and RIE etch process development should have been performed on the final GMR-SEL wafer structure, but due to a limited amount of this material, the process parameters were developed on GaAs wafers. RIE etching in this work was performed with a PlasmaQuest ECR (extended cyclotron resonance) load-locked etch system [CNF]. The turbo-pumped system used mass flow control (MFC) on all process gasses, LN2 substrate chuck cooling, and He cooling on the substrate backside.

The ECR etch system used a remote cyclotron microwave source with a tunable waveguide to ionize the process gases. The microwave energy is coupled into to the chamber to generate a low-pressure plasma in turn driven with a 13.56MHz RF source. Various process parameters include microwave power (forward and reflected), RF power

(forward and reflected), upper and lower magnet current, chamber pressure, substrate temperature, substrate loading (resulting in dc bias), and process time. The tuning dependency of the microwave and RF sources is coupled to the source power, chamber pressure, and total gas flow process parameters. Changes in any of the latter parameters required tuning and stabilization of the RF and microwave sources. Each of these process parameters determined the etch rate and resulting etch profiles. The plasma beam-shape between the anode and substrate (cathode) is controlled by upper and lower electromagnets. The plasma beam-shape to some degree, determines the directionality of the plasma that impinges on the substrate giving an additional margin of control to the resulting etch profiles (anisotropy.)

Initial etch processing was performed with a 4:10 (sccm ratio) $\text{Cl}_2:\text{BCl}_3$ gas mixture[88]. It was found that this etch mixture resulted in a large degree of undercutting (isotropic etching) in grating grooves that had good clearing between the HSQ grating lines. The grating grooves with poor HSQ clearing suffered from non-uniform etching. The net result was that large parts of the HSQ grating mask pattern were completely undercut resulting in mask delamination while other areas had inconsistent etch depths. The process gas mixture was modified to include Argon (to increase the amount of non-reactive sputter etching) to better penetrate the slightly overexposed areas of the HSQ mask [89]. Additionally, the Cl_2 content was reduced to promote anisotropy in the resulting etch profiles as well as to reduce the overall etch rate. The gas ratios and system parameters were systematically varied and results were characterized by SEM inspection. Final processing

was performed with a 15:10:1 (sccm ratio) Ar:BCl₃:Cl₂ gas mixture. The specific process parameters are summarized in Table 5.1.

Table 5.1. Process Parameters for RIE Etching of GaAs in ECR Etch System.

Parameter	Value	Comments
Process Gasses	15:10:1 Ar:BCl ₃ :Cl ₂	(sccm ratio)
Chamber Pressure	4 mTorr	
RF Power	45W / 10.3W	Forward / Reflected Power
Microwave Power	400W / 33W	Forward / Reflected Power
Magnet Current	16A / 50A	Upper / Lower Magnet
Substrate Temperature	0° C	(Helium Cooling)
Substrate Bias	24V	Function of RF tuning and pressure

A 30-minute system cleaning etch (20:4 O₂:CHF₃) was performed before each process session to insure uniformity of results. This was followed by a conditioning process run with a scrap of GaAs wafer to allow microwave and RF source tuning and system stabilization for the specific process parameters. The individual GaAs samples were mounted to a clean 4-inch silicon wafer for RIE etch processing with double-sided copper tape to insure good thermal conductivity before loading into the RIE etch system. Selected results are presented in Figures 5.10 and 5.11.

Figure 5.10 shows RIE-etched pattern results for GaAs gratings using an HSQ mask and the process parameters of Table 5.1. The samples were obtained from central regions of the patterns by sample cleaving. A thin layer of gold was deposited to improve on-edge SEM imaging. Fig. 5.10 shows final etched depth as a function of time

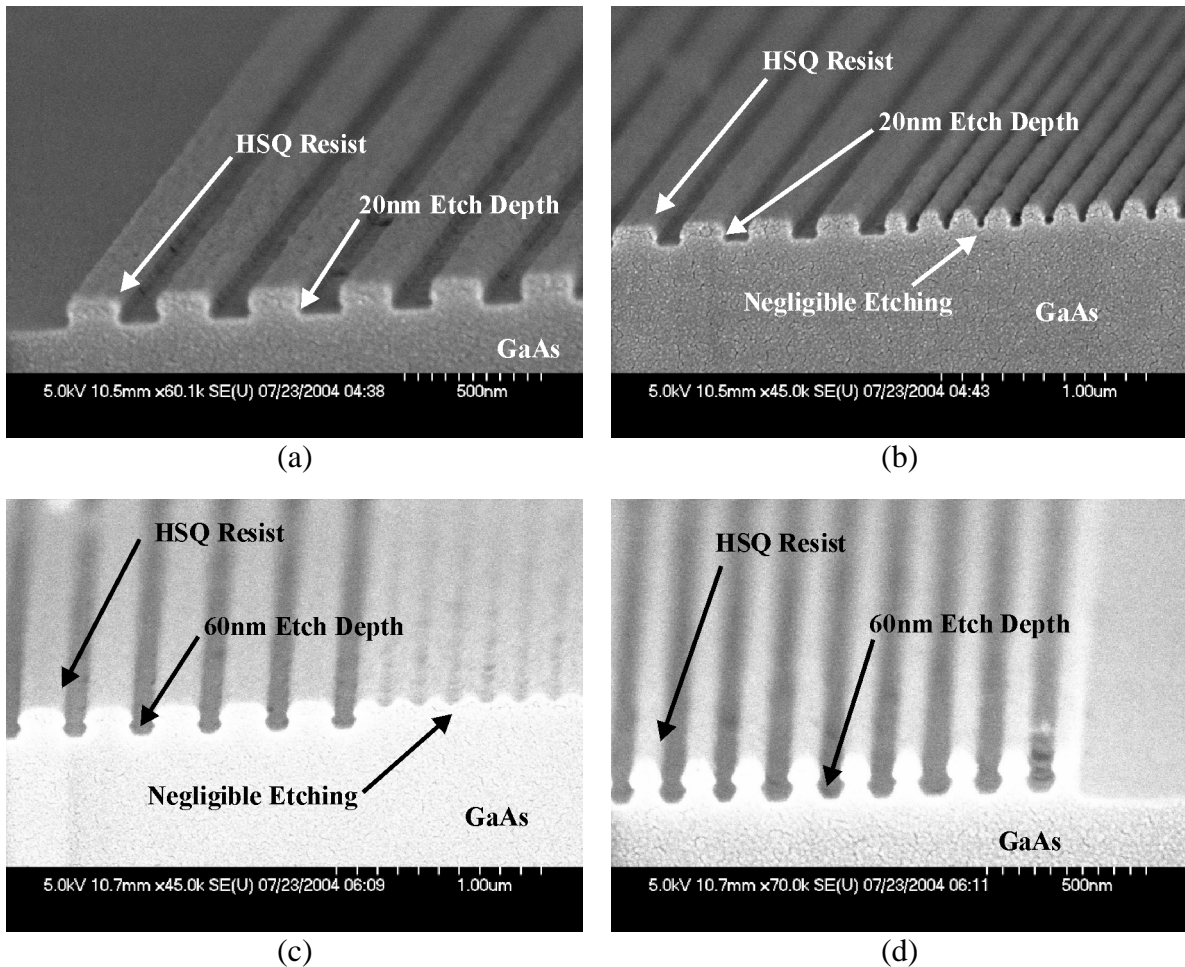


Figure 5.10. SEM micrographs of RIE-etched GaAs grating depth as functions of etch time. The pattern exposure dose in each figure is $420\mu\text{C}/\text{cm}^2$. (a) and (b) were etched for 30 seconds showing an approximate 20 nm etch depth. (c) and (d) were etched for 60 seconds showing an approximate 60 nm etch depth.

for grating structures patterned with a $420\mu\text{C}/\text{cm}^2$ exposure dose. The patterns of Figures 5.10(a) and (b) were etched for 30 seconds, while (c) and (d) were etched for 60 seconds. The results show that a 30-second etch results in a 20 nm etch depth while a 60-second etch results in a 60 nm etch depth. This indicates that the etch process is non-linear with time.

Fig. 5.10 also shows that the etch rate was a function of the pattern fill factor. The figures indicate that the etch rate of the 160 nm grating periods was less than the etch rate

for the 320 nm grating periods. The reason for almost no etching of the 160 nm grating period (with the longer 60-second etch) on the right side of Fig. 5.10(c) while limited etching did occur for the similar area (30-second etch) shown in Fig. 5.10(b) is unknown. Fig. 5.10(d) shows that the 160 nm grating period at the perimeter of the same device is well defined. It is assumed that result in Fig. 5.10(c) was due to a defect in the patterned HSQ occurring during the lithography step. Fig. 5.11 is a continuation of the same process.

The results of Fig. 5.11(a) and (b) show the effects of again doubling the etch time to 120 seconds for the same process. The resulting etch depth for 320 nm grating periods is approximately 130 nm while the etch depth for 160 nm grating periods is approximately 80 nm. The exposure dose for the HSQ mask of Figures 5.11(a) and (b) was similar - $440\mu\text{C}/\text{cm}^2$ (5% higher) to that of the patterns shown in Fig. 5.10. The results of Figures 5.11(c) and (d) were obtained after a 180-second etch with the same process parameters. The exposure-dose for the HSQ pattern was $600\mu\text{C}/\text{cm}^2$ (generally overexposed,) however the HSQ pattern was well defined near the edges of the device for etch characterization purposes. The results show that after some initial etching, a threshold is reached where the etch rate rapidly accelerates. By increasing the etch time by 50%, the resulting etch depth increased by approximately 500%. The resulting grating lines have an approximate 10:1 aspect ratio which is an excellent result, although much deeper than the gratings required for the GMR-SEL devices designed for this work.

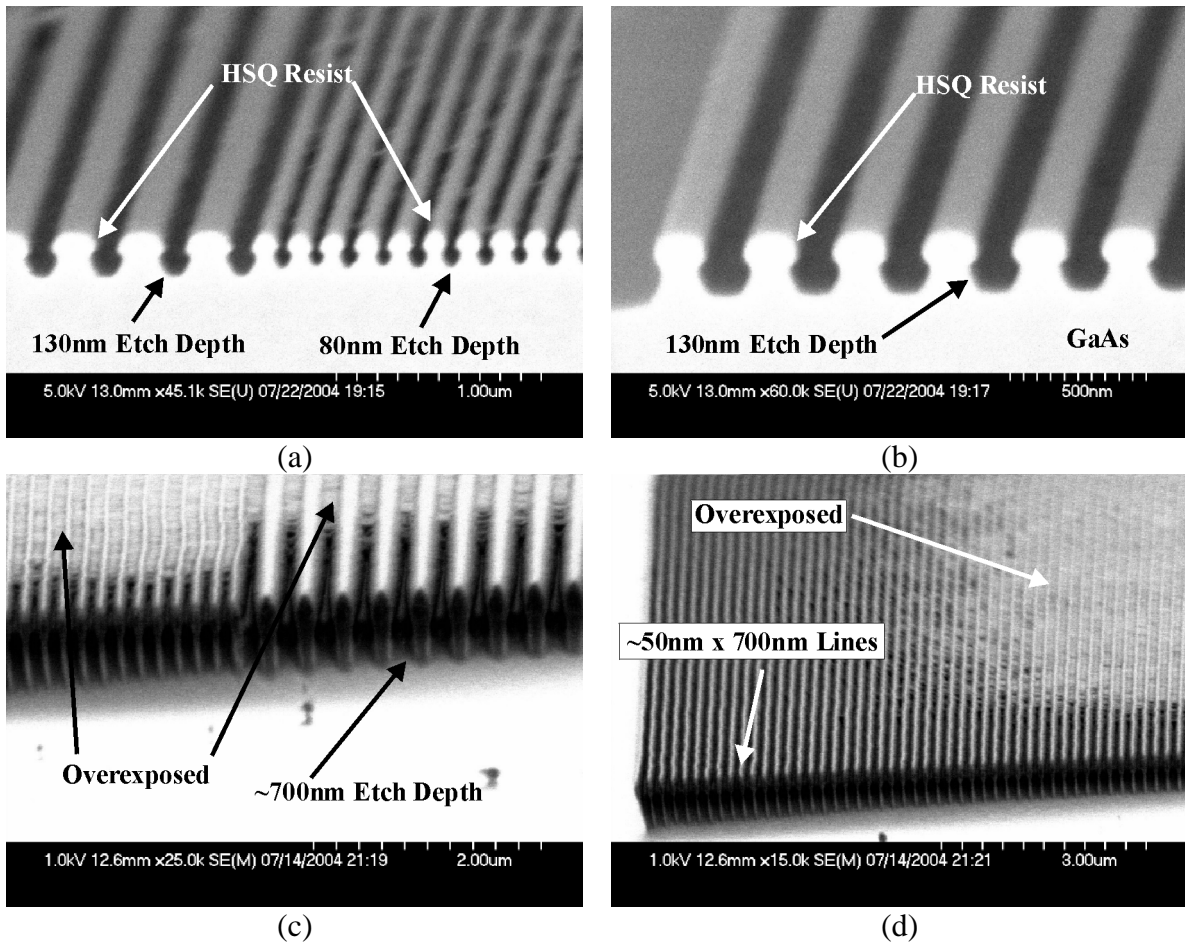


Figure 5.11. SEM micrographs of RIE-etched GaAs grating depth as functions of etch time. The pattern exposure dose for (a) and (b) was $440\mu\text{C}/\text{cm}^2$. This pattern was etched for 120 seconds showing an approximate 130 nm etch depth. (c) and (d) were etched for 180 seconds showing an approximate 700 nm etch depth. The exposure dose for this device was $600\mu\text{C}/\text{cm}^2$.

The results of Figures 5.10 and 5.11 indicate that the physical conditions in the etch chamber are changing during the initial etching; when the system stabilizes, the etch process chemistry becomes optimized and etching proceeds at a constant rate. The results also indicate that the initial etching is somewhat isotropic while the stabilized etching becomes anisotropic. These results clearly exemplify the need for thorough and rigorous process characterization for any given etch system and process.

5.12 Summary of Electron-Beam Patterning and RIE Etching of Sub-Micron Grating Structures on GaAs

This work has described the process development and characterization for patterning sub-micron grating structures in GaAs by electron-beam lithography and reactive ion etching. The results from the electron-beam lithographic patterning indicate that the fractured proximity-effect-corrected patterns used unoptimized exposure-dose assignment. The result is that the exposure dose range for proximity-corrected patterns was too large causing incorrect exposure at either the center or edges of the grating pattern. Additionally, patterning is best performed immediately after full electron-beam lithography system calibration.

The RIE-etching results indicate that the etch rate is non-linear with time and substrate material. The observed threshold in etch rate could be determined accurately by use of HSQ mask patterns with uniform line widths and clearing between the patterned grating lines. One primary source of optimization would be obtained by refinement of the HSQ mask pattern quality before RIE etching. The patterns used for etching the final GMR-SEL wafer had non-uniform grating line widths and poor groove clearing between central and peripheral areas of each device. The poor clearing between grating lines resulted in roughness of the final etched grating structures. For sub-micron grating devices, this roughness will result in increased scattering losses from the device.

In summary, although not completely optimized, the results indicate that the methods presented here are suitable for fabrication the grating structures required for the GMR-SEL devices described in previous chapters.

CHAPTER 6

FABRICATION OF GUIDED-MODE RESONANCE SURFACE-EMITTING LASERS BY ELECTRON-BEAM LITHOGRAPHY, REACTIVE ION ETCHING, AND TESTING

Fabrication of guided-mode resonance surface-emitting lasers (GMR-SEL) based on the designs of Chapter 4 begins with crystal growth of the desired layer structure on high-quality substrates [12]. The GaAs/AlGaAs material system using an $\text{In}_{0.2}\text{Ga}_{0.8}\text{As}$ strained quantum well region for light emission near 980 nm was employed for this work. For the fabricated prototype devices, a simplified GMR-SEL design using optical excitation (pumping) of the quantum-well light-emitting layers was selected. Crystal growth was by molecular beam epitaxy (MBE).

Fabrication steps for the GMR-SEL devices included wafer material characterization followed by refinement of the GMR grating design parameters described in Chapter 3. All post-wafer-growth output wavelength tunability was through variation of the grating parameters including period, depth, and fill factor. Subsequent fabrication steps included lithographic definition of the grating patterns and etch-transfer of the grating pattern into the GMR waveguide-grating layers. In this work, the electron-beam lithography process described in Chapter 5 was used to define different GMR device sizes and shapes as well as devices incorporating both first and second-order grating periods.

The GMR-SEL grating patterns were exposed in Hydrogen-Silsesquioxane (HSQ) resist yielding a SiO₂-like hard-mask layer for reactive-ion-etching (RIE) [73]. Due to the non-linear resist exposure characteristic, the GMR-SEL device patterns required proximity-effect correction to better equalize the electron-beam exposure dose between the centers and perimeters of the grating patterns [86, 87]. The exposed HSQ grating patterns were transferred into the top GMR-SEL wafer layers using the RIE process described in Chapter 5 with the parameters given by Table 5.1. Finally, GMR-SEL output characterization was performed by resonant optical pumping and spectroscopic analysis.

6.1 Electron-Beam Patterning of GMR-SEL Grating Structures

The results of the HSQ electron-beam exposure-dose characterization and RIE-etch process development described in Chapter 5 were applied to devices patterned on the GMR-SEL Wafer #2. Six different proximity-corrected device patterns for prototype GMR-SEL lasers were grouped into 1cm² 13-element arrays for the patterning of Wafer #2. A description of the different device patterns is given in Table 6.1.

Device pattern Types #1 and #4 were single-field devices. Pattern Type #1 was a simple uniform 320 nm grating period and Type #4 was the pattern of Fig. 5.1 having first-order 160 nm-period gratings at each end of a uniform 320 nm-period grating region. Device pattern Types #2, #3, #5, and #6 were larger multiple-field devices requiring stepped-wafer patterning to define the full device. These devices were fabricated devices for testing purposes despite the possibility of significant stitch error at the time of

Table 6.1. Device pattern types for patterning of prototype GMR-SEL Devices.

Device Type	Device Size	Structure Comments
Type #1	300 μm x 300 μm	Uniform 320 nm Grating Period (730 periods)
Type #2	300 μm x 600 μm	Uniform 320 nm Grating Period (1460 periods)
Type #3	600 μm x 600 μm	Uniform 320 nm Grating Period (1460 periods)
Type #4	300 μm x 300 μm	Pattern of Figure 5.1
Type #5	300 μm x 600 μm	Two End-aligned patterns of Figure 5.1
Type #6	300 μm x 270 μm	Pattern of 5.7 with only 1 section of 160 nm period

patterning. Two series of these 13-element pattern groups were defined with varying exposure doses. Each 13-element array was patterned with the same exposure dose.

The 13-device array pattern layout is shown in Fig. 6.1. Six of the devices in each array were pattern Type #1, two devices each of pattern Types #2 and #3, and single patterns of the remaining types. Wafer #2 was patterned with 20 sets of these 13-element arrays with exposure doses ranging between 400 $\mu\text{C}/\text{cm}^2$ and 460 $\mu\text{C}/\text{cm}^2$ and two scaling factors. A set of 13, 100% scale-factor 13-element arrays was first patterned, followed by a set of 7 arrays with a 99% scaling factor. The 320 nm grating design period for the majority of devices corresponds to the 1000 nm photoluminescence peak for Wafer #2 described in the previous chapter. The 99% scaling resulted in a patterned grating period of 317 nm to demonstrate resonant wavelength dependence on the grating parameters of the GMR-SEL laser structure. Pattern scaling for the Leica VB-6 E-Beam lithography system is implemented with a simple run-time software command.

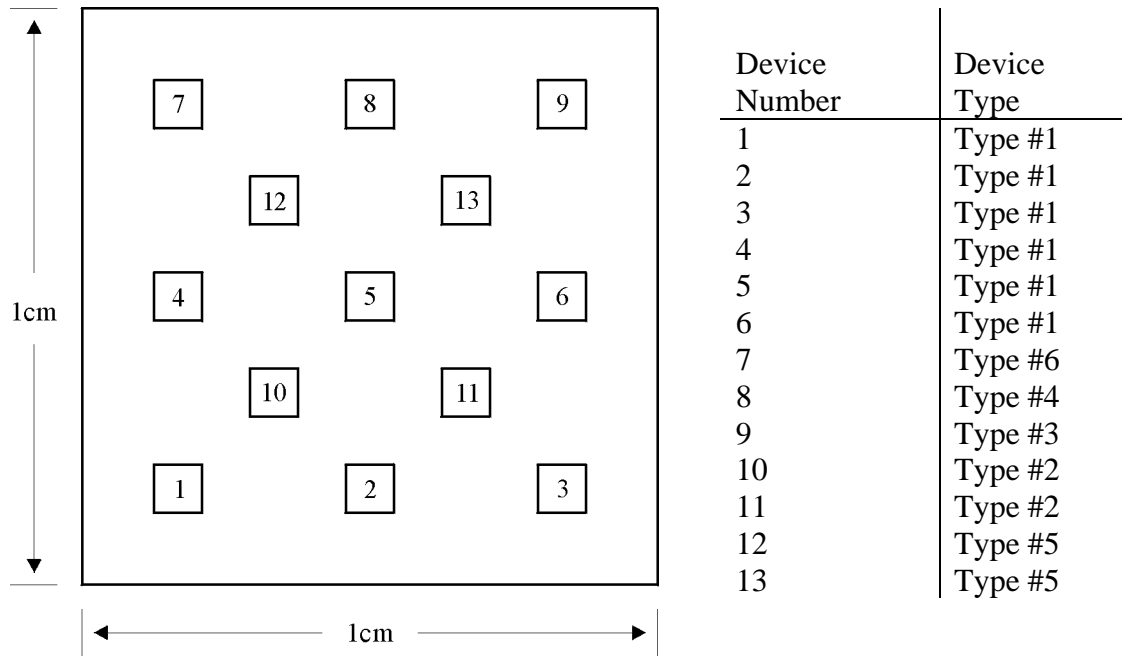


Figure 6.1. Schematic of layout for electron-beam patterning of GMR-SEL devices. Each 1cm^2 layout was comprised of 13 device patterns. The specific pattern for each device is given in the legend and described in Table 6.1.

6.2 RIE Etching of GMR-SEL Grating Structures

After electron-beam exposure, the devices were developed and RIE-etched using the parameters of Table 5.1. RIE etching was performed on each 13-element array with etch times ranging between 30 and 90 seconds. Two of the resulting RIE-etched GMR-SEL structures are shown in Fig. 6.2. The exposure doses for 6.2(a) and (b) were $400\mu\text{C}/\text{cm}^2$ and $460\mu\text{C}/\text{cm}^2$ respectively. The figures clearly show the GMR-SEL laser wafer structure including the upper and lower waveguide-gratings and quantum-well regions. The results show that the final etched-layer depth is well above the quantum-well region indicating that etch-damage to the light-emitting layers should be minimal.

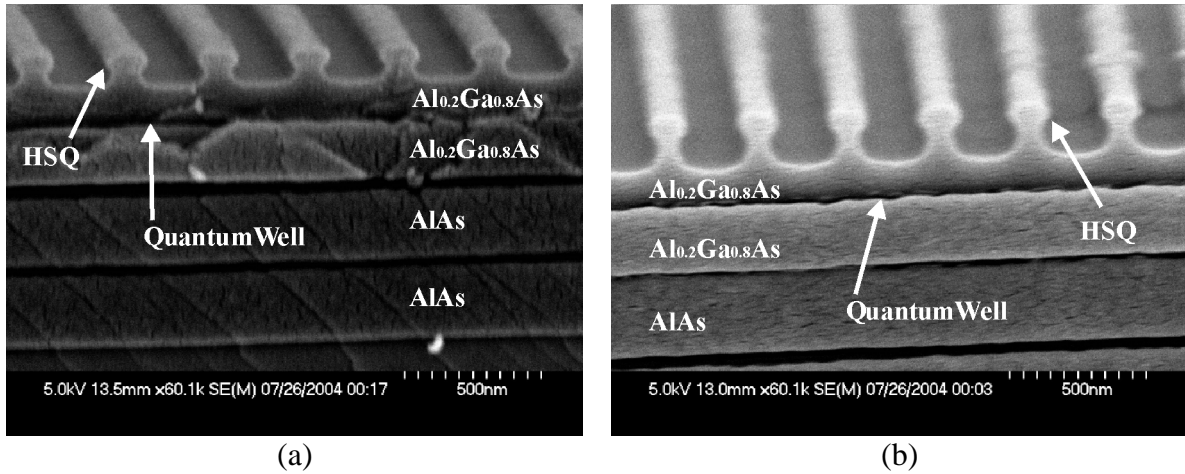


Figure 6.2. SEM micrographs of RIE etched GMR-SEL gratings structures. (a) Etched GMR grating after 30-second etch. Etch depth is approximately 70 nm for the $400\mu\text{C}/\text{cm}^2$ HSQ mask exposure. (b) Etched GMR grating after 90 second etch. Etch depth is approximately 120 nm for the $460\mu\text{C}/\text{cm}^2$ HSQ mask exposure.

The final etched devices of Fig. 6.2 exhibit significant isotropic etching of the $\text{Al}_{0.2}\text{Ga}_{0.8}\text{As}$ top waveguide and GaAs cap layers. The results indicate that the RIE-etching characteristics for $\text{Al}_{0.2}\text{Ga}_{0.8}\text{As}$ differ from those of the plain GaAs substrates. In addition to isotropic etching, the etch rate was slightly higher for $\text{Al}_{0.2}\text{Ga}_{0.8}\text{As}$ than for GaAs . The isotropic etching also resulted in significant HSQ mask undercutting and reduced grating line widths and fill factors. The proximity-corrected patterns used for patterning of the GMR-SEL laser wafer also suffered from the un-optimized fracturing and dose assignments described in section 5.9. The resulting devices exhibited non-uniform line widths and etch depths near the perimeter of the devices. Additionally, the non-optimized pattern fracturing resulted in a high degree of dose-error near stitch boundaries of the multi-field devices.

The stepped-pattern areas were clearly visible under an optical microscope for all devices with multi-field patterns. From the results of section 5.10, the exposed HSQ

grating fill factors were typically 40% which were less than the 62.5% design value. The resulting final grating fill factors for all fabricated structures were approximately 20% to 25% in the uniform central areas of the devices. The measured grating periods were 319 nm.

6.3 GMR-SEL Laser Test Setup

The setup of Fig. 6.3 was used for testing of the fabricated GMR-SEL devices. This setup provided for resonant pumping of the GMR devices near the 45 degree incident resonant pump angle with wavelengths in the range of 740 nm to 840 nm as described in Chapter 4. To allow high-intensity pumping, the output of the Ti:Sapphire

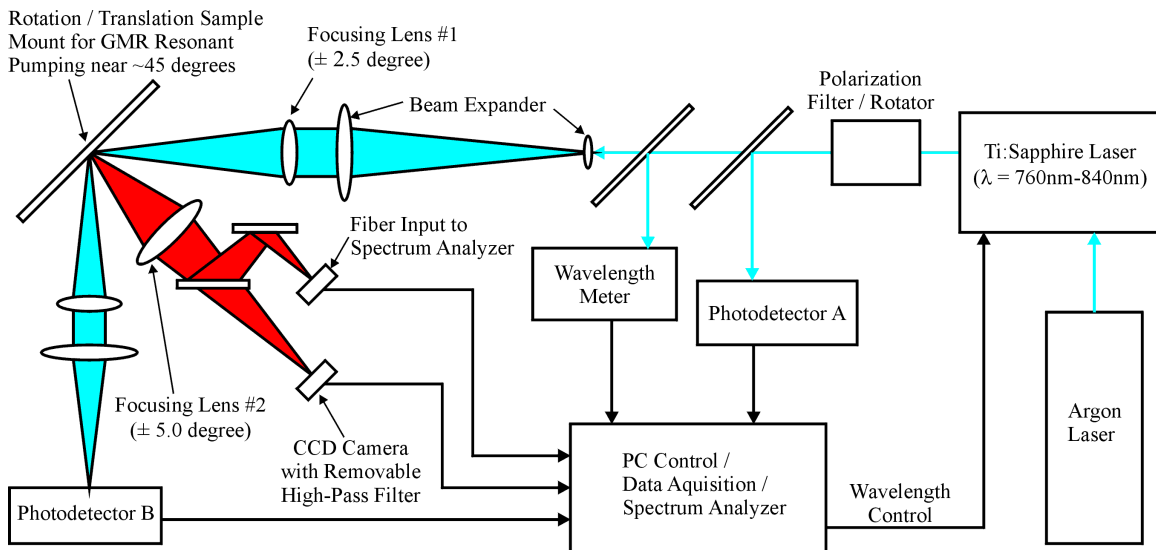


Figure 6.3. Schematic of GMR-SEL laser test setup. PC control is provided for all data acquisition and wavelength control. The sample mount is configured to provide angular adjustment of the incident pump angle as also translational positioning of the wafer samples to allow pumping of individual devices. The photodetectors are provided to allow normalization of the pump and reflected beam intensities due to variation in output power from the Ti:Sapphire laser at different wavelengths.

laser was first expanded and refocused on the GMR-SEL sample. The pump-beam intensity was monitored under computer control to allow normalization of the GMR pump intensity (the Ti:Sapphire output power varies with output wavelength tuning.) The reflected beam intensity was monitored to insure pumping at the device resonance wavelength.

A CCD camera was used to observe the location of the pump-beam spot relative to the GMR grating structures. The CCD camera element is sensitive to both the pump wavelength as well as the photoluminescence near 980 nm from the GMR-SEL sample. A removable high-pass filter was placed between the focusing lens and the CCD camera element by using a simple double-side-polished GaAs wafer. The GaAs bandgap occurs at approximately 870 nm with high transparency for the longer wavelengths near 980 nm. This allowed viewing of the GMR-SEL sample with low-level visible light during translational alignment with the pump beam, then viewing through the high-pass filter to allow visualization of the emitted photoluminescence only.

6.4 GMR-SEL Laser Test Results

The fabricated GMR-SEL devices were mounted in the setup of Fig. 6.3 for testing. Samples were pumped at the GMR resonance angle and wavelength near 810 nm. For testing of each device, the incidence angle was set, and the Ti:Sapphire output wavelength was varied slightly to maximize the photoluminescence (PL) from the device. The incident pump illumination was approximately $50\text{W}/\text{cm}^2$. For all devices fabricated from GMR-SEL Wafer #2, strong photoluminescence was observed confirming that the quantum-well light emitting layers were undamaged from the RIE etching process. Due

to coupling losses into the optical spectrum analyzer, the absolute photoluminescence intensity was not measured.

Typical photoluminescence curves obtained from the GMR-SEL devices are shown in Fig. 6.4. The measured photoluminescence peak for all measure devices under resonant pumping conditions was in the range of 1005 nm to 1020 nm. It was found that the photoluminescence peak shifted toward longer wavelengths with increasing measurement (pumping) time. Additionally, the relative strength of the photoluminescence tended to decrease with measurement time. These characteristics are attributed to device heating under the high-power pump illumination.

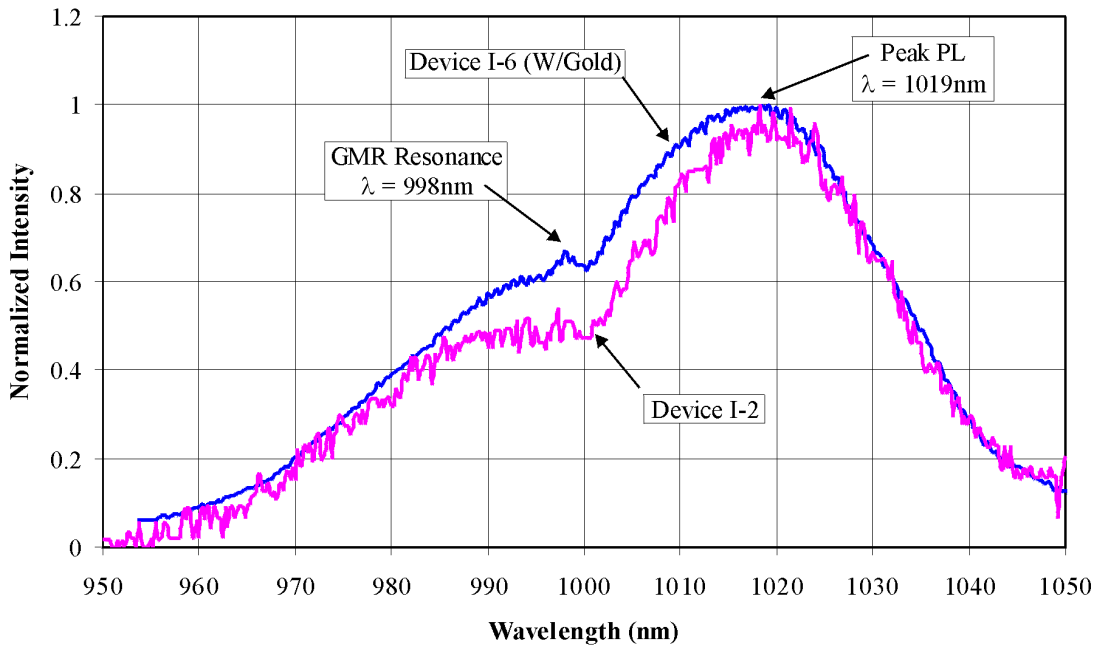
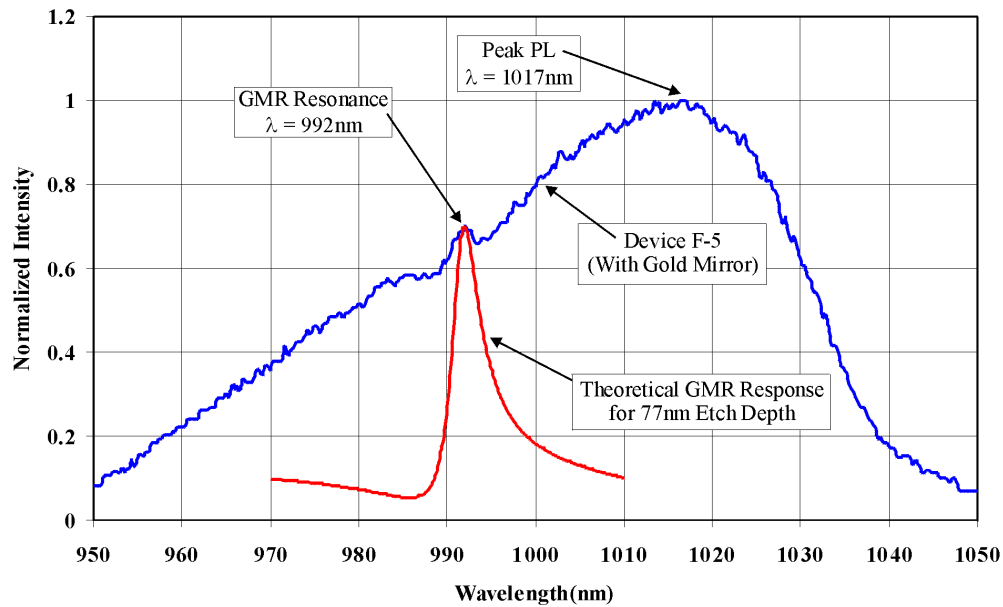


Figure 6.4. Graph of typical normalized photoluminescence (PL) obtained from GMR-SEL wafer devices. Device I-2 shows a dip in the photoluminescence curve near the resonance wavelength of the GMR waveguide-grating. Device I-6 shows a small peak that often appeared in the photoluminescence curve at the GMR resonance wavelength when the bottom substrate surface was coated with a thick-layer gold mirror.

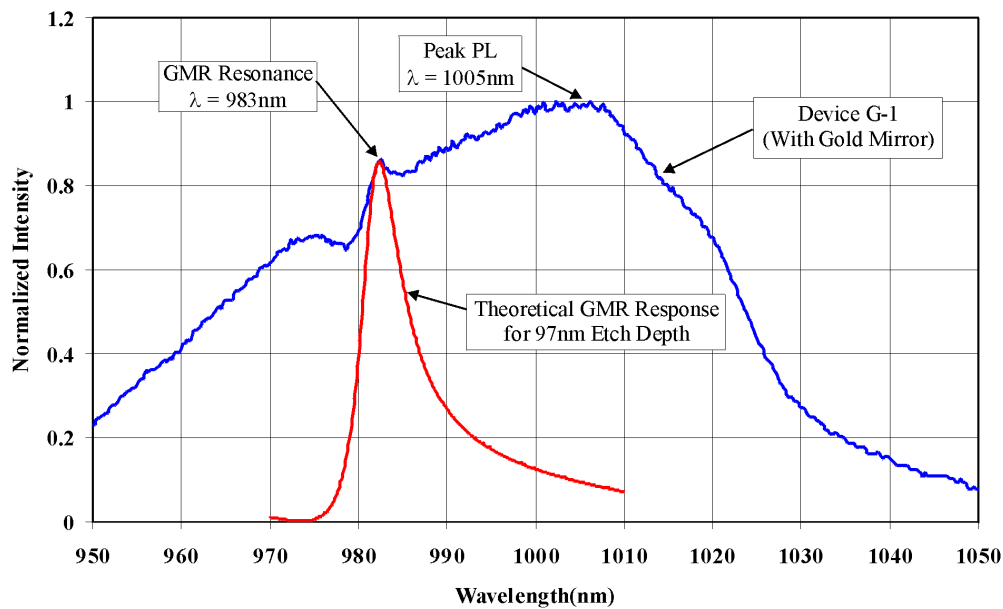
The photoluminescence curves of Fig. 6.4 are normalized to show the change in the shape of the PL curves when a thick-film gold mirror is added to the bottom surface of the substrate. Without the mirror, a flat area in the photoluminescence (PL) curve for Device I-2 occurs near the GMR resonance wavelength. The PL curve for Device I-6 shows the effect of adding a thick-layer gold mirror. The emitted PL intensity is enhanced (approximately by a factor of 2 due to the Gold mirror,) and often a small peak appeared in the PL curve at the GMR resonance wavelength.

This peak indicates that device I-6 is exhibiting super-luminescent spontaneous emission just below the threshold of lasing. The strained quantum well behaves as an inhomogeneously broadened gain medium that exhibits the effects of “spectral hole burning” [90] due to coupling of energy into the GMR resonance mode. As the number of stimulated photon transitions increases in the GMR resonator mode, the gain (PL) at adjacent wavelengths is depleted. The results indicate that GMR-SEL lasing would likely occur if the GMR resonator mode coincided with the peak photoluminescence gain, thus allowing additional gain in the resonator mode.

Two additional photoluminescence curves are shown in Fig. 6.5 where the spectral hole burning effect is more pronounced. Each device has a deposited gold mirror on the backside of the substrate. The curves show the measured variation of the PL peak wavelengths, as well as the effect of GMR waveguide-grating coupling efficiency. The difference in the peak PL wavelengths is attributed to variation in the quantum-well layer thicknesses near the edges of Wafer #2, as well as slightly different optical pumping



(a)



(b)

Figure 6.5. Graph of measured normalized photoluminescence (PL) versus wavelength obtained from GMR-SEL wafer devices F-5 and G-1 with gold substrate mirrors. (a) The HSQ exposure dose was $420\mu\text{C}/\text{cm}^2$ with a 60-second etch time. The theoretical GMR response curve corresponds to a 77 nm etch depth. (b) The HSQ exposure dose was $440\mu\text{C}/\text{cm}^2$ with a 75-second etch time. The theoretical GMR response curve corresponds to a 97 nm etch depth.

conditions during measurement of the two devices. Again, a shift toward longer wavelengths occurred for devices illuminated for long periods during data recording.

For a measured grating period of 319 nm and estimated 25% average fill factor for each device, the GMR resonance peaks were calculated to occur for etched grating depths of 77 nm for Device F-5 and 97 nm for Device G-1. These etch depths correlate closely with the measured RIE etch rate and time for processing of Wafer #2 and illustrated in Fig. 6.2. The deeper grating of Device G-1 results in increased coupling between the GMR guided modes, thus this device exhibits increased spectral hole burning.

This increased coupling results in both a shift in the resonant wavelength toward shorter wavelengths from that of device F-5 as well as increased coupling into the GMR resonator mode. The increased coupling into the GMR resonant mode reduces the resonator losses and produces a larger spectral hole burning effect. In both cases, for the curves of Fig. 6.5, there is still insufficient gain at the GMR resonant wavelengths to achieve lasing.

6.5 GMR-SEL Laser Fabrication Results Summary

This work has described the process development and characterization for fabrication of prototype GMR-SEL laser devices by electron-beam lithography and reactive ion etching. The prototype GMR-SEL laser devices fabricated in this work did not exhibit the single-wavelength operating characteristic of lasing modes. Nevertheless, there appear clear peaks in the PL spectra precisely where GMR resonances are predicted to appear by numerical simulation using the experimental values for the parameters. The

Wafer #2 layer structure (substrate spacer layer thickness) was designed based on a 980 nm peak quantum-well gain wavelength. The combination of a 20 nm minimum difference between the peak gain wavelength and GMR resonator mode wavelengths, combined with a 40 nm difference between the peak gain wavelength and the GMR layer design wavelength resulted in highly un-optimized devices that did not achieve lasing. The results do indicate that lasing could be achieved by further optimizing the device structure.

Optimization steps would include tailoring of the GMR grating parameters to better match the photoluminescence gain peak and by providing more gain near the GMR resonator wavelength by including additional strained quantum-well layers into the basic wafer structure. One additional source of device optimization would be obtained by refinement of the HSQ mask pattern quality before RIE etching. The patterns used for etching the final GMR-SEL wafer had non-uniform grating line widths and poor groove clearing between central and peripheral areas of each device. The poor clearing between grating lines resulted in roughness of the final etched grating structures. This roughness results in increased scattering losses from the GMR resonator mode, thus requiring increased gain to achieve the threshold of lasing.

The results of the RIE-etch process development indicate that the process should be optimized on the $\text{Al}_{0.2}\text{Ga}_{0.8}\text{As}$ layers similar to those used in the GMR-SEL wafer structure. The RIE-etching results indicate that the etch rate is non-linear with time and substrate material. The observed threshold in etch rate could be determined accurately by

use of HSQ mask patterns with uniform line widths and clearing between the patterned grating lines.

The results from the electron-beam lithographic patterning indicate that the fractured proximity-effect-corrected patterns used unoptimized exposure dose assignment. The net effect is that the exposure dose range for the proximity-corrected patterns was too large causing incorrect exposure at either the center or edges of the grating pattern. Additionally, e-beam patterning would best performed immediately after full electron-beam lithography system calibration. In summary, guided-mode resonance surface emitting laser (GMR-SEL) operation was not achieved in this research, but the essential processing requirements and baseline parameters have been developed for future work in this area.

CHAPTER 7

CONCLUSIONS

In this dissertation, practical design and fabrication methods of guided-mode resonance surface-emitting lasers (GMR-SELs) have been presented. The main contributions toward realization of these devices are summarized below.

- (1) The design and fabrication of lasers using guided-mode resonance (GMR) structures has been studied both theoretically and experimentally. By extending the results of previous experimental work using GMR mirrors as output couplers in dye and Ti:Sapphire laser cavities, the feasibility of integrating GMR mirrors into semiconductor cavities has been investigated. The practical aspects of design and fabrication of semiconductor-based GMR surface-emitting lasers have been analyzed. These include design, analysis and fabrication of the required gratings in the GaAs / AlGaAs material system.
- (2) A numerical analysis tool based on modifications to the standard implementation of rigorous coupled-wave analysis (RCWA) was developed to study the electric fields in GMR structures. The fields analysis allows visualization of standing wave patterns as well as temporal variations in the fields under steady-state conditions. The numerical analysis provides rigorous

solution of both propagating and evanescent diffracted orders yielding simulation results similar to those obtained by finite difference time domain (FDTD) or finite-element method (FEM) analysis under steady-state conditions. The modified RCWA analysis method is highly efficient compared to the FDTD or FEM methods when applied to periodic structures. This numerical analysis formulation is a key tool necessary for the design of GMR-SEL structures presented in this work.

- (3) High-quality sub-micron diffraction gratings are a critical component of GMR devices. An optimized two-beam interferometer for ultra-violet (UV) exposure of photoresist gratings was designed and implemented. The interferometer system is rapidly reconfigurable for the fabrication of high-quality uniform large-area photoresist grating structures. The interferometer system employs a simple but effective CCD camera-based fringe stabilization system.
- (4) A simple CCD-based fringe stabilization system using commercial off-the-shelf (COTS) components was designed and implemented for fabrication of high-quality photoresist gratings. This system provides fringe stabilization better than $1/100^{\text{th}}$ of a fringe by analysis of the video frame data from a CCD camera element. Projected fringe pattern data is acquired under computer control. A single line of the video data is extracted from the data and then filtered in the spatial frequency domain to obtain accurate fringe position information. The fringe control system is designed specifically to operate in

the presence of high-frequency spatial intensity noise including laser speckle noise and intensity variations due to defects in the optical components. The filtered fringe data is compared with data obtained in subsequent video frames to issue an error control signal to a piezo-electric positioner that corrects any measured fringe movement. This fringe stabilization system is a key component for fabrication of the photoresist gratings presented in this work as well as in related work by other researchers.

- (5) The requirements for practical fabrication of photoresist gratings on various substrates including those with high-reflectivity masking layers were investigated. These requirements included the use of thin-film analysis and proper utilization of bottom anti-reflection coatings (BARC). The results of this study as well as practical limitations in the fabrication of high-quality photoresist gratings were demonstrated
- (6) The practical limitations for fabricating high-quality photoresist gratings were considered in the design of GMR-SEL grating structures. These include resulting grating profiles and characteristics when the grating patterns are transferred into underlying substrate layers by both wet and dry etching. Wet-etching of semiconductor substrates presents finite limits on the depth and aspect ratio of the resulting structures. It was demonstrated by RCWA analysis that virtually any grating profile can be employed in GMR-SEL structures if properly considered during the design phase.

- (7) The practical design and characterization of GMR-SEL wafers was presented. This included simple estimates for initial design followed by RCWA field analysis to optimize the laser wafer thicknesses. The design procedure was applied to an optically-pumped GMR-SEL device that also employs the GMR resonance effect for optical pumping. The design was performed for a GaAs / AlGaAs laser structure using an $\text{In}_{0.2}\text{Ga}_{0.8}\text{As}$ strained-layer quantum-well for surface-normal light emission near 980 nm. The GMR-SEL structure is optically pumped with an 810 nm input beam at an approximate 45° oblique angle. The GMR-SEL design included variation of parameters to insure operation over a wide range of grating parameters.
- (8) The results of wafer characterization by photoluminescence measurements were used to optimize the grating parameters before fabrication of the GMR-SEL devices. The catastrophic defects that appeared on the initial grown wafer verified the limitations of growing thick layers of AlAs on GaAs substrates. By including thin GaAs layers during the growth of the thick AlAs layer, strain is reduced resulting in a high-quality wafer structure. By using numerical simulations to calculate the proper positioning of the thin GaAs layers at nulls of the laser cavity standing wave, the GMR-SEL characteristics are essentially unchanged.
- (9) A process for fabricating sub-micron gratings for GMR-SELs on GaAs by electron-beam lithography was developed. The resist material used for this work was hydrogen-silsesquioxane (HSQ) which results in a directly

patterned SiO₂-like etch mask after e-beam exposure and development. This work is among the first reports of the HSQ patterning of uniform grating structures with dense lines and spaces similar to DFB / DBR lasers on GaAs.

- (10) The HSQ resist gratings were used as an etch mask for RIE transfer of 320 nm and 160 nm grating periods into GaAs substrates. A consistent RIE process was developed by systematic variation of etch parameters. It was demonstrated that the RIE etching process could overcome minor HSQ mask overexposure (due to electron-beam proximity effects) to yield predictable GaAs grating features.
- (11) Experimental results indicated that the RIE-etch process was non-linear in time, and could be utilized to fabricate grating lines and spaces with high aspect ratios. Although not applicable to the GMR-SEL structures of this work, dense 50 nm grating lines with approximately 15:1 (50 nm x 700 nm) aspect ratios were fabricated in GaAs substrates. These results indicate that the HSQ and RIE processing presented in this work is applicable to other work on GaAs-based optoelectronic devices such as photonic crystal structures.
- (12) The fabricated GMR-SEL devices were characterized by optical pumping at oblique angles of incidence near 45° with a Ti:Sapphire laser operating near 810 nm. The specific pump wavelengths satisfied one of the two (reflection or transmission) resonance conditions for the given angle of incidence. The GMR-SEL devices did not achieve lasing either with or without a deposited gold mirror on the backside of the substrate. The results indicate that the

devices with gold mirror demonstrated the spectral hole burning effects that occur just below the threshold of lasing.

- (13) From the measured results of Chapter 6, there appear clear peaks in the PL spectra precisely where GMR resonances are predicted to appear by numerical simulation using the experimental values for the parameters. Therefore, the results indicate that with device optimization, the GMR-SEL devices can achieve lasing threshold.

Based on results of this research, future theoretical and experimental work on GMR-SEL devices will be directed toward proof-of-concept demonstration of optically-pumped as well as electrically injected laser devices. The primary steps toward this goal are outlined below.

- (1) Repeat the experimental procedures outlined in this work with a laser wafer structure employing a multiple quantum-well active region. This will allow increased gain thus increasing the light intensity in the cavity resonant mode to produce monochromatic light output above the lasing threshold.
- (2) Repeat the experimental procedures outlined in this work with a laser wafer structure having an integrated multi-layer Bragg mirror between the substrate and AlAs spacer / cladding layer. This will allow higher reflection with lower optical loss than the deposited metal mirror.
- (3) Repeat the experimental electron-beam lithography processing with optimized proximity-effect corrected patterns. This will allow definition of uniform

grating structures over the entire device as well as the patterning of multiple-field devices with stitch errors dependent only on the misalignment of the fields. This stitch error can be typically be minimized through rigorous system calibration.

- (4) Perform optimization of the RIE processing on both GaAs and $\text{Al}_x\text{Ga}_{1-x}\text{As}$ using uniform and well-defined patterns. In this way, the etch rate dependence on feature size and pattern density can be better quantified. This would allow consistent and repeatable patterning of sub-micron grating features for both uniform gratings and devices employing grating structures with multiple periods.
- (5) Perform MBE regrowth of GaAs / $\text{Al}_x\text{Ga}_{1-x}\text{As}$ grating structure as a key step in fabricating electrically injected GMR-SEL devices. This step must be accomplished successfully to maintain the single-crystal layer structure necessary to both minimize optical scattering from the waveguide / grating region as well as provide the means for electrical current injection through the waveguide-grating layers.
- (6) Explore the use of other material systems for the fabrication of GMR-SEL devices. This research may allow fabrication of devices with operating wavelengths at the $1.3\mu\text{m}$ and $1.55\mu\text{m}$ wavelengths employed in telecommunications devices. The material systems would include the quaternary $\text{Ga}_x\text{In}_{1-x}\text{As}_y\text{P}_{1-y}$ and $\text{In}_{1-x-y}\text{Al}_x\text{Ga}_y\text{As}$ lattice matched to InP substrates.

- (7) New theoretical work should include the incorporation of an optical gain model into the rigorous coupled-wave analysis. This combined with recent work on RCWA for finite structures would allow theoretical modeling of a full GMR-SEL structure. The current piecewise modeling typically assumes that the various layers have no gain or loss at resonance.
- (8) Perform an advanced ray tracing simulation to determine the practical requirements for using GMR mirrors as the tuning element for Ti:Sapphire lasers. This is necessary to determine the useful operating wavelength range as a function of the dielectric coatings required as well as the quality of the optical and mechanical components.

In summary, this work has demonstrated fundamental methods for design, fabrication, and analysis of an optically-pumped guided-mode resonance surface-emitting laser. This work provides a solid foundation for future work on these devices.

APPENDIX A

**MATCAD IMPLEMENTATION OF 3-LAYER ASYMMETRICAL
WAVEGUIDE ANALYSIS ROUTINE**

Analysis Routine to Determine 3-Layer Asymmetric Slab Waveguide Characteristics

This analysis is adapted from [Kogelnik and Ramaswamy [1], 1974]

Define Refractive Indices:

Cover: (Air) $n_c := 1$

Waveguide (Al_{0.2}Ga_{0.8}As): $n_f := 3.397$

Substrate (GaAs): $n_s := 2.96$

Define Operating Wavelength: $\lambda := 0.985 \cdot 10^{-6}$

Define Propagation Constant: $k := \frac{2 \cdot \pi}{\lambda}$ $k = 6.379 \times 10^6$

Define TE Asymmetry Parameter: $a_{TE} := \frac{n_s^2 - n_c^2}{n_f^2 - n_s^2}$ $a_{TE} = 2.794$

Define TM Asymmetry Parameter: $a_{TM} := \frac{n_f^4}{n_c^4} \cdot a_{TE}$ $a_{TM} = 372.049$

Define Normalized Cutoff Frequency for Fundamental Mode: $V_o := \text{atan}(a_{TE})$ $V_o = 1.227$

Define Mode m: $m := 1$

Define Normalized Frequency for Mode m: $V_m := V_o + m \cdot \pi$ $V_m = 4.369$

Define Initial Seed Value for Normalized Guide Index: $b := 0.1$

Set asymmetry parameter a for TE analysis: $a := a_{TE}$

Define Normalized Dispersion Relation and solve for m = 1 order: (For TE Mode)

$$b_p(V_m, m) := \text{root} \left[\left(m \cdot \pi + \text{atan} \left(\frac{\sqrt{b}}{\sqrt{1-b}} \right) + \text{atan} \left(\frac{\sqrt{b+a}}{\sqrt{1-b}} \right) - V_m \cdot \sqrt{1-b} \right), b \right]$$

$b_{ww} := b_p(V_m, 1)$ $b = 0.021$

Solve for Normalized Waveguide Index:

$N_{ww} := \sqrt{b \cdot (n_f^2 - n_s^2) + n_s^2}$ $N = 2.97$

Solve for Transverse Propagation Constant:	$\kappa := \sqrt{k^2 \cdot (n_f^2 - N^2)}$	$\kappa = 1.052 \times 10^7$
Solve for Mode Propagation Constant:	$\beta := \frac{2 \cdot \pi}{\lambda} \cdot N$	$\beta = 1.894 \times 10^7$
Solve for Mode Propagation Angle:	$\theta := \text{asin}\left(\frac{N}{n_f}\right)$	$\theta = 60.95 \text{ deg}$
Solve for Decay Constants: Substrate:	$\gamma_s := k \cdot \sqrt{N^2 - n_s^2}$	$\gamma_s = 1.526 \times 10^6$
Cover:	$\gamma_c := k \cdot \sqrt{N^2 - n_c^2}$	$\gamma_c = 1.784 \times 10^7$
Solve for Penetration into Substrate:	$x_s := \frac{1}{\gamma_s}$	$x_s = 0.655 (10^{-6})$
Solve for Penetration into Cover:	$x_c := \frac{1}{\gamma_c}$	$x_c = 0.056 (10^{-6})$
Solve for Substrate Phase Shift:	$\phi_s := \text{atan}\left(\frac{\gamma_s}{\kappa}\right)$	$\phi_s = 0.144$
Solve for Cover Phase Shift:	$\phi_c := \text{atan}\left(\frac{\gamma_c}{\kappa}\right)$	$\phi_c = 1.038$
Solve for Shift along Substrate:	$Z_s := \frac{\tan(\theta)}{\gamma_s}$	$Z_s = 1.18 \times 10^{-6}$
Shift along Cover:	$Z_c := \frac{\tan(\theta)}{\gamma_c}$	$Z_c = 1.009 \times 10^{-7}$
(Total shifts are 2 times Z values)		
Calculate Maximum Waveguide Thickness: (for this Mode)	$h := \left(\frac{m \cdot \pi + \phi_s + \phi_c}{\kappa}\right)$	$h = 0.411 (10^{-6})$
Solve for Effective Waveguide Thickness (TE):	$h_{\text{eff}} := h + \gamma_s^{-1} + \gamma_c^{-1}$	$h_{\text{eff}} = 1.122 (10^{-6})$

Note this routine is currently configured to solve for the maximum waveguide thickness for given mode. To solve for above parameters with known waveguide thickness, move the following normalized frequency expressions to the top of this sheet, define h, and solve for b in terms of Vmax.

$$V_{\text{min}} := \frac{2 \cdot h \cdot \pi}{\lambda} \cdot \sqrt{(n_f^2 - n_s^2)} \quad V_{\text{max}} := \text{floor}\left(\frac{V}{\pi}\right)$$

[1] H. Kogelnik and V. Ramaswamy, "Scaling rules for thin-film optical waveguides," *Applied Optics*, vol.13, pp. 1857-1862, Aug. 1974.

REFERENCES

- [1] R. Magnusson, Y. Ding, K. J. Lee, D. Shin, P. S. Priambodo, P. P. Young, and T. A. Maldonado, "Photonic devices enabled by waveguide-mode resonance effects in periodically modulated films," *Proceedings of the SPIE*, vol. 5225, Nano- and Micro-Optics for Information Systems, pp. 20-34, 2003.
- [2] S. Tibuleac and R. Magnusson, "Narrow-linewidth bandpass filters with diffractive thin-film layers," *Optics Letters*, vol. 26, pp. 584-586, May 2001.
- [3] D. Wawro, S. Tibuleac, R. Magnusson, and H. Liu, "Optical fiber endface biosensor based on resonances in dielectric waveguide-gratings," *Proceedings of SPIE*, vol. 3911, Biomedical Diagnostic, Guidance, and Surgical-Assist Systems II, pp. 86-94, 2000.
- [4] P. S. Priambodo, T. A. Maldonado, and R. Magnusson, "Fabrication and characterization of high-quality waveguide-mode resonant optical filters," *Applied Physics Letters*, vol. 83, pp. 3248-3250, Oct. 2003.
- [5] S. Tibuleac, R. Magnusson, T. A. Maldonado, P. P. Young, and T. R. Holzheimer, "Dielectric frequency-selective structures incorporating waveguide-gratings," *IEEE Transactions on Microwave Theory and Techniques*, vol. 48, pp. 553-561, April 2000.
- [6] S. Tibuleac, R. Magnusson, P. P. Young, and T. R. Holzheimer, "Experimental verification of waveguide-mode resonant transmission filters," *IEEE Microwave and Guided Wave Letters*, vol. 9, pp. 19-21, January 1999.
- [7] D. Shin, "Resonance properties of periodic waveguides and their applications," Ph.D. Dissertation, Department of Electrical Engineering, University of Texas at Arlington, Arlington, TX, 2001.
- [8] R. Magnusson, Z. S. Liu, D. Shin, S. Tibuleac, and P. P. Young, "Efficient polarized laser mirror," *Optics & Photonics News*, vol. 9, pp. 35-36, December 1998.
- [9] P. P. Young, Z. S. Liu, S. Tibuleac, and R. Magnusson, "Laser operation with a guided-mode resonance output coupler," *Optical Society of America Annual Meeting, Baltimore, Maryland, October 1998, Conference Proceedings*, p. 127, 1998.

- [10] Z. S. Liu, S. Tibuleac, D. Shin, P. P. Young, and R. Magnusson, "High-efficiency guided-mode resonance laser mirror," Technical Digest of the OSA Topical Meeting on Diffractive Optics and Micro-Optics, post deadline paper, DPDP3.2-DPDP3.4, Kailua-Kona, Hawaii, June 8-11, 1998.
- [11] P. P. Young, Z. S. Liu, S. Tibuleac, D. Shin, and R. Magnusson, "Laser operation with a Guided-Mode Resonance Output coupler," Technical Digest of the OSA Topical Meeting on Diffractive Optics and Micro-Optics, post deadline paper, Kailua-Kona, Hawaii, June 8-11, 1998.
- [12] R. Magnusson, P. P. Young, and D. Shin, "Vertical cavity laser and laser array incorporating guided-mode resonance effects and method for making the same," U.S. Patent 6154480, November 28, 2000.
- [13] S. M. Loktev, V. A. Sychugov, B. A. Usievich, and O. Parriaux, "Anomalous reflection of light in novel distributed-feedback structures," JETP Letters, vol. 65, pp. 320-324, Feb. 1997.
- [14] I. A. Avrutsky and R. Rabady, "Waveguide-grating mirror for large-area semiconductor lasers," Optics Letters, vol. 26, pp. 989-991, July 2001.
- [15] I. A. Avrutsky and R. Rabady, "Experimental characterization of simultaneous spatial and spectral filtering by an optical resonant filter" Optics Letters, vol. 29, pp. 605-607, March 2004.
- [16] J. A. Cox, R. A. Morgan, R. Wilke, and C. Ford, "Guided-mode grating resonant filters for VCSEL applications," Proceedings of the SPIE, vol. 3291, Diffractive and Holographic Device Technologies and Applications V, 1998, pp. 70-76.
- [17] J. A. Cox, R. A. Morgan, and T. Marta, "Mode control in VCSELs using guided-mode resonant filters," Optical Society of America, Trends in Optics and Photonics. Diffractive Optics and Micro-Optics, vol. 41, Technical Digest. Postconference Edition 2000, pp. 57-59, 2000.
- [18] A. Sharon, G. Rosenblatt, A. A. Friesem, H. G. Weber, H. Engel, and R. Steingrueber, "Light modulation with resonant grating-waveguide structures," Optics Letters, vol. 21, pp. 1563-1566, October 1996.
- [19] N. Dudovich, G. Levy-Yurista, A. Sharon, A. A. Friesem, and H. G. Weber, "Active semiconductor-based grating waveguide structures," IEEE Journal of Quantum Electronics, vol. 37, pp. 1030-1039, Aug. 2001.

- [20] T. Kobayashi, Y. Kanamori, and K. Hane, "Surface laser emission from solid polymer dye in a guided mode resonant grating filter structure," *Applied Physics Letters*, vol. 87, pp. 151106-1-2, Oct. 2005.
- [21] T. Kobayashi, Y. Kanamori, and K. Hane, "A surface emitting solid polymer dye laser using a guided mode resonant grating for bio-optical detections," in *IEEE/LEOS Optical MEMs 2005*, pp. 101-102.
- [22] H. Kogelnik and V. Ramaswamy, "Scaling rules for thin-film optical waveguides," *Applied Optics*, vol. 13, pp. 1857-1862, Aug. 1974.
- [23] S. S. Wang, R. Magnusson, J. S. Bagby, and M. G. Moharam, "Guided-mode resonances in planar dielectric-layer diffraction gratings," *Journal of the Optical Society of America*, vol. 8, pp. 1470-1475, August 1990.
- [24] S. S. Wang and R. Magnusson, "Theory and applications of guided-mode resonance filters," *Applied Optics*, vol. 32, pp. 2606-2613, May 1993.
- [25] R. W. Day, S. S. Wang, and R. Magnusson, "Filter-response line shapes of resonant waveguide-gratings," *Journal of Lightwave Technology*, vol. 14, pp. 1815-1824, August 1996.
- [26] S. Tibuleac and R. Magnusson, "Reflective and Transmission guided-mode resonance filters," *Journal of the Optical Society of America A*, vol. 14, pp. 1617-1626, July 1997.
- [27] M. G. Moharam and T. K. Gaylord, "Diffraction analysis of dielectric surface-relief gratings," *Journal of the Optical Society of America*, vol. 72, pp. 1385-1392, Oct. 1982.
- [28] M. G. Moharam, E.B. Grann, D.A. Pommet, and T.K. Gaylord, "Formulation for stable and efficient implementation of the rigorous coupled-wave analysis of binary gratings," *Journal of Optical Society of America A*, vol. 12, pp. 1068-1076, May 1995.
- [29] M. G. Moharam, D. A. Pommet, E. B. Grann, and T. K. Gaylord, "Stable implementation of the rigorous coupled-wave analysis for surface-relief gratings: enhanced transmittance matrix approach," *Journal of Optical Society of America A*, vol. 12, pp. 1077-1086, May 1995.
- [30] R. Tyan, "Design, modeling and characterization of multifunctional diffractive optical elements," Ph.D. Dissertation, Department of Electrical Engineering (applied Physics), University of California, San Diego, San Diego, CA, 1998.

- [31] R. Magnusson at University of Connecticut (private communication), 2003.
- [32] RSoft Design Group, "DiffractMOD," April 2006. [Online]. Available: http://www.rsoftdesign.com/products/component_design/DiffractMOD/
- [33] C. Zimmermann, V. Vuletic, A. Hemmerich, L. Ricci, and T.W. Hansch, "Design for a compact tunable Ti:Sapphire laser," *Optics Letters*, vol. 20, pp. 297-299, Feb. 1995.
- [34] P. P. Young, P. S. Priambodo, T. A. Maldonado, and R. Magnusson, "Simple interferometric fringe stabilization by CCD-based feedback control," presented at the OSA Frontiers in Optics / Laser Science XIX Conference, Tucson, AZ, October 5-9, 2003.
- [35] P. P. Young, P. S. Priambodo T. A. Maldonado, and R. Magnusson, "Simple interferometric fringe stabilization by CCD-based feedback control," Accepted for Publication in *Applied Optics*, 2006.
- [36] P. S. Priambodo, "Theoretical Analysis, Design, Fabrication and Characterization of Dielectric and Nonlinear Guided-Mode Resonance Optical Filters," Ph.D. Dissertation, Department of Electrical Engineering., University of Texas at Arlington, Arlington, TX, 2003.
- [37] P. L. Gourley and M. E. Warren, "Surface-emitting semiconductor laser structures fabricated by microlithography," *Journal of Nonlinear Optical Physics and Materials*, vol. 4, pp. 27-81, Jan. 1995.
- [38] A. Taflove and S. C. Hagness, *Computational electrodynamics: the finite-difference time-domain method*, 3rd ed. Boston: Artech House, 2005.
- [39] I. A. Avrutsky, A. S. Svakhin, and V. A. Sychugov, "Interference phenomena in waveguides with two corrugated boundaries," *Journal of Modern Optics*, vol. 36, pp. 1303-1320, Oct. 1989.
- [40] S. W. Corzine, R. H. Yan, and L. A. Coldren, "Theoretical gain in strained InGaAs/AlGaAs quantum wells including valence-band mixing effects," *Applied Physics Letters*, vol. 57, pp. 2835-2837, Dec. 1990.
- [41] H. Gao, H. Y. Ong, W. J. Fan, and S. F. Yoon, "Analysis of optical gain and threshold current density of 980 nm InGaAs/GaAs compressively strained quantum well lasers," *Computational Materials Science*, vol. 30, pp. 296-302, Aug. 2004.

- [42] S. W. Corzine, R. H. Yan, and L. A. Coldren, "Theoretical gain in strained InGaAs/AlGaAs quantum wells including valence-band mixing effects," *Applied Physics Letters*, vol. 57, pp. 2835-2837, Dec. 1990.
- [43] M. Fallahi, F. Chatenoud, M. Dion, I. Templeton, R. Barber, and J. Thompson, "Circular-grating surface-emitting distributed Bragg reflector lasers on an InGaAs-GaAs structure for 0.98- μm applications," *IEEE Journal of Selected Topics in Quantum Electronics*, vol. 1, pp. 382-386, June 1995.
- [44] S. Y. Hu, D. B. Young, S. W. Corzine, A. C. Gossard, and L. A. Coldren, "High-efficiency and low-threshold InGaAs/AlGaAs quantum-well lasers," *Journal of Applied Physics*, vol. 76, pp. 3932-3934, Sept. 1994.
- [45] W. J. Alford, T. D. Raymond, and A. A. Allerman, "High power and good beam quality at 980 nm from a vertical external-cavity surface-emitting laser," *Journal of the Optical Society of America B (Optical Physics)*, vol. 19, pp. 663-666, April 2002.
- [46] M. Miller, M. Grabherr, R. King, R. Jager, R. Michalzik, and K. J. Ebeling, "Improved output performance of high-power VCSELs," *IEEE Journal of Selected Topics in Quantum Electronics*, vol. 7, pp. 210-216, March-April 2001.
- [47] S. Adachi, "GaAs, AlAs, and Ga $_{1-x}$ Al $_x$ As: Material parameters for use in research and devices applications," *Journal of Applied Physics*, vol. 58, R1-R28, Aug. 1985.
- [48] M. Born and E. Wolf, *Principles of Optics*, 6th ed. Cambridge: Cambridge University Press, 1997, pp. 66-70.
- [49] A. Yariv, *Optical Electronics*, 4th ed. Philadelphia: Saunders College Publishing, 1991, pp. 479-510.
- [50] S. L. Chuang, *Physics of Optoelectronic Devices*, New York: John Wiley & Sons, 1995, pp. 708-711.
- [51] P. G. Snyder, J. A. Woollam, S. A. Alterovitz, and B. Johs, "Modeling Al $_x$ Ga $_{1-x}$ As optical constants as functions of composition," *Journal of Applied Physics*, vol. 68, pp. 5925-5926, Dec. 1990.
- [52] Z. S. Liu, "Design, Fabrication, and Characterization of Guided-Mode Resonance Filters and Waveguide-Grating Couplers," Ph.D. Dissertation, Department of Electrical Engineering, University of Texas at Arlington, Arlington, TX, 1999.
- [53] C. C. Guest and T. K. Gaylord, "Phase stabilization for holographic optical data processing," *Applied Optics*, vol. 24, pp. 2140-2144, July 1985.

- [54] P. Hariharan, B. F. Oreb, and N. Brown, "Real-time holographic interferometry: a microcomputer system for the measurement of vector displacements," *Applied Optics*, vol. 22, pp. 876-880, Mar. 1983.
- [55] G. Saxby, "Fringe Stabilization," *Optical Holography*, Prentice Hall, 1988, pp. 158-159.
- [56] J. Odhner, "Stabilock II® Active Fringe Stabilizer," *Stabilock Application Notes*, 1993.
- [57] R. Lima and L. H. Cescato, "Mixing of the reflected waves to monitor and stabilize holographic exposures," *Optical Engineering*, vol. 35, pp. 2804-2809, Oct. 1996.
- [58] R. K. Heilmann, P. T. Konkola, C. G. Chen, G. S. Pati, and M. L. Schattenburg, "Digital heterodyne interference fringe control system," *Journal of Vacuum Science and Technology*, vol. 19, pp. 2342-2346, Nov.-Dec. 2001.
- [59] M. Schattenburg and P. N. Everett, "Method and system for interference lithography utilizing phase-locked scanning beams," U. S. Patent 6882477, April 19 2005.
- [60] F. Hrebabetzky and A. Albertazzi Jr., "Camera-based active phase stabilization for electronic holography," *Proceedings of the SPIE*, vol. 4420, *Laser Metrology for Precision Measurement and Inspection in Industry 1999*, pp. 155-161, 2001.
- [61] W. H. Press, S. A. Teukolsky, W.T. Vetterling, and B. P. Flannery, "Fast Fourier Transform," *Numerical Recipes in C, Second Edition*, Cambridge University Press, 1992, pp. 496-510.
- [62] R. Tacke, E. C. Rodenburg, M. Van der Veer, J. H. Van Fegchel, and R. Eijmberts, "Evaluation of I-line and DUV photoresists for high density optical disk mastering," *Proceedings of the SPIE*, vol. 4345, *Advances in Resist Technology and Processing XVIII*, pp. 637-646, 2001.
- [63] "Ultra-I 123 I-Line Photoresist" Rohm and Haas Electronic Materials Microelectronic Technologies Data Sheet, ME04N106.Rev.1, April 2005.
- [64] P. S. Priambodo, D. Shin, and R. Magnusson, "Fabrication and characterization of resonant optical filters," presented at the Optical Society of America Annual Meeting 2002, Orlando, FL, 2002.
- [65] M. L. Schattenburg, R. J. Aucion, and R. C. Fleming, "Optically matched trilevel resist process for nanostructure fabrication," *Journal of Vacuum Science and Technology B*, vol. 13, pp. 3007-3011, Nov.-Dec. 1995.

- [66] W. R. Runyan and K. E. Bean, *Semiconductor integrated circuit processing technology*, Reading, MA: Addison-Wesely, 1990, pp. 172-190.
- [67] Software Spectra Inc., “TFCalc Users Manual,” Software Spectra Inc., 2002.
- [68] R. Magnusson (private communication), 1998.
- [69] S. Li, G. Witjaksono, S. Macomber, and D. Botez,” Analysis of surface-emitting second-order distributed feedback lasers with central grating phaseshift,” *IEEE Journal of Selected Topics in Quantum Electronics*, vol. 9, pp.1153-1165, Sept.-Oct. 2003.
- [70] P. Rai-Choudhury, Ed., *SPIE Handbook of Microlithography, Micromachining and Microfabrication, Volume 1: Microlithography*. SPIE Press Monograph Vol. PM39, 1997, pp. 139-250.
- [71] Cornell NanoScale Science & Technology Facility (CNF), Cornell University, “CNF Resist Process Library,” June 2004, http://www.cnf.cornell.edu/cnf_process_ebl_resists.html.
- [72] Dow Corning, Product Information: Flowable Oxides, AMPM170/105, 2005.
- [73] H. Namatsu, T. Yamaguchi, M. Nagase, K. Yamazaki, and K. Kurihara, “Nanopatterning of a hydrogen silsesquioxane resist with reduced linewidth fluctuations,” *Microelectronic Engineering*, vol. 41-42, pp. 331-334, March 1998.
- [74] M. Kroon, F. C. van Delft, and W. S. Ketelaars, “Manufacturing sub-50-nm gratings using e-beam lithography and electroplating,” *Proceedings of the SPIE*, vol. 4688, *Emerging Lithographic Technologies VI*, Santa Clara, CA, USA 5-7 March 2002, pp. 922-931.
- [75] M. J. Word, I. Adesida, and P. R. Berger, “Nanometer-period gratings in hydrogen silsesquioxane fabricated by electron beam lithography,” *Journal of Vacuum Science & Technology B (Microelectronics and Nanometer Structures)*, vol. 21, pp. L12-L15, Nov. 2003.
- [76] L. Mollard, G. Cunge, S. Tedesco, B. Dal'zotto, and J. Foucher, “HSQ hybrid lithography for 20 nm CMOS devices development,” *Microelectronic Engineering*, vol. 61-62, pp. 755-761, July 2002.
- [77] C. M. Falco and F. C. van Delft, “Delay-time and aging effects on contrast and sensitivity of hydrogen silsesquioxane,” *Journal of Vacuum Science & Technology B*, vol. 20, pp. 2932-2936, Nov. 2002.

- [78] D. Gil, R. Menon, and H. I. Smith, "Fabrication of high-numerical-aperture phase zone plates with a single lithography exposure and no etching," *Journal of Vacuum Science & Technology B*, vol. 21, pp. 2956-2960, Nov. 2003.
- [79] D. Lauvernier, J. P. Vilcot, M. Francois, and D. Decoster, "Optimization of HSQ resist e-beam processing technique on GaAs material," *Microelectronic Engineering*, vol. 75, pp. 177-182, Aug. 2004.
- [80] D. Lauvernier, S. Garidel, C. Legrand, and J. P. Vilcot, "Realization of sub-micron patterns on GaAs using a HSQ etching mask," *Microelectronic Engineering*, vol. 77, pp. 210-216, April 2005.
- [81] O. D. Negrete and A. Bleier, "Fabrication of variable-thickness structures with e-beam sensitive HSQ resist," Cornell University, "2003-2004 CNF Research Accomplishments," 2004.
- [82] L. Frye and W. T. Collins, "The Oligomeric Silsesquioxanes, $(\text{HsiO}_{3/2})_n$," *Journal of the American Chemical Society*, vol. 92, pp. 5586-5588, Sept. 1970.
- [83] R. Williams, *Modern GaAs Processing Methods*, Boston, MA: Artech House, 1990, pp. 101-108.
- [84] D. F. Kyser and N. S. Viswanathan, "Monte Carlo simulation of spatially distributed beams in electron-beam lithography," *Journal of Vacuum Science and Technology*, vol. 12, pp. 1305-1308, Nov.-Dec. 1976.
- [85] G. Owen and P. Rissman, "Proximity effect correction for electron beam lithography by equalization of background dose," *Journal of Applied Physics*, vol. 54, pp. 3573-3581, June 1983.
- [86] PDF/ Solutions – AISS Division, "SCELETON," June 2005. [Online]. Available: <http://www.aiss.de/skeleton/skeleton-index.html>
- [87] PDF/ Solutions – AISS Division, "PROXECCO," June 2005. [Online]. Available: <http://www.aiss.de/PROXECCO/PROXECCO.html>
- [88] F. N. Timofeev, S. A. Gurevich, V. B. Smirnitskii, L. B. Gladysheva, B. S. Yavich, and A. Usikov, "Application of low-defect reactive ion etching in $\text{Cl}_2:\text{BCl}_3$ plasma in combination with overgrowth for formation of GaAs/AlGaAs submicrometre structures," *Semiconductor Science Technology*, vol. 11, pp. 797-800, May 1996.

- [89] M. Pelton, "An efficient source of single photons: a single quantum dot in a micropost microcavity," Ph.D. Dissertation, Department of Applied Physics, Stanford University, Stanford, CA, 2002.
- [90] B. A. Saleh and M. C. Teich, Fundamentals of Photonics, New York: John Wiley & Sons, Inc., 1991, pp.495-522.

BIOGRAPHICAL INFORMATION

Preston P. Young received the B.S. (magna cum laude) degree in electrical engineering from the University of Texas at Arlington in 1997. He completed his M.S. degree in electrical engineering in 1999 at UTA. He received his doctorate in Electrical Engineering in May 2006. He also has an AAS (highest honors) in electronic technology from Texas State Technical Institute. He received support from the National Science Foundation Research Experiences for Undergraduates that led to his pursuit of graduate degrees in electrical engineering.

He worked beginning in 1990 as an engineering technician for industry research and development groups. He has been employed as a researcher by the UTA Electro-optics Research Center since 1995. His research has been in the areas of lasers, diffractive, and waveguide structures with an emphasis on prototype guided-mode resonance devices and applications. Current areas of study involve the fabrication and integration of diffractive structures with dielectric, semiconductor, and active materials for applications at visible, infrared, and microwave frequencies. He holds a patent on vertical cavity surface-emitting lasers incorporating resonant waveguide-grating reflectors. He is a member of OSA and IEEE-LEOS.